



Efficient transducer modelling and characterization for handheld optoacoustic tomography

Kaushik Basak Chowdhury

Vollständiger Abdruck der von der Fakultät für Elektrotechnik und Informationstechnik der Technischen Universität München zur Erlangung des akademischen Grades eines

Doktors der Ingenieurwissenschaften (Dr.-Ing.)

genehmigten Dissertation.

Vorsitzende: Prof. Dr. Gabriele Schrag

Prüfer der Dissertation:

1. Prof. Dr. Vasilis Ntziachristos
2. Prof. Dr. Oliver Hayden

Die Dissertation wurde am 15.02.2021 bei der Technischen Universität München eingereicht und durch die Fakultät für Elektrotechnik und Informationstechnik am 03.11.2021 angenommen.

Abstract

Optoacoustic (photoacoustic) tomography (OAT) equipped with structural, functional, and molecular imaging capabilities has demonstrated immense potential in a wide range of pre-clinical applications. Such optoacoustic tomographic setups with detector arrays covering the full angular range are only suitable for small animal imaging. Handheld scanners with linear or arc shaped ultrasound transducers arrays have made considerable progress and have been promising candidates for clinical applications. Despite several demonstrations of disease diagnosis in humans, handheld optoacoustic scanners still face some challenges towards generation of high-quality images rendering faithful clinical information. The quality of images generated using OAT imaging systems directly depends on the characteristics of the system components. The effect of the components of handheld scanners on image quality has not been considered in detail so far. The work presented in this thesis is mainly dedicated towards the improvement of image quality in handheld optoacoustic tomography using efficient transducer modelling and novel characterization techniques.

The shape and bandwidth of the transducers are modelled as spatial and electrical impulse responses, SIR and EIR, respectively. It is demonstrated that the EIR can be derived by deconvolving the simulated SIR from only one measurement of TIR. The derived EIR, being spatially independent is combined with the simulated SIR to obtain the full field of view (FOV) characterization of the handheld scanner called the synthetic TIR (sTIR) model. The capability of the sTIR model to reconstruct images of significantly higher accuracy and resolution is demonstrated using recorded data from phantoms and healthy probands.

To achieve higher image quality, this work further investigates the variation of EIRs across transducer elements within the array instead of assuming identical EIR for all transducers like existing impulse response correction methods. A robust method to determine the individual EIR of the transducer elements is proposed which uses only few TIR measurements and solves the linear system for the temporal convolution. The forward model correcting for the individual EIRs called individual synthetic TIR (isTIR), demonstrates significant improvement in isotropic resolution.

The inclusion of the transducer properties into the forward model leads to increasing computational load and inversion time. Therefore, a hybrid regularization scheme based on bidiagonalization regularization is explored to tackle this problem. Apart from characterizing the resolution achieved by the handheld optoacoustic tomography system, a few other system specifications were characterized such as image slice thickness, noise, and illumination profile, which offer important insight towards the performance of the imaging system.

The proposed modelling and characterization techniques are believed to open new possibilities to optimize the design of handheld optoacoustic scanners with any coupling medium of known acoustic properties and produce high quality images, eventually facilitating clinical translation.

Zusammenfassung

Die optoakustische (photoakustische) Tomographie (OAT), die mit strukturellen, funktionellen und molekularen Bildgebungsmöglichkeiten ausgestattet ist, hat ein immenses Potenzial in einer Vielzahl von präklinischen Anwendungen gezeigt. Solche optoakustischen Tomographiesysteme mit einem Detektorring, der den gesamten Winkelbereich abdeckt, eignen sich nur für die präklinische Bildgebung von Kleintieren. Handgeführte Scanner mit linearen oder bogenförmigen Ultraschallwandler-Arrays haben beträchtliche Fortschritte erzielt und sind vielversprechende Kandidaten für klinische Anwendungen. Trotz mehrerer Demonstrationen von Krankheitsdiagnosen beim Menschen stehen handgeführte optoakustische Scanner immer noch vor einigen Herausforderungen bei der Erzeugung qualitativ hochwertiger Bilder, die getreue klinische Informationen wiedergeben. Die Qualität der Bilder, die mit einem OAT-Bildgebungssystem erzeugt werden, hängt direkt von den Eigenschaften der Systemkomponenten ab. Der Einfluss der Komponenten von handgeführten Scannern auf die Bildqualität ist bisher nicht im Detail untersucht worden. Die in dieser Arbeit vorgestellten Methoden widmen sich hauptsächlich der Verbesserung der Bildqualität in der handgeführten optoakustischen Tomographie unter Verwendung effizienter Schallkopfmodellierung und neuartiger Charakterisierungstechniken.

Form und Bandbreite der Schallköpfe werden als räumliche und elektrische Impulsantworten, SIR bzw. EIR, modelliert. Es wird gezeigt, dass die EIR durch Entfaltung (Dekonvolution) der simulierten SIR aus nur einer Messung der TIR abgeleitet werden kann. Die abgeleitete EIR, die räumlich unabhängig ist, wird mit der simulierten SIR kombiniert, um die Charakterisierung des gesamten Sichtfeldes (FOV) des Handscanners, das synthetische TIR-Modell (sTIR) genannt wird, zu erhalten. Die Fähigkeit des sTIR-Modells, Bilder mit deutlich höherer Genauigkeit und Auflösung zu rekonstruieren, wird anhand von aufgezeichneten Daten von Phantomen und gesunden Probanden demonstriert.

Um eine höhere Bildqualität zu erreichen, wird in dieser Arbeit die Variation der EIRs zwischen den Wandlerelementen innerhalb des Arrays weiter untersucht, anstatt wie bei bestehenden Impulsantwortkorrekturverfahren von einem identischen EIR für alle Wandler auszugehen. Es wird eine robuste Methode zur Bestimmung der individuellen EIR der Wandlerelemente vorgeschlagen, die nur wenige TIR-Messungen verwendet und das lineare System für die zeitliche Faltung löst. Das für die einzelnen EIRs korrigierte Vorwärtsmodell, das als individueller synthetischer TIR (isTIR) bezeichnet wird, zeigt eine deutliche Verbesserung der isotropen Auflösung.

Die Einbeziehung der Detektoreigenschaften in das Vorwärtsmodell führt zu einer Erhöhung der Rechenlast und der Inversionszeit. Daher wird ein hybrides Regularisierungsschema auf der Basis der Bidiagonalisierungs-Regularisierung untersucht, um dieses Problem zu lösen. Zusätzlich zur Charakterisierung der durch das handgeführte optoakustische Tomographiesystem erzielten Auflösung wurden weitere Systemspezifikationen wie Bildschichtdicke, Rauschen und Beleuchtungsprofil charakterisiert, die wichtige Einblicke in die Leistung des Bildgebungssystems bieten.

Es ist davon auszugehen, dass die vorgeschlagenen Modellierungs- und Charakterisierungs-techniken neue Möglichkeiten eröffnen, das Design von optoakustischen Handheld-Scannern mit beliebigen Kopplungsmedien bekannter akustischer Eigenschaften zu optimieren und qualitativ hochwertige Bilder zu erzeugen, die schließlich die klinische Übersetzung erleichtern.

Acknowledgements

The support, guidance and mentoring provided by several individuals were crucial during the three years of research work presented in this thesis.

First, I would like to sincerely thank my supervisor Prof. Vasilis Ntziachristos for providing me the wonderful opportunity to work in the exciting field of optoacoustics at his highly interdisciplinary lab of great international repute. I would also like to thank him for assigning me with the problem of impulse response correction of handheld clinical scanners, which was not only challenging but also a great learning experience in both aspects of modelling and experiments. Then, I would like to express my gratitude for Prof. Oliver Hayden, who agreed to act as my second supervisor. Without his kind and generous support during yearly evaluation, the Graduate school requirements for doctoral studies would not be satisfied. I was also fortunate to attend some of his lecture talks and his charisma is truly inspirational.

I am immensely grateful to Dr. Dominik Jüstel for his support and patience while mentoring me during the final phase of my research. Discussing theoretical concepts with him for long hours on the whiteboard is something I still fondly remember. His timely support was immensely valuable towards the completion of this dissertation. I am deeply grateful to Dr. Jaya Prakash for mentoring me during the first half of my research. I am ever grateful to him for introducing me to the area of computation and reconstruction algorithms and teaching me how to solve problems independently instead of being spoon-fed, a valuable lesson I will cherish for lifetime. Even after his departure from the group, he continued to provide valuable support and guidance. I also thank Dr. Angelos Karlas for having me as a member of the clinical optoacoustics group. Without this collaboration I would not be able to perform experiments in the clinic and visualize the real-life challenges of translating optoacoustic imaging to the clinics.

I am sincerely thankful to Dr. Xosé Luís Deán-Ben, Dr. Korbinian Paul-Yuan and Dr. Alexander Urich (iThera Medical GmbH) for introducing me to phantom development and imaging system characterization. I am very much obliged to Dr. Gael Diot and Hong Yang for sharing with me the parameters of the MSOT Acuity which was undocumented at the beginning of my research. I would like to specially thank Dr. Stefan Morscher and Dr. Marcin Kacprowicz from iThera Medical GmbH for sharing the design and specification of the MSOT Acuity handheld probe, without which the work presented in this thesis would not be accomplished. I am also very thankful to Dr. Christian Zakian for his unconditional support and playing multiple roles of mentor, guide and friend during ups and downs of research. His amazing leadership style continues to inspire me.

I would like to express my gratitude to my colleague Christoph Dehner and Maximilian Bader for supporting with the computational resources for high resolution reconstruction using isTIR model. I also sincerely thank Christoph for the fruitful collaboration in the deep learning-based noise removal project. I would also like to acknowledge Maria Anastasopoulou for providing the necessary optical imaging infrastructure for characterizing the laser illumination profile of the MSOT Acuity. Her knowledge and experience in building phantoms with calibrated optical properties were immensely helpful for a portion of work presented in this thesis.

I am incredibly grateful to my colleagues, officemates, and friends Dr. Lucas Riobo, Antonia Longo, Francesca Gasparin, Andrei Bereznoi, Dr. Philipp Köhler, Benedikt Schätz, Tao Yuan and Dr. Nasire Uluc for creating a friendly atmosphere and offering cheerful company during coffee breaks. I thank Lucas for helping me with preparation of few figures in Latex during the crucial time of manuscript preparation. I also thank Francesca for the supply of good coffee for a long period of time without which working for long hours would not be possible. I thank Antonia Longo for her support during the stressful times.

I am greatly indebted to Dr. A. Chapin Rodríguez not only for proofreading my first journal article but also helping to build the storyline. Working with him and attending his workshops really improved my skills in scientific storytelling. I am also grateful to scientific writer Dr. Sergey Sulima for helping in proofreading my second journal article and providing necessary help to fast track other publication related issues. Additionally, I thank scientific writer Dr. Robert Wilson for his valuable support towards the end of my tenure at IBMI.

I am profoundly thankful to several members of the admin team – Susanne Stern, Lidia Seidel and Dr. Andreas Hillmair for their valuable co-operation and support throughout my doctoral project. I am also grateful to Dr. Roland Boha for his valuable support in maintaining, managing IT-equipment. I sincerely thank Prof. Dr. Karl-Hans Englmeier, for helping with crucial paperwork on several occasions. I am deeply grateful to the laboratory technicians Dr. Uwe Klemm and Sarah Glasl for their patience, support, and value assistance towards using and procurement of different laboratory equipment and consumables. Without this valuable support many experiments presented in this thesis would not be feasible.

I am very thankful to Dr. Vipul Gujrati not only for assisting me the very first day in Germany but also for providing valuable assistance to navigate smoothly through the bureaucratic issues at the beginning of life in Munich. I am very thankful to Subhamoy Mandal for providing me with valuable feedback on choosing graduate school which was extremely helpful later. I admire his wealth of knowledge and his willingness to support with patience. I also thank Kanuj Mishra for inviting me for tea after Monday meetings and having funny conversations.

I would like to express my deepest gratitude towards the Graduate Center of Bioengineering (GCB) at Munich School of Bioengineering for accepting me as into their doctoral program and especially I would like to thank ex-GCB coordinator Dr. Anja Drescher whose support was invaluable during the doctoral program. Also, the summer schools organized and led by her were filled with networking activities crucial for doctoral training. The lecture talks, workshops and dinners involving scientists and researchers from various disciplines of academia and industry enriched me both professionally and personally. The summer schools offered me the opportunity to escape from the intense life for a few days to rejuvenate.

Finally, I would like to thank my family for their constant support, love, and motivation. I thank my mother for her great patience with the longer periods of my absence. I would like to specially my friend from IIT Madras, Rudra, who encouraged me to move abroad for pursuing the PhD studies. Also, I am deeply grateful to my dearest friend Marzena, whose encouragement, support and patience were extremely beneficial to go through the ups and downs of life during doctoral program.

Contents

Abstract	3
Zusammenfassung	5
Acknowledgements	7
Contents	10
List of abbreviations	13
List of figures	15
1. Introduction	17
1.1. Traditional clinical imaging modalities	17
1.2. Motivation behind clinical optoacoustic imaging	17
1.3. Challenges for handheld optoacoustic imaging	22
1.4. Outline of the thesis	24
2. Brief theory of optoacoustic image reconstruction	27
2.1. Forward model	27
2.2. Inverse Problem	29
2.3. Advantages of model-based reconstruction	31
3. Transducer properties and characterization of optoacoustic tomography system	32
3.1. Motivation	32
3.2. Transducer properties	33
3.2.1. Spatial impulse response (SIR)	34
3.2.2. Electrical impulse response (EIR)	35
3.3. Characterization of transducers for medical ultrasound	37
3.4. Characterization of transducers for optoacoustic tomography	38
3.5. Specifications of optoacoustic tomographic imaging system	40
3.5.1. Resolution	41
3.5.2. Image slice thickness	42
3.5.3. Illumination profile	47
3.5.4. Noise	49
3.6. Modeling optoacoustic wave detection	52
3.7. TIR model for constant acoustic speed	53
3.8. Discussion	56
4. A synthetic total impulse response for handheld tomography	59
4.1. Motivation behind TIR characterization of handheld systems	59
4.2. Acoustic refraction	61

4.3.	Dependence of SIR on refraction	63
4.4.	TIR model based on refraction at membrane interface.....	64
4.5.	Synthetic TIR (sTIR).....	65
4.5.1.	Measurement of TIR at center of FOV	65
4.5.2.	Simulation of refraction-based SIR	66
4.5.3.	Derivation of approximate EIR.....	68
4.5.4.	Validation of the simulated SIR	70
4.5.5.	Synthesis of sTIR	70
4.5.6.	sTIR forward models	70
4.6.	Image correction using sTIR	72
4.6.1.	Description of the optoacoustic imaging platform.....	72
4.6.2.	Image correction framework.....	73
4.6.3.	Numerical phantoms	74
4.6.4.	Experimental measurements	75
4.7.	Results.....	75
4.7.1.	Characterization of system resolution	75
4.7.2.	Reconstruction using numerical phantoms.....	78
4.7.3.	Evaluation of effect of noise on numerical simulation	82
4.7.4.	Experimental validation with physical phantom	84
4.7.5.	Clinical measurements	86
4.7.6.	Robustness of sTIR against variation of acoustic speed in tissue.....	89
4.8.	Discussion	91
5.	Characterization of individual transducer element response.....	94
5.1.	Motivation	94
5.2.	Individual synthetic TIR (isTIR)	95
5.2.1.	Measurements in multiple locations	97
5.2.2.	Modelling of SIR and pixel response at measured locations	97
5.2.3.	Derivation of individual aEIR	97
5.2.4.	isTIR forward model.....	98
5.3.	Image correction using isTIR	100
5.3.1.	Image correction framework.....	100
5.3.2.	Experimental measurements	100
5.4.	Results.....	101
5.4.1.	Characterization of system resolution	101
5.4.2.	Reconstruction of grid scan	104
5.4.3.	Clinical measurements	106

5.5.	Discussion	108
6.	Efficient inversion for optoacoustic image reconstruction with sTIR	110
6.1.	Motivation behind the hybrid regularization	110
6.2.	Hybrid regularization based on bidiagonalization	112
6.3.	LSQR based choice of regularization parameter	114
6.4.	Discussion	119
7.	Conclusion	121
7.1.	Conclusive summary	121
7.2.	Future outlook	123
	Appendix A	126
	Bibliography	127
	List of Publications	138

List of abbreviations

CAD – Computer aided design

DAQ – Data acquisition

EIR – Electrical impulse response

FOV – Field of View

FMD – Flow mediated dilation

GPU – Graphics Processing Unit

LTI – Linear time invariant

MSOT – Multispectral optoacoustic tomography

NIR – Near infra-red

OA – Optoacoustic

PA – Photoacoustic

PET – Positron Emission Tomography (PET)

ROI – Region of interest

RSME – Root mean square error

SIR – Spatial impulse response

SPECT – Single Photon Emission Computed Tomography

SLN – Sentinel Lymph Node

TIR – Total impulse response

Hb – Hemoglobin

HbO₂ – Oxygenated Hemoglobin

MI – Mutual Information

MRI – Magnetic Resonance Imaging

OAT – Optoacoustic Tomography

OCT – Optical Coherence Tomography

USI – Ultrasound Imaging

List of figures

Figure 1.1: Concept of optoacoustic tomographic imaging.	18
Figure 1.2: Concept of Multispectral Optoacoustic Tomography (MSOT).	19
Figure 1.3: An example of clinical handheld optoacoustic imaging.	22
Figure 2.1: Geometry of inverse source detection.	28
Figure 2.2: Discretization of optoacoustic wave detection.	29
Figure 2.3: Concept of forward and inverse problem.	30
Figure 3.1: Concept of Spatial Impulse Response (SIR).	34
Figure 3.2: Concept of Electrical Impulse Response (EIR).	36
Figure 3.3: Schematic of typical characterization of optoacoustic imaging system.	40
Figure 3.4: Illustration of slice thickness using the sensitivity map in the elevation plane.	43
Figure 3.5: Construction of phantom to characterize the image slice thickness.	44
Figure 3.6: Characterization of the image slice thickness using cross-sectional image of incline suture phantom.	46
Figure 3.7: Characterization of the illumination profile.	48
Figure 3.8: Characterization of noise.	51
Figure 3.9: Physical characteristics of transducers.	53
Figure 3.10: Schematic of limited view transducer using constant acoustic speed model.	55
Figure 4.1: Modelling of the handheld scanner.	61
Figure 4.2: Schematic of limited view transducer using refraction model.	62
Figure 4.3: Schematic of signal decomposition.	64
Figure 4.4: Photograph of signal measurement.	65
Figure 4.5: Simulation of refraction-based SIR.	67
Figure 4.6: Experimentally derived aEIR and validation of simulated SIR.	69
Figure 4.7: The handheld optoacoustic imaging system.	73
Figure 4.8: Improvement in system resolution using sTIR models.	77
Figure 4.9: Reconstruction of numerical dot grid phantom to demonstrate the negative effects on image quality due to neglecting transducer properties.	79
Figure 4.10: Reconstruction of numerical USAF target phantom to demonstrate the negative effects on image quality due to neglecting transducer properties.	81

Figure 4.11: Evaluation of effect of increasing noise on the structural quality in reconstruction of numerical phantoms.	83
Figure 4.12: Improvement in reconstruction of physical phantom using the sTIR models.	85
Figure 4.13: Schematic of locations of clinical scans.	86
Figure 4.14: Improvement in reconstruction of clinical images using sTIR model.	88
Figure 4.15: Evaluation of robustness of M_0 and M_R^{sTIR} models against slight variation of acoustic speed in tissue.	90
Figure 5.1: Characterization of individual transducer response.	96
Figure 5.2: Variation of aEIR across transducer elements.	99
Figure 5.3: Improvement in isotropy and resolution.	103
Figure 5.4: Improvement in isotropic resolution throughout the FOV of the grid scan.	105
Figure 5.5: Improvement in clinical images.	107
Figure 6.1: Zeros in modelled signals.	111
Figure 6.2: Hybrid regularization.	116
Figure 6.3: Illustration of choice of the regularization parameter using hybrid regularization method.	118

1. Introduction

1.1. Traditional clinical imaging modalities

Imaging plays a crucial role in screening, diagnosis, and treatment monitoring of diseases. Clinical imaging modalities have evolved a long way since the first usage of X-ray photographic plates to examine bone fracture to current day ultra-high-field Magnetic Resonance Imaging (MRI) used to map the human body at unprecedented detail [1], [2]. This exponential growth in diagnostic radiology was fueled by the innovations in instrumentation and computers. The established clinical imaging modalities for structural and functional imaging include X-ray Computed tomography (CT), Ultrasound imaging (USI), Magnetic Resonance Imaging (MRI), Positron Emission Tomography (PET) and Single Photon Emission Computed Tomography (SPECT). These clinical imaging modalities are routinely used for detection of cancer [3], one of the deadly diseases[4] which requires early detection. Nuclear medicine techniques such PET/SPECT use radioactive tracers in small quantities to detect tumors deep inside the human body with high specificity but with low resolution. Nevertheless, these techniques expose the patient to harmful ionizing radiation of radioactive dyes and have low signal to noise ratio due to short-lived nature of radio-isotopes. Optical imaging techniques on the other hand are non-ionizing in nature, do not require radioactive tracers and take advantage of distinct absorption spectra of molecules in cancerous tissue. Microscopic optical imaging techniques offer sensitive detection and higher resolution ($\sim 0.1\mu\text{m}$) compared to the established imaging modalities like CT, MRI, PET and SPECT where the attainable resolution is in the range of (1mm – 10mm) [5]. However, the penetration depth of microscopic optical imaging is low ($\sim 1\text{mm}$) due to diffusion limit [6] and traditional optical tomography technique called Diffuse Optical Tomography (DOT) can image several centimeters deep inside tissue but suffers from poor resolution due to scattering of light [6], [7]. Hence, there is a need for a imaging modality which can image molecular contrast [5] at resolutions of few hundreds of microns at considerable penetration depth of several centimeters; which has been filled by Optoacoustic (Photoacoustic) imaging.

1.2. Motivation behind clinical optoacoustic imaging

In the last two decades optoacoustic imaging has shown immense potential in structural and functional imaging capabilities for small animals and clinical applications [7]–[10]. This growth of optoacoustic imaging across a wide range of spatial scales – cells to organs [6], can be attributed to its unique resolution to depth ratio (around 1/200) [6]. Optoacoustic imaging

capitalizes of the photoacoustic phenomenon which was first reported by Alexander Graham Bell and Sumner Tainter with the invention of photophone back in 1880 [11]. Only after a century in the 1990s optoacoustic sensing in one-dimension was introduced [12], [13]. Soon with the development of sophisticated lasers optoacoustic tomography was also demonstrated [14], [15].

The concept of optoacoustic tomographic imaging is illustrated in Figure 1.1. Laser pulses of very short duration (few nanoseconds), are used to optically excite tissue sample, which generates broadband ultrasound waves due to thermoelastic expansion [16]. The outwardly propagating ultrasound waves are intercepted using transducers placed at different angular positions. The recorded 1D signals at different projection angles can be arranged as a sinogram shown in Figure 1.1. The recorded sinogram is fed into tomographic reconstruction algorithm to generate optoacoustic image rendering the initial pressure distribution of the sample being examined [17]. The initial pressure distribution is proportional to the optical absorption map of the sample. Hence, the optoacoustic image generated using the acoustic inversion may be termed as qualitative optoacoustic imaging.

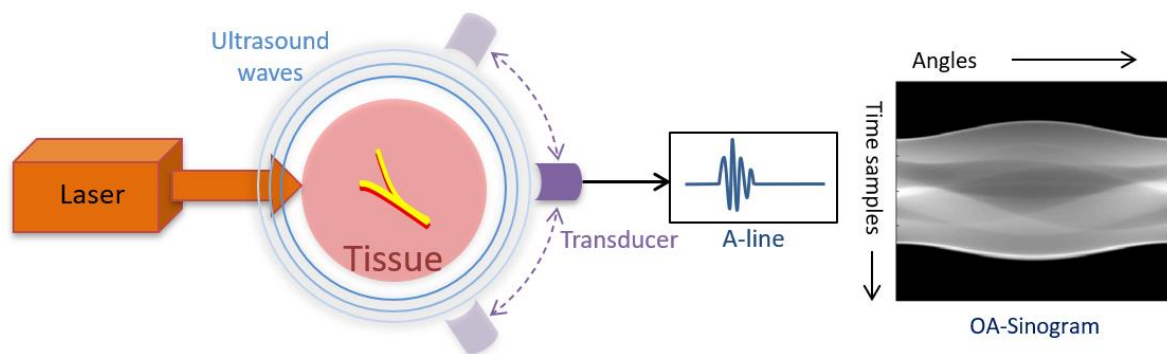


Figure 1.1: Concept of optoacoustic tomographic imaging. Pulsed laser excitation of tissue sample generates ultrasound waves which are intercepted by ultrasound transducers placed around the sample eventually generating a sinogram. The sinogram can be used to reconstruct the initial pressure distribution of the tissue sample.

The optoacoustic image obtained using a single laser excitation wavelength corresponds to the optical absorption map at that wavelength, which is the linear combination of molecular extinction coefficients of different molecules at that wavelength and the coefficient representing the concentration of the molecule. This feature can be utilized to implement hyperspectral imaging [18] in optoacoustic tomography. The absorption spectra can be sampled using multiple laser excitation wavelengths and thereby distinguishing tissue composition based on

the differences in optical absorption spectra. This led to the development of multispectral optoacoustic tomography (MSOT) [8]. The concept of MSOT is illustrated in the Figure 1.2. Consider a tissue sample consisting of arteries and veins consisting of oxygenated (HbO₂) and deoxygenated hemoglobin (Hb) respectively. This tissue sample is excited at multiple wavelengths in the near IR (NIR) range, OA sinograms at different wavelengths can be recorded as shown in Figure 1.2a. Thereafter the initial pressure images at given excitation wavelength can be obtained using acoustic inversion of the recorded OA sinogram. Finally, concentrations of different chromophores in the arteries and veins can be resolved using spectral unmixing of the reconstructed images at different wavelengths. Spectral unmixing [19], [20] is the linear inversion scheme which uses prior information of absorption spectra of the chromophores as shown in the Figure 1.2b. Since unmixed multispectral images approximately represent the optical absorption maps of the individual chromophores they are referred to as quantitative optoacoustic images [21]. Thus, MSOT facilitates label-free imaging of endogenous chromophores such as Hb, HbO₂, lipids, collagen in biological tissues *in-vivo* leading to wide range of preclinical and clinical applications [8].

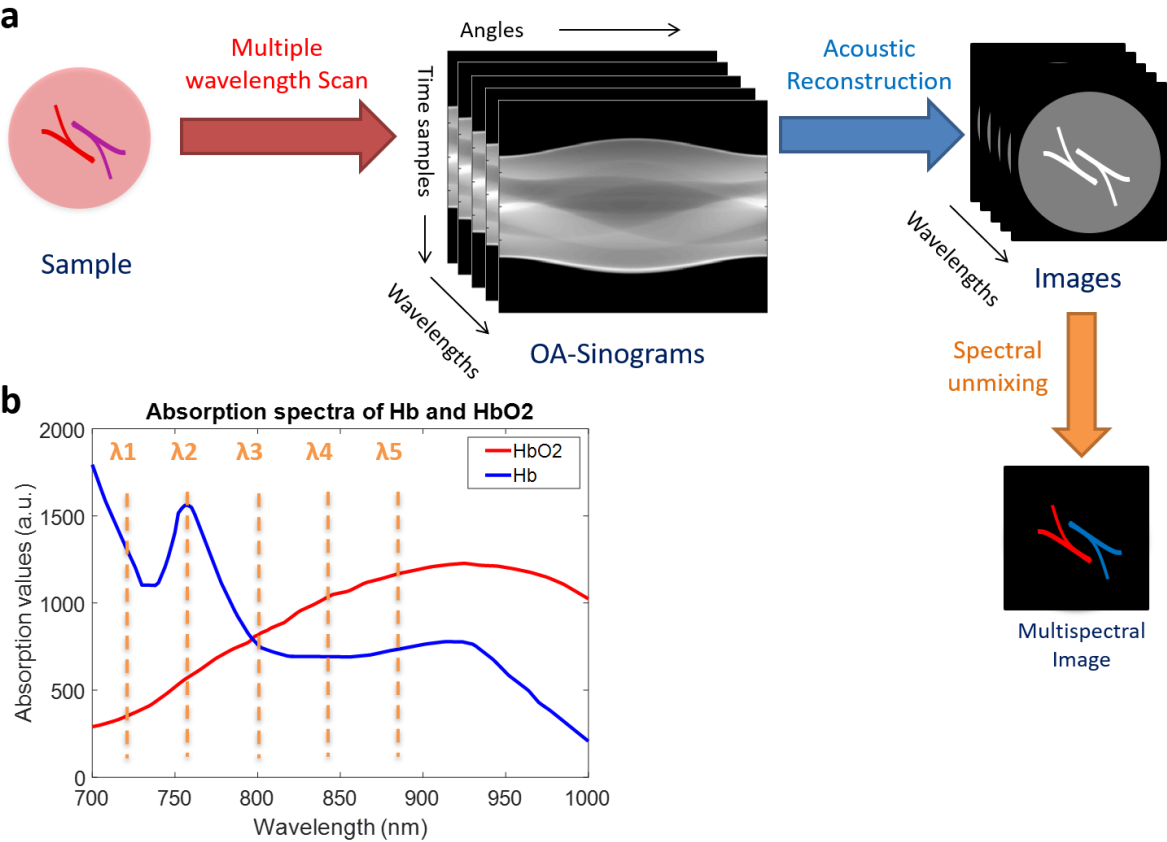


Figure 1.2: Concept of Multispectral Optoacoustic Tomography (MSOT). (a) Illustration of multispectral optoacoustic imaging from multiwavelength scan to spectral unmixing. (b) Exemplary

sampling at five wavelengths in the absorption spectra of two commonly observed chromophores – Hb and HbO₂. (Source of data in panel b: <https://www.omlc.org/>)

Optoacoustic tomography (OAT) offers several advantages compared to optical, fluorescence and ultrasound imaging. The acoustic scattering in biological tissue is roughly three orders of magnitude lower than optical scattering and hence optoacoustic imaging offers higher image resolution in deep tissue compared to optical and fluorescence imaging [6], [7], [9]. Non-absorbing components in tissue samples does not emit ultrasound signals hence there is no background signal. Also, the excitation light does not leak into the detection system which is often a challenge in fluorescence imaging systems [6]. OAT is a speckle-free [22] imaging modality unlike USI and OCT. USI offers mechanical contrast while OAT offers optical contrast allowing characterization of tissue based on differences in optical absorption, which can be used to detect disease or anomaly in physiological process. This particular property of OAT led to the development of widespread applications in disease detection as elaborated next.

The ability of OAT to resolve chromophores based on the optical absorption property positions this hybrid imaging modality as a molecular imaging technique with wide range of applications in clinical imaging [10], [23]–[25] especially for cancer diagnosis [26], [27]. Angiogenesis, which is a physiological process of formation of new blood vessels from existing ones, is one of the hallmarks of cancer [28]. Angiogenesis often leads to enhancement in metabolic rate depleting HbO₂ rapidly inducing hypoxia. It has been demonstrated that the tumor cores exhibiting hypoxia can be detected by imaging the relative concentrations of Hb and HbO₂ using spectroscopic OAT in a label-free manner [29], [30]. As an alternative to X-ray mammography which uses harmful ionizing irradiation, ability of OAT to detect breast cancer has been widely explored [24], [31]–[34]. Traditional X-ray mammography and ultrasound examination results can conceal cancerous tissue inside breasts with higher density which is often a case in females with relatively younger age group. However, it was reported that the OAT contrast was independent of breast density which is a significant advantage over conventional techniques with mechanical contrast [35]. The use of OA imaging has been explored at a microscopic/mesosopic scale for detection of skin cancer [36], [37]. *Ex-vivo* detection of thyroid cancer [38], prostate cancer [39] and ovarian cancer [40] has also been attempted. *In-vivo* detection of cancer using various contrast agents – fluorescent dyes, nanoparticles, nanotubes, and nano-droplets, etc. are compiled in several reviews [41]–[44]. Apart from detection of cancer, OAT has also been used to target other areas in clinical imaging. Intravascular OA imaging has been used to image atherosclerosis in coronary arteries [45], [46].

In the domain of orthopedics, OAT was applied to diagnose arthritis from images of finger joints [47], [48]. Overall, OAT has demonstrated its potential as a valuable clinical diagnostics tool. Nevertheless, for clinical translation and global adoption there are several challenges which needs to be addressed such as availability, affordability, portability, standardization and regulatory [27].

Handheld scanning configurations [49] of OAT has progressed significantly over the past decade due to several inherent advantages. First, easy integration of optical fiber coupled laser with established clinical ultrasound transducers led to fast prototyping of handheld optoacoustic imaging systems for research applications [36], [49]–[52]. Second, integration with ultrasound imaging system enables dual modality OA/US imaging [53]–[55]. Third, handheld scanning configuration leads to enhanced portability of the imaging system making it useful for wide range of clinical examinations [56]–[58]. Apart from integrating laser with conventional ultrasound systems, several handheld OAT systems were built with suitable choice of array based ultrasound transducer arrays [15], [58]–[60]. Inspired by the capabilities of the lab-made handheld OAT systems, few commercial handheld scanners have made some progress in design and implementations [31], [36], [61], [62]. Handheld configurations of OAT has been used in clinical setting for breast imaging [31], [62], [63], thyroid imaging [64], [65], detection of atherosclerosis in carotid artery [66], flow mediated dilation (FMD) tests [67], muscle hemodynamics [60], [68], detection of sentinel lymph node (SNL) [53], [69], detection of melanoma beneath skin [70], [71] and imaging of intestinal walls [72]. Even though handheld configurations of OAT have shown much higher potential than benchtop OAT systems towards clinical studies, there are several challenges faced by handheld scanners which needs to be addressed for gaining momentum towards translation to clinics. These challenges will be discussed in the next section.

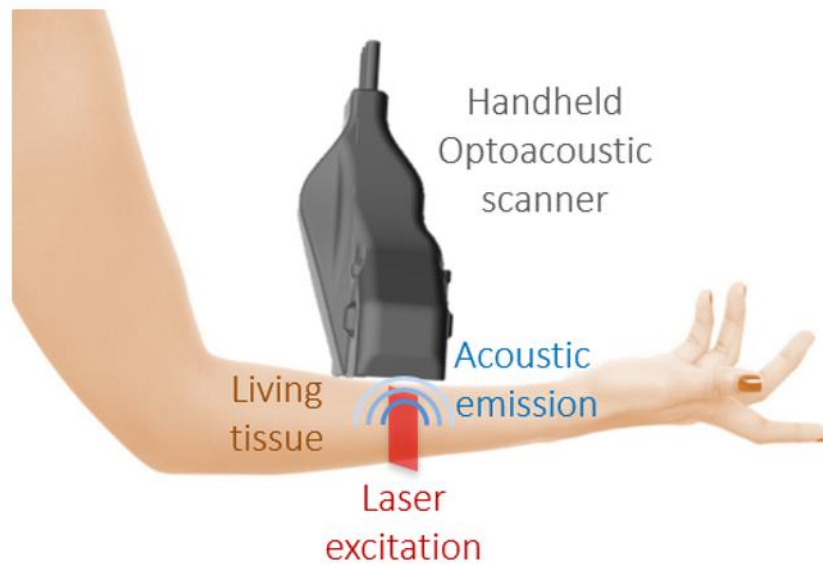


Figure 1.3: An example of clinical handheld optoacoustic imaging. Laser tunable in a range of wavelengths in the NIR region excites the human tissue and the generated optoacoustic waves are recorded by a handheld optoacoustic scanner, later to be reconstructed to form a cross sectional image. Regular ultrasound gel is used as a coupling medium.

1.3. Challenges for handheld optoacoustic imaging

The diagnostic value of the handheld optoacoustic tomography systems strongly depends on the quality of the images reconstructed. The quality of the reconstructed optoacoustic images in turn depends on how precisely the imaging physics and the instrument responses are mathematically modelled [73]–[81]. An example of clinical scan using typical handheld OAT scanner is shown in the Figure 1.3. The handheld scanner is typically gently pressed against the skin surface with regular ultrasound gel in between the probe surface (or transducer array) and skin for acoustic coupling. The laser excitation is directed outward from the probe surface and the acoustic waves generated from the tissue sample is collected into the probe surface. For ergonomic reasons, the transducer probe must be compact and lightweight for handheld scanning. The compactness introduces design constraints in terms of having shorter object to detector distance leading to technical challenges. Also, the handheld scanner must be held firmly during the data recording process. Otherwise, even small motion can lead to misalignment of data acquisition across different excitation wavelengths leading to erroneous unmixed chromophore maps. Additionally, due to compact geometry of handheld probes the entire volume of sample cannot be uniformly excited with laser irradiation and therefore the fluence decays with imaging depth. All these different aspects of the handheld scanner can

affect the quality of reconstructed images in different magnitudes. These challenges can be summarized as –

- i) Illumination inhomogeneity owing to fluence decay deep inside sample volume [82], [83]
- ii) Attenuation of ultrasound waves during propagation through sample [84], [85]
- iii) Limited angular coverage of detectors making the reconstruction problem ill-posed [80], [86], [87]
- iv) Finite dimension of detector aperture to intercept larger amount of incoming wavefront eventually leading to higher sensitivity [88]–[90]
- v) Response of the detectors due to limited bandwidth capabilities arising from material properties and signal transduction electronics [88], [90]
- vi) Inhomogeneity in responses among transducer elements within an array [91]
- vii) The acoustic property mismatch between the sample and the coupling medium [92]

The influence of each of the component of the imaging system can be analyzed separately as noted from the literature cited above. Since, the detector plays the most vital role in the formation of images, detector characteristics and properties has been an important topic of research. The influence of the physical and acoustoelectric properties of the detector can be captured by the total impulse response (TIR) of the imaging system [93], [94]. TIR characterization is a tedious process where a point source must be scanned in a dense grid throughout the field of view of the scanner. Furthermore, mismatch in the acoustic properties of sample and coupling medium causing acoustic refraction, which will further complicate the TIR characterization problem. The effects of the coupling medium on the TIR of the detector has never been systematically explored. With increased use handheld scanners for clinical applications [10], [27], [49], [95], there is an urgent need to develop a robust and efficient method to characterize the properties of the scanner and develop novel reconstruction schemes to generate images of higher quality.

The goal of the thesis was to address the problem of modelling and characterizing the entire transducer probe to improve image quality in handheld optoacoustic tomographic imaging, which poses unique challenges as described in the last paragraph. The optoacoustic wave detection mechanism in the entire handheld scanning probe was mathematically modelled. Refraction arising due the acoustic speed mismatch between tissue and coupling medium was included in the forward model. The SIR of the transducer array was numerically

simulated including refraction and the EIR of the transducer was experimentally derived using a recorded data from a single point source. Combining the experimentally derived EIR and the numerically simulated SIR, the composite synthetic TIR was generated which is called sTIR. The performance of the sTIR model is then demonstrated with physical phantoms and clinical scans. Thereafter a robust method to determine the individual EIR of the transducer elements is conceived using least square solution of a set of linear equations formulated using sparse measurements of point sources. The individual EIRs combined with refraction-based SIR resulted in the so called individual synthetic TIR or isTIR. Microsphere phantoms and clinical scans were again used to evaluate the performance of the isTIR model. Superior isotropic resolution is reported using isTIR compared to sTIR. LSQR based hybrid regularization is investigated to deal with the increasing complexity of the forward models. Few other aspects of the clinical handheld scanner like image slice thickness, noise and illumination profile are also investigated offering insights into further improvements. In summary, the methods and techniques proposed in this thesis directly addresses few of the challenges the clinical handheld scanner faces towards clinical translation.

1.4. Outline of the thesis

The work presented in the thesis is organized as follows:

Chapter 0 reviews the theory of optoacoustic image reconstruction briefly. It starts with the description of the forward model which deals with the conversion of initial pressure to detected signals. Then it describes the problem of inversion which deals with the formation of the image from the recorded signals. It also explains the advantages of the model-based reconstruction schemes citing relevant literature. The goal of this chapter is to introduce the relevant terms and theory behind the model-based reconstruction in optoacoustic tomography.

Chapter 3 describes the properties of transducers which can influence image quality and methods of characterization of optoacoustic system. It begins with the motivation behind the study of transducer properties and characterization of imaging systems. Then, it illustrates the concepts of spatial and electrical impulse response related to the shape and material properties of the transducer. It reviews the characterization techniques for medical ultrasound and discusses the challenges of full experimental characterization of the optoacoustic tomography systems with relevant literature review. Estimation techniques of some specifications of the imaging system such as resolution, image slice thickness, illumination profile and noise are presented. Then, the mathematical model of optoacoustic wave detection is presented along

with the forward model based on constant acoustic speed. This model is equivalent to the existing models based on constant acoustic speed. It forms the basis for evaluation of the performance of the models proposed in the next chapters.

Chapter 0 introduces the proposed sTIR model consisting of the experimentally derived average EIR of all transducer elements and numerically simulated SIR. First the motivation behind the development of sTIR characterization method is stated highlighting the challenges of pure dense grid full FOV TIR characterization. Then the importance of modelling refraction owing to the effects of coupling medium is discussed. Thereafter, the dependence of the sensitivity field of the transducer probe on the refraction is analyzed with the introduction of the concept of virtual source. The steps required to construct the sTIR mode are explained in detail along with the description of the image correction procedure using sTIR. Next, the experimental results evaluating the performance of the sTIR model using phantoms and clinical scans are presented. Additional numerical simulation is also presented to highlight the negative effects when the transducer properties are neglected. The robustness of the sTIR model towards slight change in assumed acoustic speed in tissue is also evaluated for a clinical scan. Finally, the advantages and limitations of the sTIR method is summarized.

Chapter 5 proposes a robust method to characterize the EIR of individual transducer elements using sparse measurements. It starts with the motivation behind the investigation of the variation of the electrical impulse responses across the transducer elements of the array. The problem to derive the EIR of a particular transducer element using sparse point source measurements is formulated using a set of linear equations. Next, the individual EIRs are obtained for solving the problem using regularized least squares and combined with the simulated SIR to construct the comprehensive model called isTIR. Thereafter, it presents the experimental results evaluating the performance of the isTIR using phantoms and clinical scans. Finally, the achievements of correcting for individual transducer element responses were summarized and limitations were discussed.

Chapter 0 addresses the problem of increasing computational load due to incorporation of transducer properties into the forward model. First, it investigates the issue of increasing size of the model matrix in the perspective signal quantization and sparsity of matrices. Then it explores the concept of hybrid regularization capitalizing the LSQR based inversion scheme which is suitable for the matrices dealt in this work. It also exhibits the equivalence between the direct regularization scheme and the iterative method with internal regularization. It presents

the LSQR type of method used to choose the regularization parameter for all reconstructions presented in this work. Finally, it concludes summarizing the current developments presented in this work and room for further improvements concerning design of stopping criteria for fully automatic choice of regularization parameter.

Chapter 0 finally summarizes the findings and the achievements presented in this thesis. It also provides an insight to the current limitations and open problems, showing directions of future research.

2. Brief theory of optoacoustic image reconstruction

This chapter provides a brief theory of optoacoustic tomographic image reconstruction to set the stage for a comprehensive treatment of handheld optoacoustic tomography in the later chapters. First the forward model is introduced wherein the problem of generation and propagation of optoacoustic wave is formulated. A discretized version of the forward model is presented in the tomographic setting as an introduction to the model-based reconstruction framework to be presented in later chapters. Then, the problem of inversion is discussed wherein the image is reconstructed from the recorded data. Different inversion schemes are reviewed which are popular in optoacoustic tomography. Finally, the advantages of model-based reconstruction scheme have been discussed with reference to already published literature. An argument is also provided to justify the choice of model-based reconstruction framework for the work presented in this thesis.

2.1. Forward model

When a region of homogenous fluid medium is excited by an optical pulse, acoustic waves are generated due to the thermoelastic expansion of the medium. Under the regime of thermal confinement [14] the acoustic pressure, $p(r, t)$ at a location r and at time t in a lossless medium obeys the optoacoustic wave equation [9], [96] which can be written as

$$\frac{\partial^2 p(r, t)}{\partial t^2} - c_0^2 \nabla^2 p(r, t) = \Gamma \frac{\partial H(r, t)}{\partial t}, \quad (2.1)$$

where H is the heating function and is defined as the amount of energy absorbed by the tissue sample per unit volume and per unit time. Γ is the dimensionless Grüneisen parameter [16] and c_0 is the acoustic speed in the propagation medium.

The solution of the inhomogeneous wave equation (2.1) using free-space Green's function can be written as [9],

$$p(r, t) = \frac{\Gamma}{4\pi c_0^2} \int \frac{dr'}{|r - r'|} \left. \frac{\partial}{\partial t'} H(r', t') \right|_{t'=t-|r-r'|/c_0}. \quad (2.2)$$

In order to satisfy thermal confinement [9], [14], [16] in time-domain optoacoustic imaging, the pulse duration of optical excitation is on the order of nanoseconds which is sufficient enough to avoid heat conduction into the neighboring areas of optically excited region. Hence, in

practice temporal heating can be approximated by Dirac delta δ such that $H(r,t)=H(r)\delta(t)$, and (2.2) can be expressed as

$$p(\mathbf{r},t) = \frac{\Gamma}{4\pi c_0^2} \frac{\partial}{\partial t} \int \frac{H_r(\mathbf{r}')}{|\mathbf{r}-\mathbf{r}'|} \delta\left(t - \frac{|\mathbf{r}-\mathbf{r}'|}{c_0}\right) d\mathbf{r}', \quad (2.3)$$

which is useful to derive the acoustic pressure generated by an optically absorbing object on absorbing energy H_r . The integral in (2.3) depicts the summation of optoacoustic pressure field $p(r,t)$ intercepted by an ideal point detector located at r due to excitation of point absorbers located on surface of a spherical shell centered at r with radius $|r-r'|$ as shown in Figure 2.1. Further, the radius of the spherical shell varies to enable acquisition of time series data at the detector located at position r .

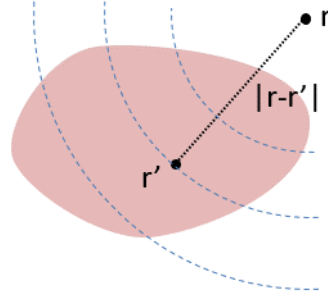


Figure 2.1: Geometry of inverse source detection. Illustration of inverse source detection problem showing ideal point detector located at r intercepting the pressure generated at object location r' lying on the surface of a spherical shell of radius $|r-r'|$

In quantitative optoacoustic tomography the goal is to determine the optical absorption distribution μ_a from the measured signals. This is usually done in two steps:

- i) the initial pressure p_0 is derived from the measured signals using (2.3) and $p_0=\Gamma H_r$.
- ii) the absorption coefficient is derived from the initial pressure using $p_0=\Gamma\mu_a\phi$, where ϕ is the light fluence distribution in the sample which could be estimated using light propagation models.

The optical inversion problem is out of the scope of the work presented in this thesis and hence $\Gamma\phi=1$ was considered for the sake of simplicity. Therefore, throughout the thesis the reconstruction of initial pressure as intensity of images were considered in the context of qualitative optoacoustic imaging.

Treating the optoacoustic wave detection (2.3) as linear problem, the signal measurement operator can be discretized in the form of matrices [94], [97]–[99]. A generic

tomographic imaging configuration was taken into account as shown in Figure 2.2 where the 2D image was discretized into $P \times P$ pixels and signals are measured at N locations around the sample to be imaged. The pixels were lexicographically stacked into $P^2 \times 1$ vector denoted by f , then measured signals at N projections around the imaged object were also stacked in a column vector s of dimension $NT \times 1$, where T is the length of acquired samples from each transducer. Hence, the forward model of optoacoustic imaging can be expressed as

$$s = Mf, \quad (2.4)$$

where M is the forward model matrix that maps the initial pressure f in arbitrary units to the recorded signal vector s . The dimension of system matrix is $NT \times P^2$, with its columns containing the acoustic response at the detector positions corresponding to each pixel. Generally, the pixels are modelled as a small homogeneously absorbing sphere generating ideal “N”- shaped [16], [100] optoacoustic response.

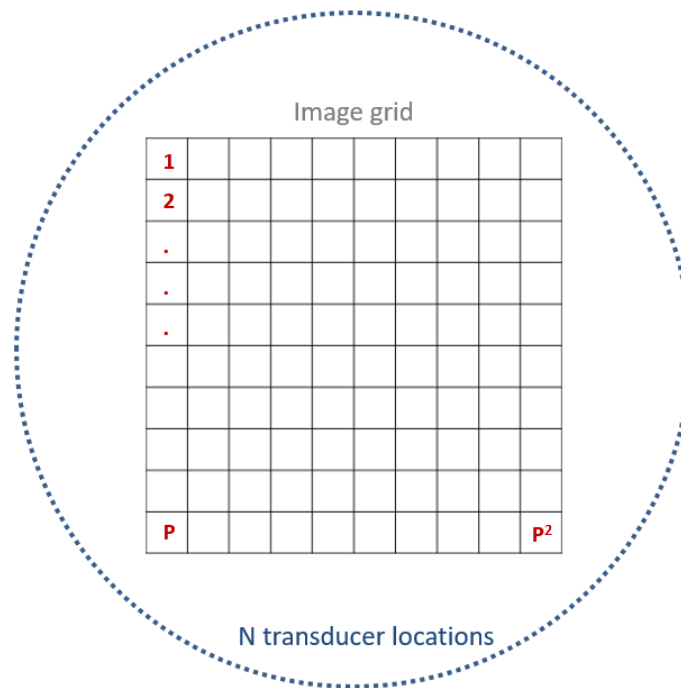


Figure 2.2: Discretization of optoacoustic wave detection. 2D image grid of $P \times P$ pixels surrounded by N transducer locations.

2.2. Inverse Problem

Inverse problem in tomography refers to the process of reconstruction of an image from the measured sinogram. In the context of qualitative optoacoustic tomography, it refers to the acoustic inversion which generates the initial pressure distribution from the recorded acoustic

signals. Figure 2.3 depicts the concept of forward and inverse problems. The forward problem refers to the generation of sinogram given the properties of the medium and detector location (2.3) as explained in the previous section. This section discusses the problem of inversion which deals with the generation of the image from the recorded sinogram data.

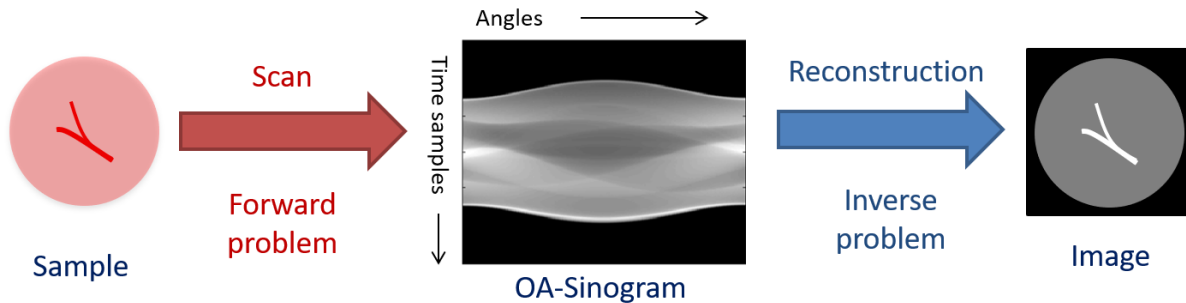


Figure 2.3: Concept of forward and inverse problem. The forward problem refers to the generation of the OA-sinogram from tomographic scan of the sample and the inverse problem refers to the formation of the image from the recorded OA-sinogram.

The commonly used time-domain reconstruction algorithms can be classified under two schemes – analytical inversion technique and model-based inversion technique.

Analytical inversion techniques tend to have a closed form analytical solution of the forward problem (2.2) - (2.3), quite similar to the inverse Radon transform. These algorithms (also called back-projection) in general consists of three steps [17] – preprocessing of recorded signals, back-projection over the image FOV from each detector and summation of the intermediate images obtained due to back projection from different detector positions. The use of back-projection algorithms can be traced to the very early developments in optoacoustic tomography [14] due to their simplicity and ease of implementation. An elementary form of back-projection is “delay and sum” algorithm [101] and a more sophisticated variant is universal back-projection algorithm [102] which offers exact solutions in planar, cylindrical and spherical geometries.

Model-based inversion techniques, on the other hand belongs to a class of algebraic techniques which numerically model the imaging system. Unlike analytical inversion methods, model-based inversion does not offer a closed form solution, instead they are iteratively [94], [99], [103], [104] solved by minimizing the error between the measured and the modelled data. Model-based inversion [97], [98] schemes can be used to closely model the components involved in the imaging mechanism thereby leading to an more accurate reconstruction results.

Nevertheless, this improvement comes at a computational expense comparatively higher than analytical inversion techniques.

2.3. Advantages of model-based reconstruction

The earliest developments in optoacoustic tomographic imaging made use of schemes like analytical or back-projection, which are well-established since decades in other imaging modalities namely X-ray computed tomography and Ultrasound imaging. The analytical reconstruction schemes being simple in implementation and computationally efficient were favored in the initial developments. With rapid progress in laser and ultrasound technology, the domain of optoacoustic imaging grew in length and breadth with search for new biomedical applications and growing demand for higher resolution, sensitivity and penetration depth. Back-projection schemes offer exact solutions, assuming ideal detection system, and hence in most practical cases these algorithms lead to artefacts, negative (unreal) contrast thereby hindering the image quality. Hence, it was soon realized that back-projection based schemes fails to cater to the growing need for better image quality and researchers ventured to explore various model-based reconstruction schemes. The inherent advantage of model-based reconstruction scheme lies in the fact that the physical aspects of the imaging system i.e. detector shape [74], [81], detector response [99], [105], light fluence [77], detection geometry [106], ultrasound attenuation [85], [96], etc. can be numerically modelled and hence leading to higher reconstruction accuracy. However, incorporation of complex imaging physics and iterative solutions are computationally expensive and time consuming. Fortunately, contemporary growth of computational power also facilitated the use of model-based inversion methods.

3. Transducer properties and characterization of optoacoustic tomography system

This chapter reviews the properties of ultrasound transducers which plays a key role in the resolution and quality of the reconstructed images produced by an optoacoustic tomography system. This chapter also presents methods to characterize few other important aspects of the optoacoustic tomography system such as – image slice thickness, laser illumination profile and noise.

First the motivation behind consideration of transducer properties is presented. Next, the impact of key transducer properties pertaining to the shape and material used on the impulse response is presented. Then the literature of clinical ultrasound transducer characterization is reviewed. Thereafter the method of characterization of optoacoustic imaging systems is presented in terms of – resolution, image slice thickness, laser illumination profile and noise. Later the entire optoacoustic wave detection pipeline from generation to recorded signals is modelled as a cascaded linear time invariant system where the transducer properties are included. Subsequently, the forward model including the total impulse response was formulated using constant acoustic propagation speed considering homogenous propagation medium. Finally, the implications of transducer properties are discussed. This is supplemented by the importance of characterization of the imaging system providing an outlook for possible research directions arising from analysis of noise, image slice thickness and inhomogeneity in illumination.

3.1. Motivation

The quality of images reconstructed in optoacoustic tomography strongly depends on the accuracy of the mathematical models of imaging physics coupled with transducer properties and instrument responses [73]–[81]. A hand-held optoacoustic imaging systems [49], [51] involves lasers, ultrasound transducers and coupling medium to produce an image and consequently the properties of each of these different components can influence the quality of the final optoacoustic image. Hence, it is imperative to study and evaluate the effects of these components to assess their impact on the quality of the resulting images. The geometric shape of the transducer aperture can be represented as spatial impulse response (SIR) and the receive-mode acousto-electric property of the transducer can be represented as electrical impulse responses (EIR). Then the whole transducer can be characterized using total impulse response (TIR) which is the temporal convolution of SIR and EIR. Numerical models for EIR and TIR

may be used to understand the image formation process. However, pure simulations often do not accurately model many aspects of the actual system which may lead to loss of image quality post TIR correction. The experimental characterization of TIR in general is a tedious procedure where a point absorber is scanned throughout the field of view (FOV) in a dense grid. Trivially speaking the EIR of a transducer can be measured [93], [107] by placing the point absorber at the focus of the transducer. However, in many focused transducer arrays, the foci are not the same point corresponding to each element, in such cases, placing the point source accurately to the focus of each transducer element can be dreadful especially for commercial (closed) imaging systems. Additionally, deviation of ultrasound propagation path due to coupling mismatches can adversely affect image quality. Therefore, EIR and TIR characterization of transducers presents a critical challenge.

It is to be noted that different facets of optoacoustic imaging has been explored to improve the resultant image quality by modelling underlying physics [14], [15], [97], using signal or image processing methods [98], [108] and deploying regularization methods [109], [110]. An appropriate combination of all these abovementioned methods may ideally result in best image quality. To reduce the computational burden in these algorithms' simple assumptions of point-like detectors are made and the frequency response of the detectors are also neglected. However, in most practical cases the transducer aperture sizes, and bandwidth limitations are significant and cannot be neglected without compromising the reconstructed image quality. Hence there is a need to study transducer properties and characterize the resolution of the imaging system which is directly affected by transducer properties [88]–[90]. Apart from characterizing the resolution of the optoacoustic imaging system, there are other specifications of the optoacoustic imaging system such as – image slice thickness, laser illumination profile and data acquisition noise which are influenced by the characteristics of the transducer and the design of the imaging system. Since these parameters also affect image formation process, a proper characterization of these parameters can lead to development of methods to improve the overall quality of reconstructed images.

3.2. Transducer properties

The motivation behind the modelling and characterization of transducer properties and their effects on the performance of the optoacoustic imaging system has been reviewed in the previous sub-section. The concepts of two fundamental properties of ultrasound transducers pertaining to its shape and frequency bandwidth will be elaborated herein. These two properties play a key role in dictating the resolution and shape of the absorbers in optoacoustic

tomography. The impulse response arising from the shape of the transducer aperture is called spatial impulse response (SIR) and the impulse response arising from the limited frequency bandwidth of the transducer is called electrical impulse response (EIR).

The theoretical concepts of these transducer properties will be illustrated using schematics and their implications with actual implementations will be discussed. Also, a brief review will be provided about existing literature attempting to model or characterize these transducer properties.

3.2.1. Spatial impulse response (SIR)

Assuming infinite bandwidth of detection, the response offered by the transducer due to its aperture geometry, on intercepting an acoustic impulse from a particular source is known as spatial impulse response (SIR) as illustrated in Figure 3.1. The spatial impulse response depends on the size, shape of the active surface of the aperture and the relative location of the origin of the impulse. Intuitively, SIR arises from the fact that the delta spherical wave when intercepted by the active surface of the transducer is smeared all over the active surface of the transducer as the incoming wave front reaches different locations on the transducer surface at different time points. On the other hand, an ideal point-detector with infinite bandwidth would produce an impulse on reception of a delta spherical wave originating from anywhere in 3D space.

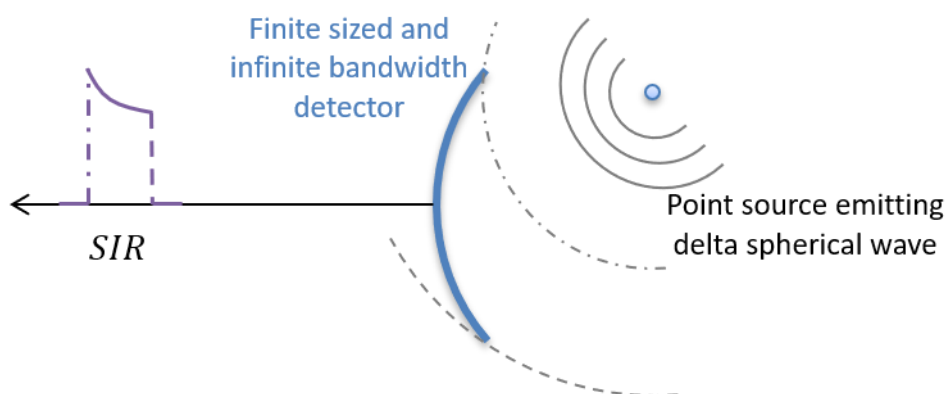


Figure 3.1: Concept of Spatial Impulse Response (SIR). Schematic illustrating finite sized detector of infinite bandwidth intercepting delta spherical wave from a nearby point source and producing spatial impulse response corresponding to the location of the point source.

Considering the ultrasound generation and detection process to be a linear system, by the virtue of reciprocity theorem the field generated at a point in space is equal to the SIR obtained from the detector while the same point is treated as the source. One of the earliest analytical solutions of SIR of planar pistons were proposed by Tupholme and Stepanishen

[111], [112] based on linear acoustics. The method finds the SIR by using Rayleigh integral over the whole surface or summing up the spherical waves generated from all over the transducer active surface. Analytical solutions can be found for only few transducer geometries, i.e. closed form expressions cannot be derived for all kinds of transducer configurations due to the difficulty of using Rayleigh integral over complex geometries [113], [114]. A powerful technique based on the Topholme and Stepanishen method to calculate the SIR for any arbitrary shaped transducer was first proposed by Jensen [113]. This method discretizes the transducer surface into small rectangular sub-apertures, calculates the field due to the small rectangles utilizing the far-field approximation and finally integrates all the responses to obtain the SIR. The technique developed by Jensen [113] to compute SIR for any arbitrary transducer shape is available in the Field II ultrasound simulation program [115].

The ultrasound transducers used in optoacoustic imaging work primarily in receive mode. The active surface of an ultrasound detector intercepts the incoming optoacoustic wave to generate an electrical signal. The amount of the signal is roughly proportional to the amount of the pressure wave intercepted and therefore to achieve higher signal to noise ratio larger apertures are preferred. In case of small animal imaging full angular view transducers are preferred where sample to detector distance is significantly higher than the dimensions of the transducers. This facilitates imaging in the far-field region and hence the distortion of the recorded optoacoustic signals due to SIR is significantly less. However, in the case of clinical handheld optoacoustic imaging, the sample to detector distance is not negligible compared to the dimensions of the transducers. In fact, tightly focused large transducer apertures are preferred to achieve high signal to noise ratio in the image plane. Such compact geometry may lead to strong SIR based distortion of the signals due to operation close to near-field region. Hence, it is beneficial to consider SIR of the transducer probe in case of compact handheld optoacoustic imaging. SIR simulation of the handheld transducers used in this work will be elaborated in detail in the Section 3.7 and Chapter 0.

3.2.2. Electrical impulse response (EIR)

Under the assumption of point-like detector, the response of the detector to an incoming delta spherical wave is known as electrical impulse response (EIR) as illustrated in Figure 3.2. The EIR in frequency domain defines the bandwidth limitation of the transducer. From system point of view the transducer acts like a band-pass filter with the center frequency being the resonant frequency and the lower and higher cutoffs defined by the material of construction and

transduction electronics. It is important to note that the EIR of a transducer is independent of location of the source of acoustic impulse.

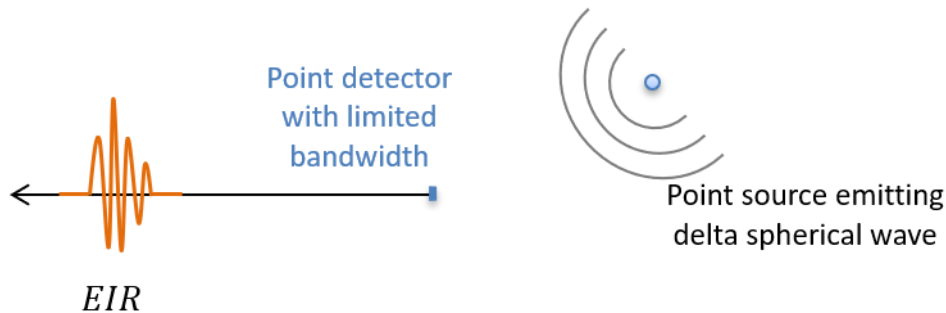


Figure 3.2: Concept of Electrical Impulse Response (EIR). Schematic illustrating point detector of finite bandwidth intercepting delta spherical wave from a nearby point source and producing electrical impulse response corresponding to the frequency response of the transducer and transduction electronics.

Piezoelectric materials have been extensively used for manufacturing of medical grade ultrasound transducers [116], [117]. Depending on applications piezoelectric transducers come in a range of sizes, shapes, center frequency and bandwidth of operation. Historically, elementary piezoelectric transducer [116] having a piezoelectric slab and two electrodes were represented by a general purely lumped RLC equivalent circuit [118], [119] to study the transducer impedance as a function of frequency. Since, then extensive research has been done to refine the equivalent circuit to effectively design piezoelectric transducers for example analysis of the multiple refractions due to acoustic impedance mismatch on both sides of the piezoelectric slab [120]. The most widely used equivalent circuit model is the KLM model named after Krimholtz-Leedom-Matthaei [121]. The KLM model is similar to the previously developed models in terms of thickness expander mode [116] of transducer design suitable for producing medical ultrasound transducers. The KLM model is advantageous over the previous models in separating the acoustic and electrical paths of the transducer offering more flexibility in the design and analysis. The KLM model represents a three-port network, where two ports are modelled as acoustic loads - tissue/coupling medium and backing material. The third port is represented as electrical load. This model is well-established in transducer manufacturing practice and often the model (Matlab) along with the model-parameters are available from the transducer vendor with special request. It is worthy to note that these electro-mechanical models and equivalent circuits are primarily used to design transducers, to predict the approximate acousto-electric response. Nevertheless, the actual acousto-electric response might be slightly

different from the responses predicted from these models. This may be attributed to the additional effects of thickness of electrodes, electronics, packaging etc. Therefore, transducer manufacturers generally provide the experimentally characterized acousto-electric response in the respective datasheets.

Optoacoustic signals are inherently broadband [16] in nature. Consequently, transducers with large bandwidth would be ideal for optoacoustic imaging. In practice, transducer bandwidth for a particular application [122] is chosen based on size of objects to be imaged, depth of imaging etc. For instance, in microscopy transducers with center frequency of about 40MHz and bandwidth as large as ~40MHz are chosen to image objects in the scale of tens of microns at shallow depths. In case of tomography transducers with center frequency of about 4MHz and bandwidth around ~4MHz would be a good choice to image as deep as 4cm inside soft tissue with a resolution of around hundreds of microns. In either case the generated broadband optoacoustic signals are bandpass filtered with the transducer EIR and then recorded. Therefore, EIR characterization of the transducer is immensely valuable in order to recover the broadband optoacoustic information. This can be achieved either by direct deconvolution [105] or by incorporation into the forward model [74]. Framework of inclusion of EIR into forward model will be discussed in Section 3.7 and later derivation of EIR using experimental techniques will be elaborated in detail in Subsection 4.5.3 and Subsection 5.2.3.

3.3. Characterization of transducers for medical ultrasound

It is of utmost importance to characterize transducers for medical ultrasound [123]. The resolution and sensitivity achieved in the ultrasound images can be greatly affected by the pressure field generated or the response recorded by the transducers. Also, for therapeutic ultrasound focused transducers are used where unregulated power levels may cause damage to human body [124]. Therefore ultrasound transducers must undergo rigorous characterization for quality control and certification procedures [125]. The development of sophisticated transducer modelling methods [126] also promoted the possibility to include the transducer characteristics into image reconstruction framework eventually improving image quality. In addition to that comprehensive characterization of transducers [91], [125] is also beneficial to detect faulty or dead transducer elements and very importantly capturing the inhomogeneity in responses of individual transducer elements in the array which can be included into reconstruction as prior information.

Characterization of medical ultrasound transducers can be performed in different ways taking the advantage of the reciprocity theorem [127] of ultrasound detection and generation.

The most common method is the pulse-echo characterization [123], [128], [129] where the transducer is excited with an electrical pulse and the pressure bounced back from a highly reflecting target (e.g. solid sphere or plate made of steel) kept at focus, and recorded by the same transducer. This does not require any secondary measuring instrument and therefore has been standardized in manufacturing practice. The pulse-echo method is only suitable to characterize the transducer close to the focus of its sensitivity field. However, for research and development of novel transducer types acoustic characterization in the full 3D space including sidelobes of sensitivity field would be necessary. Such characterization can be done in a temperature-controlled water bath by exciting the transducer and recording the pressure waves at different locations in space using a reference detector – hydrophone [91], [130] or laser interferometer [131]. Note that the response of the reference detector should be known in advance or well calibrated which is a challenge. The characterization using the reference detector requires accurate scanning of all possible locations close to the transducers which makes this method extremely time consuming [125], [126] and this led to the development of various ultrasound field simulators like Field II [115] and k-Wave [132]. In the recent years computational power of modern computers is leveraged to evaluate comprehensive numerical models [126] to study ultrasound wave propagation, detection and analyze the characteristics of the transducer arrays for different applications.

3.4. Characterization of transducers for optoacoustic tomography

In the previous section the importance of characterization of medical ultrasound transducers were discussed and existing literature concerning various characterization methods have been reviewed. This section provides insight into characterization of transducers for optoacoustic tomography.

The frequency response or EIR of transducers of medical ultrasound are characterized in pulse-echo mode using plane waves as most of them operate in the same mode. Since optoacoustic imaging operates in the receive mode the frequency response found using pulse-echo mode cannot be directly used in optoacoustic imaging. This makes it necessary to develop receive-mode frequency characterization methods specifically suited to optoacoustic transducers. Also, traditionally short pulses [133] and discrete frequency tones [134], [135] are used to characterize medical ultrasound transducers. Optoacoustic imaging on the other hand being a broadband imaging modality, it is important to characterize the response of transducers to the broadband frequency spectrum generated on exciting a point source. These has been addressed by Rosenthal [107] who proposed several methods to determine the frequency

response of ultrasound transducers for optoacoustic imaging systems. Among these the method of frequency characterization using optically excited point source [93], [136] is the most popular one. This popularity of this method lies in the fact that it is easy to implement. For instance, spherical microsphere of certain dimension is easily available, and this microsphere needs to be illuminated either by flooding the volume with laser illumination or using a sheet of light. There is additional requirement of light focusing optics. Also, this single microsphere being a lightweight target can be easily placed at a predefined co-ordinate location using low-cost linear motion stages. Subsequently, the EIR can be obtained by placing the point source at the focus of a transducer.

The SIR of the transducers cannot be directly measured by experimental means. This is since the recorded signals will always be convolved with the EIR and therefore EIR should be derived in order to deconvolve the recorded signals and obtain SIR. Therefore, a preferred method is to simulate the SIR using some ultrasound simulation software like Field II. The total impulse response (TIR) which is the temporal convolution EIR and SIR is more important to characterize in the context of optoacoustic tomography. There are two ways to characterize the TIR [93] of a transducer – purely experimental and hybrid.

In purely experimental characterization of TIR, a small microsphere mimicking a point source is optically excited to generate broadband acoustic waves. The point source is then scanned throughout the FOV – 2D/3D depending on tomography/volumetric imaging. An example of raster scan of the whole 2D field of view using a point source is illustrated in Figure 3.3. This can be achieved using linear translation stages stacked in two or three axes. In this method the programmable stages are synchronized with Laser trigger and data acquisition. The recorded signals represent TIR of the imaging system. The advantage of this method lies in the fact that the exact TIR can be measured at any location. However, to obtain TIR in whole FOV one should scan in dense grid which would be extremely time consuming. This may lead to system instability in practical situations owing to laser overheating and memory overflow. Since this method requires control of laser trigger and data acquisition, it is not suitable for characterization of TIR of closed systems i.e., commercial systems.

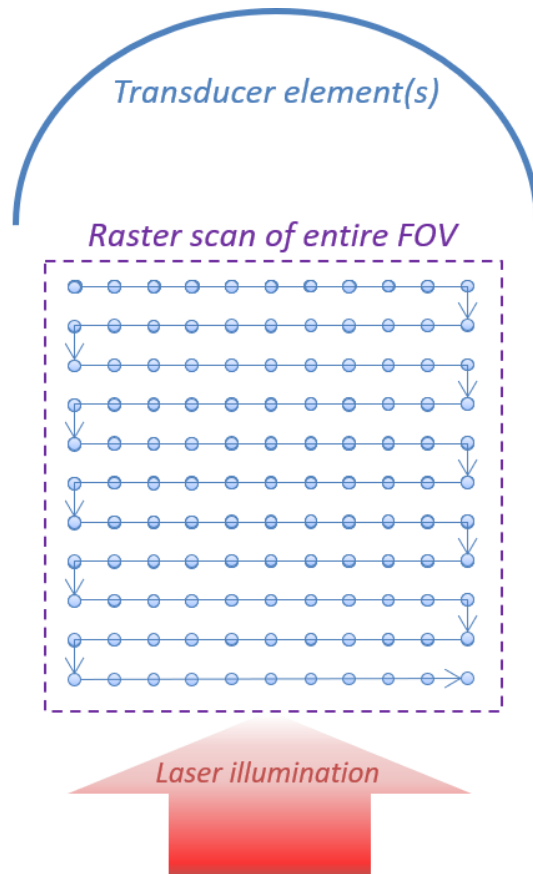


Figure 3.3: Schematic of typical characterization of optoacoustic imaging system. Illustration of typical optoacoustic characterization of transducer element(s) using raster scan of a point source excited with laser irradiation.

In the hybrid method of TIR characterization, the experimentally obtained EIR is combined with simulated SIR. The EIR is measured experimentally placing the microsphere at the focus of the transducer. At the focus of the transducer the SIR is a delta function and therefore this direct experimental EIR measurement is feasible provided it is possible to accurately place the point source at the focus. The SIR on the other hand is simulated in the whole FOV using an ultrasound simulation program. Subsequently combining the measured EIR and simulated SIR using temporal convolution the hybrid TIR can be obtained.

3.5. Specifications of optoacoustic tomographic imaging system

After having reviewed the methods of characterization of the transducers for optoacoustic imaging it is important to evaluate their effects on the performance of the system. This section elaborates on the specifications of a typical optoacoustic tomography system such as resolution,

image slice thickness, laser illumination profile and noise. These specifications indicate the performance of the imaging system in the clinical setting.

Like any other tomographic imaging modality optoacoustic tomography heavily relies on the combination of the imaging instrument and mathematical computation. Hardware components such as detectors, amplifiers and acquisition electronics used for ultrasound imaging are often used for optoacoustic imaging with some modifications. In addition to that high energy pulsed lasers are used along with focusing optics and diffusers to offer uniform illumination to the sample. These components are designed to follow certain operational characteristics e.g. bandwidth, sensitivity, homogeneity, noise etc. The characteristics or responses of the imaging components will affect the performance of the imaging system. Therefore, it is crucial to evaluate these performance metrics.

3.5.1. Resolution

Resolution achieved in the reconstructed images is one of the most important specification of an optoacoustic imaging system. The resolution of an optoacoustic imaging system determines the clinical application of the system. For example, for imaging bulk soft tissue a resolution of around 200 μm is sufficient, while for imaging microvasculature a resolution of <50 μm would be necessary. In general, the higher the resolution achieved the better the information rendered for clinical applications. However, in practice a tradeoff must be considered depending on the frequency of the transducers used and the depth of imaging.

The resolution is primarily affected by the frequency bandwidth and the dimensions of the aperture of the transducer being used. This dependence of resolution on bandwidth and aperture size of the detectors were studied analytically [88]–[90]. It was observed that the effect of frequency bandwidth was spatially invariant while the effect of aperture size was spatially variant. This is due to the fact that EIR is independent of source location and SIR is dependent on location of source as mentioned in Section 3.2. It was also observed that the bandwidth would affect both lateral and axial dimensions equally. However, the aperture size would affect the lateral resolution strongly and the axial resolution weakly.

Analytical expressions[88] of resolution was derived under straight forward assumption of “flat top” frequency response of the transducer as $R_{FWHM} = 0.7952 c/f_c$. Here, R_{FWHM} is the resolution presented in terms of full width half maximum (FWHM) of the resultant point spread function (PSF). c and f_c are defined as acoustic speed and cutoff frequency of the transducer. For example, considering acoustic propagation speed to be 1500m/s, a transducer with typical

cutoff frequency of 6MHz would result in a resolution of 200 μ m. It is important to note that this is only a theoretical estimate based on the assumption of “flat-top” frequency response, which is not the case in practical transducers. Therefore, it is imperative to experimentally measure the resolution of a developed optoacoustic system as it can be traced from the vast amount of literature. Reviewing each of the experimental methods to measure resolution of variety of optoacoustic imaging systems is out of the scope of this thesis. However, a brief overview of the method is outlined. Most of the experimental methods to characterize resolution [107], [136] of the system involved measuring optoacoustic signals generated from a black optically absorbing microsphere or suture of diameter less than the theoretically achievable resolution. The theoretically achievable resolution would be calculated using the transducer cutoff frequency in the analytical expressions discussed before.

One of the foremost goals in the domain of optoacoustic imaging is to achieve higher resolution. In order to accomplish this, research is being pursued in the different avenues of novel detectors, scanning configurations, reconstruction algorithms etc. The aim of the work presented in this thesis is to achieve higher resolution images by incorporating handheld scanner properties into the reconstruction algorithm. Therefore, the matter of experimental measurement of resolution will be dealt in details in the Subsection 4.7.1 and Subsection 5.4.1.

3.5.2. Image slice thickness

The thickness of image slice achieved in a tomographic imaging system is also an important specification and has certain clinical significance. Typically, focused transducers are used in majority of the modern optoacoustic tomographic platforms which tend to attain high sensitivity in the plane of image. Intuitively this leads to selection of slice of certain thickness where the image is averaged with certain weights along the axis perpendicular to the image plane. Therefore, the portion of the object lying within the slice thickness will be eventually averaged in the reconstructed image. This leads to reduced resolution and in worse case may lead to creating false structures when two thin blood vessels are placed close to each other. Naturally, the goal should be to achieve as thin slice as possible for clinical applications.

A method of estimating the slice thickness of a typical handheld optoacoustic tomographic scanner is presented next. First, the relation of image slice thickness to the transducer properties is explained and then simulation/experiments using an actual transducer is presented. The image slice thickness is mainly dictated by the elevation sensitivity field as illustrated in the schematic shown in Figure 3.4. Let us consider the situation of a cylindrically focused transducer array of which a single transducer is depicted with the blue curved line in

Figure 3.4. The sensitivity field map in the elevation plane or y-z plane is shown in blue shaded area marked with dashed magenta box. The image plane in the azimuthal plane is marked using dash-dot red line. The slice thickness is marked at the tapered region of the sensitivity field. A more realistic version of the definition of slice thickness from elevation sensitivity field is presented next using actual transducer.

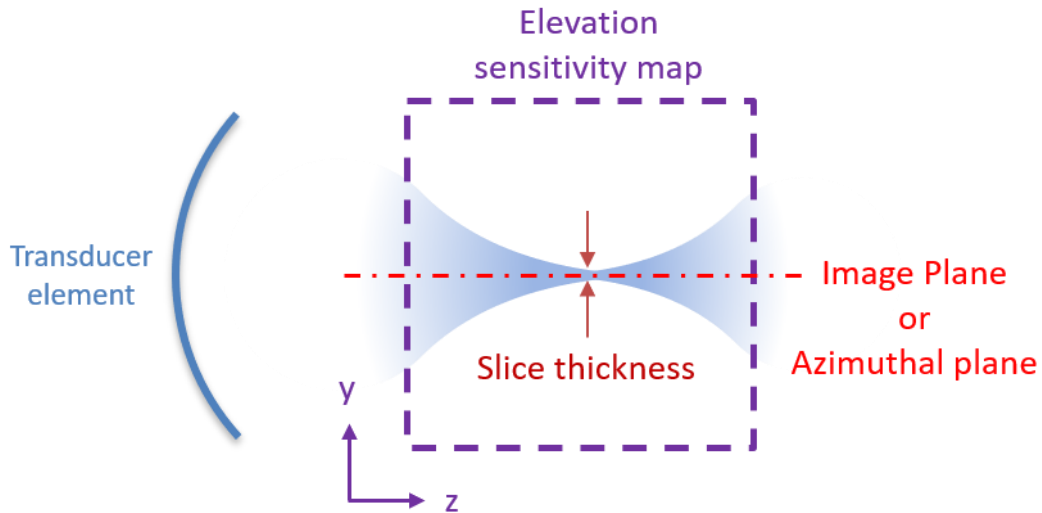


Figure 3.4: Illustration of slice thickness using the sensitivity map in the elevation plane. Schematic showing elevation sensitivity map of cylindrically focused transducer element, the central axis lying on the image plane or azimuthal plane and the metric of slice thickness at the location of highest acoustic focus.

Measurement of thickness of image slice using inclined sutures is proposed here. The concept is illustrated using a schematic in the Figure 3.5a. The black solid line indicates the absorbing suture at an angle of inclination θ with the image pane or the azimuthal plane marked with dash-dot red line. The projection of the suture in the image would be the length which is marked using dashed black line. The projection of the suture on the axis perpendicular to the image plane gives the slice thickness at that location. If the angle of inclination θ is known, then the slice thickness can be determined as $t_{slice} = l_{suture} \cdot \tan \theta$, where l_{suture} represents the length of the suture projection in image plane. Based on this principle an inclined suture phantom has been designed as shown in Figure 3.5b-d. Figure 3.5b shows the front view of the 3D CAD model of the suture holder in grey and the black lines represent five sutures at various angles - 45° , 63.4° and 90° . Figure 3.5c displays the same suture holder from the top where the weaving of the suture through the holes of the suture holder can be observed. The suture holder contained holes of around $200\mu\text{m}$ in diameter to allow weaving of suture with diameter $50\mu\text{m}$. The suture

holder was fabricated using a 3D printer and the suture was carefully interwoven as shown in the photograph of Figure 3.5d. The suture used in this case was of surgical grade and was made of black absorbing material suitable for optoacoustic imaging.

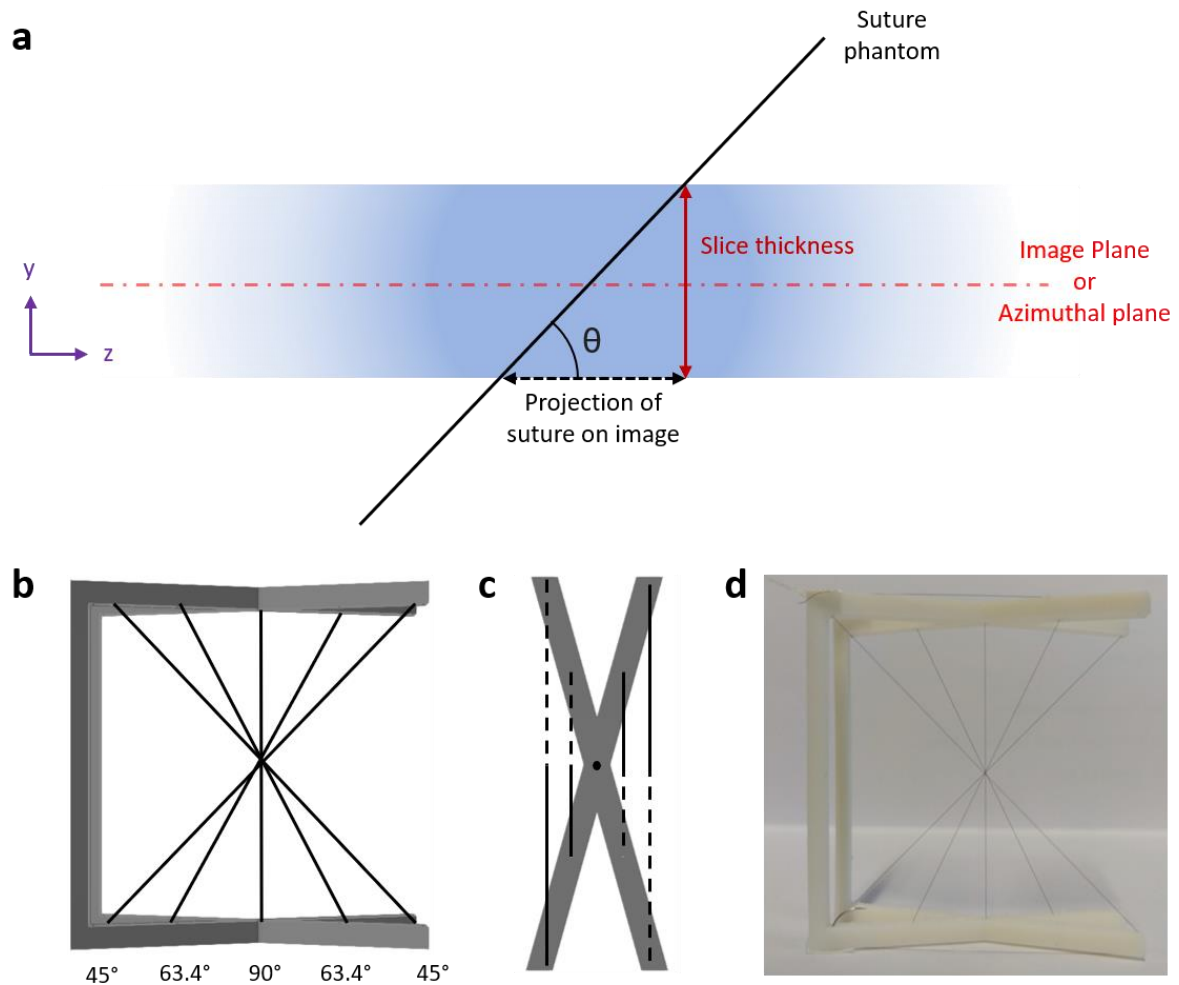


Figure 3.5: Construction of phantom to characterize the image slice thickness. Concept of inclined suture phantom was used to characterize the image slice thickness of tomographic optoacoustic setup. **(a)** Illustration of the concept of measuring image slice thickness using inclined suture phantom with known angle of inclination. **(b)** Front view of the 3D CAD model of the phantom showing five sutures at three different angles of inclination - 45°, 63.4° and 90°. **(c)** Top view of the 3D CAD model of the phantom showing the five sutures which would appear in the cross-sectional tomographic image. **(d)** Photograph of the phantom showing the suture woven into the 3D printed structure of phantom.

The suture phantom was scanned by the optoacoustic tomographic system in a turbid aqueous medium. Milk was added to the water bath to provide scattering for the incident laser

illumination. Prior to experimental measurements of slice thickness, some theoretical estimates were done using simulation. The sensitivity field of the cylindrically focused transducer array in the elevation plane or y-z plane is displayed in Figure 3.6a. Figure 3.6b displays the contour plots of the corresponding sensitivity field shown in the panel 12a. In the contour plot of panel 12b, the region segmented in yellow indicates the -6dB sensitivity region and the region segmented in blue indicates the -20dB sensitivity region. The -6dB region indicates the slice thickness in this case. It was observed that not only the slice is non-uniform but also it is asymmetrical. This can be attributed to the fact that the transducer used had limited angular coverage of only 145°. The elevation sensitivity maps and contours shown in Figure 3.6a-b are based on the side view of the transducer array. The cross-sectional optoacoustic image reconstructed from the signals recorded from the inclined suture phantom is shown in Figure 3.6c. The five crossing sutures are clearly visible in the image with a visual indication of the sutures with varying length of projections. However, to calculate the slice thickness proper quantification of the lengths of the sutures is required. Therefore, Figure 3.6d shows the lengths of the projections from the inclined sutures marked in solid green lines. The lengths of the projections of the sutures with inclination angles 45°, 63.4°, 63.4° and 45° are measured to be 4.69mm, 1.54mm, 0.98mm and 1.64mm respectively as shown using green line in the Figure 3.6d. The corresponding slice thickness in these respective locations were calculated using the relation $t_{slice} = l_{suture} \cdot \tan \theta$, to be 4.69mm, 3.08mm, 1.97mm and 1.64mm. Then, the locations of the sutures in the Figure 3.6d were marked along the z-axis in the contour plot of Figure 3.6b to derive the theoretical estimates of the thickness of image slice to be 2.8mm, 2.8mm, 2mm and 1.6mm. Finally, a strong correlation was found by comparing most of the theoretical estimates with the corresponding measured slice thickness. It indicates that this experimental method can be easily used to characterize the slice thickness of any optoacoustic tomographic imaging system without prior knowledge of the shape of the transducer aperture.

It is also observed that for the left most suture appearing in Figure 3.6c-d the experimental estimate of slice thickness being 4.69 mm is significantly higher than the theoretical estimate of 2.8mm. This abnormality can be attributed to the laser illumination aspects which will be explored in the next Subsection. Overall, an experimental method was demonstrated which can estimate the image slice thickness with fair accuracy as validated by simulation of sensitivity field in the elevation plane.

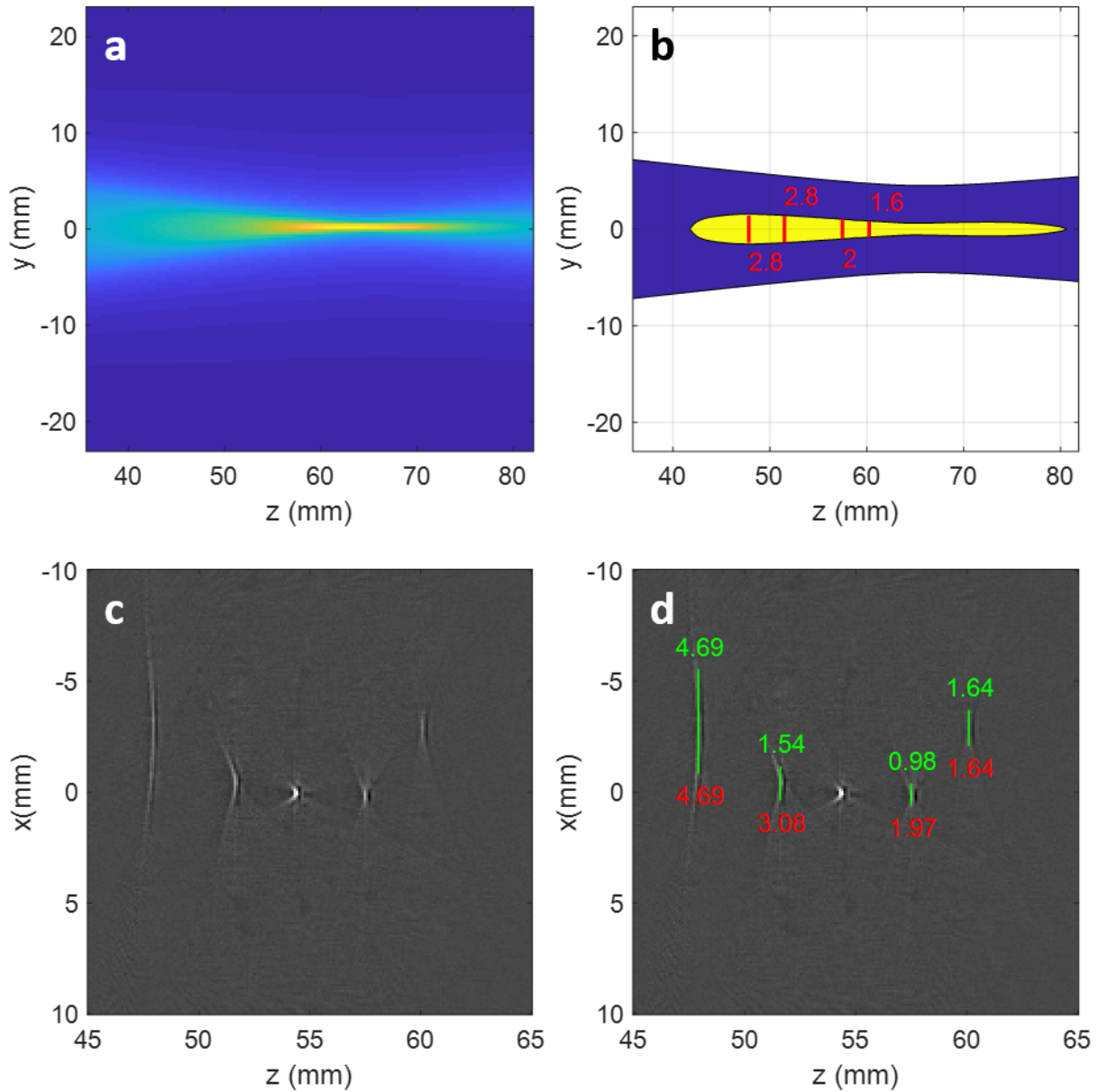


Figure 3.6: Characterization of the image slice thickness using cross-sectional image of incline suture phantom. The inclined suture phantom was scanned using the tomographic scanner and the cross-sectional image was reconstructed. The length of the suture images was correlated with the image slice thickness measured from the simulated sensitivity map in the elevation plane. **(a)** Simulation of the sensitivity map in the elevation plane. **(b)** The sensitivity map segmented with contour plot with -6dB region marked in yellow and elevation thickness marked in four locations in red. **(c)** The reconstructed image of the cross-sectional scan of the inclined suture phantom. **(d)** The length of the inclined sutures marked in green and the corresponding slice thicknesses are marked in red. Units of all measured lengths are in mm.

3.5.3. Illumination profile

The previous subsection dealt with the specification of the thickness of the image slice in optoacoustic tomographic imaging. An anomalous behavior was observed while characterizing the image slice thickness close to the transducer, precisely close to the interface of the coupling medium and the sample. This led to the exploration of the laser illumination profile incident on the surface of the sample, i.e. skin in the context of clinical applications. It is important to consider the profile of incident laser illumination along with the image plane during the design of a handheld transducer probe for clinical optoacoustic imaging. Ideally, the laser illumination should be homogeneously flooding the entire region of the skin in contact or at least be aligned with the image plane. In case of misalignment, the off-axis optoacoustic signals will be detected by the transducer and the resultant image may provide false structures or blur the vascular structures right underneath the skin.

The profile of incident laser illumination may depend on several factors such as the numerical aperture of the output of the optical fiber coupling laser illumination, the diffuser next to the optical fiber output, the angle of incline of the fiber output etc. One of the aims in optoacoustic tomographic imaging is to achieve higher depth of imaging in living tissue. Hence, light delivery angle and profile at incidence should be optimized to achieve deep tissue excitation along with maintaining synchronization with acoustic detection path. This aspect has been explored with Monte Carlo simulations [137] and experimental investigations [50], [138]. Since, laser light delivery is out of the scope of the work presented in this thesis, only characterization of the profile of the sample surface illumination will be explained and its implications in image reconstruction using acoustic inversion will be discussed.

The laser qualitative illumination profile on the surface was measured postprocessing a color photograph of the front face of the tomographic scanner covered with a thin sheet of white paper. The thin sheet was used to intercept the laser illumination mimicking the illumination on the surface of the skin. The image captured by a color camera was aligned with the actual scale in mm and the normalized profile is displayed in Figure 3.7a. The axis with the transducer sensitivity field coinciding with the image plane is marked using dashed red line aligned at $y = 0$ mm. It can be observed that the laser illumination is incident on the surface of the handheld probe has an offset of around 7 mm. This might be one of the reasons behind the anomalous behavior of slice thickness observed in the previous subsection. Again, two illumination spots are observed in Figure 3.7a. To evaluate the effect if this non-uniform laser illumination in the reconstructed images, a tissue mimicking turbid phantom was made of agar gel as the medium.

Milk was used to mimic scattering and India ink was used to mimic absorption. The phantom was scanned in the FOV of the handheld tomographic scanner and the reconstructed image is shown in Figure 3.7b. The two illuminations spots are clearly visible in the reconstructed images. In addition to that the fluence attenuation is nicely captured in the reconstructed image.

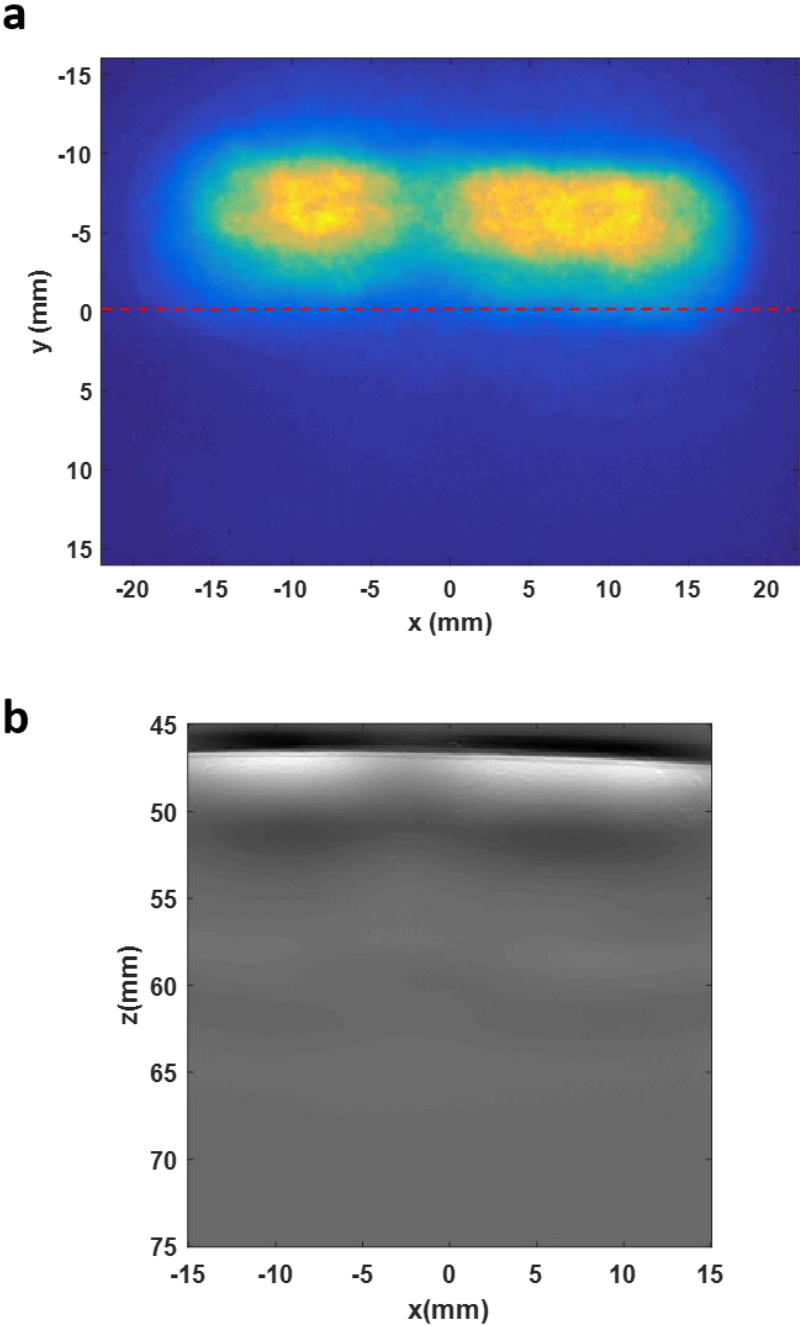


Figure 3.7: Characterization of the illumination profile. The illumination profile on the sample surface is characterized and effect on reconstructed image has been illustrated using homogeneously absorbing agar phantom mimicking soft tissue. **(a)** Normalized 2D illumination profile in the y-x plane at the top surface of the sample. **(b)** The reconstructed image of the soft tissue mimicking phantom

showing the effect of the inhomogeneous illumination on the surface of the sample. (Panel **a** was obtained in collaboration with Ph.D. candidate, Ms. Maria Anastasopoulou)

With carefully characterized laser illumination profile and carefully calibrated design of tissue mimicking phantoms, fluence maps can be obtained which can be used later for fluence correction. Overall, the importance of characterizing laser illumination has been discussed along with optical attenuation recovery using tissue mimicking phantoms can offer insights into fluence correction.

3.5.4. Noise

Noise in the measured signals can affect the resultant reconstructed images in an optoacoustic tomographic system in terms of artifacts and reduced sensitivity. Hence, noise is an important parameter which needs to be characterized and reported. Signal to noise ratio (SNR) of measured signals dictate the sensitivity performance of the tomographic system. For example, if the signal from the target optical absorber lies below the noise floor, then this object cannot be detected in the reconstructed image. Also, any other interference noise can produce artefacts in the reconstructed images.

Noise in optoacoustic tomographic imaging systems can have various origins. The most popular source of noise is the thermal noise in the electronics associated in the detection of signals. This thermal noise dictates the sensitivity of the imaging system [139]. Significant amount of noise can also be generated by the high energy pulsed lasers and importance of detection and removal of such noise has also been investigated [140]. Apart from the common thermal noise in electronics, strong intermittent ringing noise have been found while performing experiments reported in this thesis. In the reconstructed images this appear as ring-link artefacts. Interestingly the source of the noise was traced to the switched mode power supplies (SMPS). The frequency of appearance of these artefacts were in the range of few hundreds of kHz which matches with the switching frequency of the SMPS. Later, it was confirmed that placement of the SMPS close to the DAQ led to this interference. This can be a common issue for commercial optoacoustic scanners as they are compact in nature and hence care must be taken while designing of such systems.

The noise during signal acquisition was characterized while recording the signals by immersing the handheld tomographic scanner in water bath in the absence of any optically absorbing targets in the FOV of the scanner. Data from all the transducer 256 channels were recorded using laser excitation of wavelengths 700nm - 800nm in the range where optical

absorption of water is negligible. Figure 3.8a depicts the matrix of signals captured using the 256 transducer elements in the array with 2030 temporal samples in each signal. The intermittent horizontal lines represent the interference noise from the SMPS as marked using blue arrows. The dashed red rectangle marks the region between two consecutive interference noise. This region represents the pure background noise of the system which can be attributed to thermal noise. The histogram of this background thermal noise is plotted in Figure 3.8b. The red curve represents a Gaussian distribution with mean at 0 and standard deviation of around 0.4.

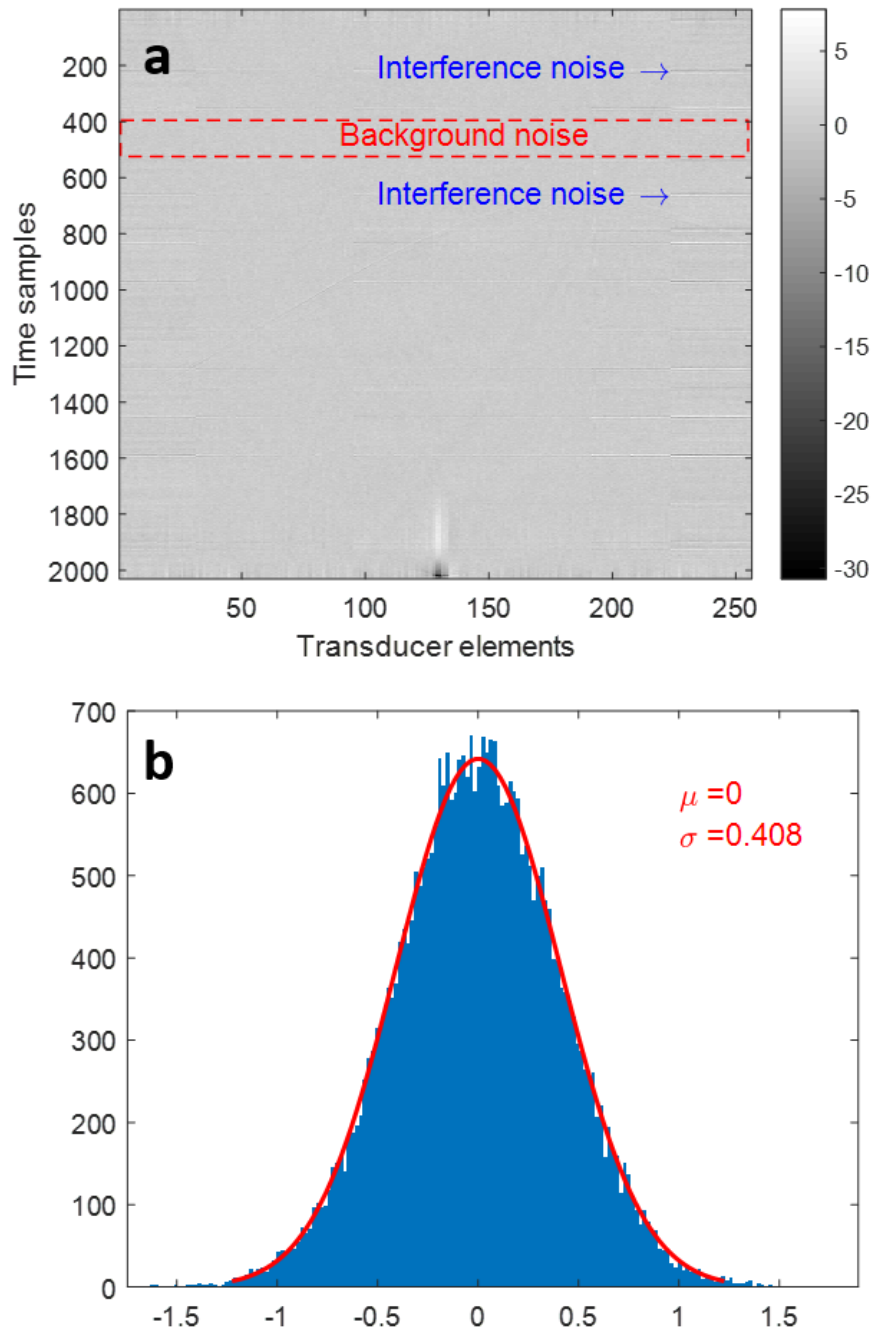


Figure 3.8: Characterization of noise. The noise in the data acquisition was characterized using data measured in absence of any optoacoustic absorbers. **(a)** The signal matrix in time samples vs transducer elements showing the interference and background noise. **(b)** The histogram of the segregated background noise showing the Gaussian distribution.

The noise characterization performed for the optoacoustic tomographic system could be used to define a stopping criterion in the inversion procedure using hybrid regularization. This exploration can be taken up as a future research direction. Also, the interference noise as described here seemed to be random in nature. These noise measurements were used to train a deep neural network to detect and remove this interference noise. The findings of this collaborative work have been considered for a publication mentioned in the list of publication at the end of this document.

3.6. Modeling optoacoustic wave detection

In order to integrate the transducer properties into the forward model, the optoacoustic wave detection mechanism needs to be investigated. To image deeper structures using optoacoustics, pressure in the range of Pa or sub-Pa needs to be detected [139], [141]. Therefore, the piezoelectric transducers widely used in optoacoustic imaging, tend to have a greater aperture size and a shape focused onto the imaging plane to better intercept acoustic waves and achieve higher signal-to-noise ratio (SNR). Also, the frequency response of the transducer is bandwidth limited and are often chosen based on the application. The shape of the transducer active surface can be characterized as SIR and the bandwidth can be characterized as EIR. With the goal to systematically investigate the effects of the transducer properties, namely shape and bandwidth, the optoacoustic wave detection mechanism was modelled. In most of the practical cases homogenous coupling medium is used such that the distortion and attenuation of the travelling acoustic waves are very negligible and hence it was safely assumed that the intercepted acoustic pressure is same as the initial pressure from the source. The intercepted acoustic wave is first averaged on the active surface of the transducer, a phenomenon characterized by the spatial impulse response or SIR as shown in Figure 3.9a. Thereafter, the combined process of energy conversion, analog amplification and digitization of the signal can be characterized as electrical impulse response or EIR. Reaping the advantage of model-based approach, the optoacoustic detection can be represented as a cascade of two linear time invariant (LTI) systems with impulse responses SIR and EIR respectively, as shown in Figure 3.9b. Finally the two LTI systems can be combined to characterize the whole optoacoustic detection using a transducer with TIR as shown in Figure 3.9c.

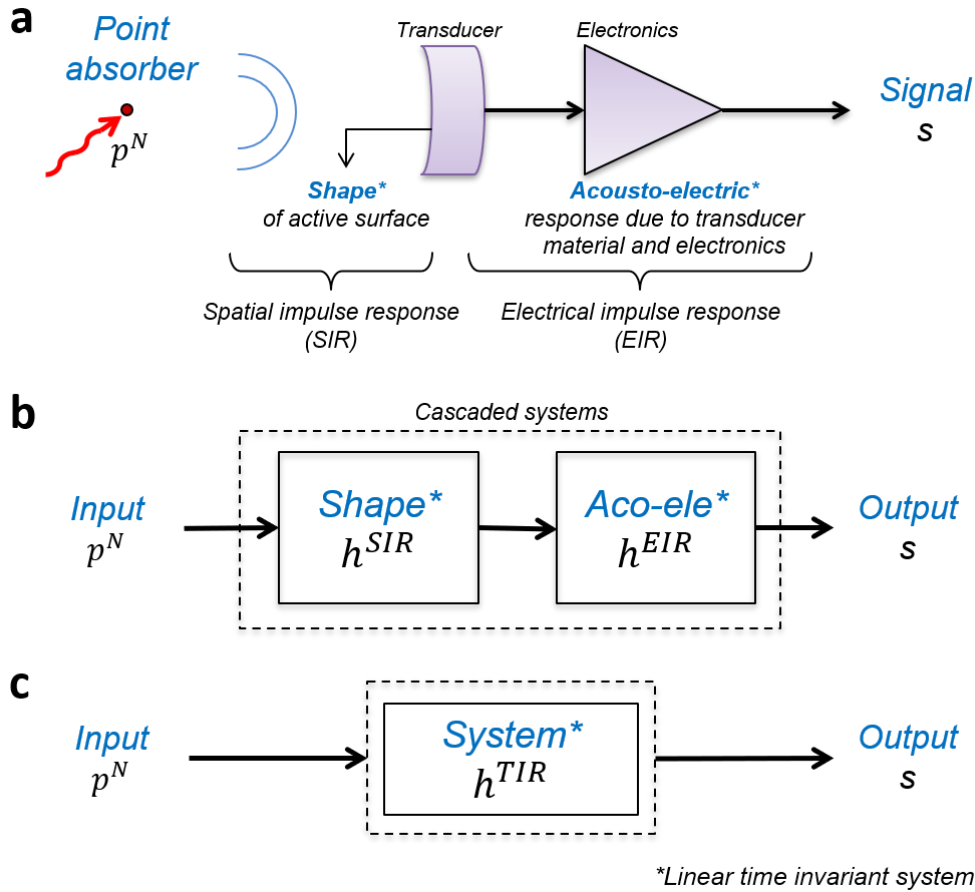


Figure 3.9: Physical characteristics of transducers. (a) The optoacoustic wave detection mechanism starting from incidence of pressure waves on the active surface of the transducer, subsequent acousto-electric conversion and finally resulting into recorded digital signals. (b) A cascade of two LTI systems representing the SIR and EIR (c) A resultant LTI system called TIR combining SIR and EIR.

3.7. TIR model for constant acoustic speed

As a basis for the TIR model with added transducer/coupling medium properties and for comparison with the established tomographic reconstruction methods, the TIR model for a constant acoustic speed was first studied. It was assumed that there was no significant acoustic speed mismatch between the sample and the coupling medium.

Figure 3.10 shows the straight-line propagation of an optoacoustic wave originating at the source r' and is detected by a transducer element at r_e of a curved transducer array in an acoustically homogeneous propagation medium with constant acoustic speed c_0 . Each transducer element is cylindrically focused onto the image plane, which is the xz -plane in Figure 3.10. The image is discretized into a collection of uniform spheres with diameter D in a Cartesian grid with spacing D . The general normalized analytical “N”-shaped optoacoustic

pressure wave [100] generated by a uniform spherical absorber of diameter D in a medium with acoustic speed c , can be written as [16], [100]

$$p_c^N(t) = \begin{cases} -t & , \quad |t| \leq \frac{D}{2c} \\ 0 & , \quad \textit{elsewhere.} \end{cases} \quad (3.1)$$

Thus, the signal $s_{r_e, r'}$ due to a pixel (modelled as a solid sphere) located at r' with initial pressure amplitude $f_{r'}$, that is detected by an ideal point-like transducer with infinite detection bandwidth at r_e and time t is

$$s_{r_e, r'}(t) = f_{r'} \cdot p_{c_0}^N(t - t_{c_0}(r_e, r')), \quad (3.2)$$

where the time of flight for constant acoustic speed c_0 along the straight line from the uniform spherical absorber to the point detector is

$$t_{c_0}(r_e, r') = \frac{|r_e - r'|}{c_0}. \quad (3.3)$$

Usually the transducer has a finite-sized aperture to intercept incoming acoustic waves. This results in averaging the intercepted wave over the active surface of the element S_e . Considering the acoustic detection as a linear system, the resulting acoustic response due to the surface of S_e is a temporal convolution [81], [142], [143] as follows

$$s_{r_e, r'}(t) = f_{r'} \cdot h_{c_0, r_e, r'}^{SIR} * p_{c_0}^N(t - t_{c_0}(r_e, r')), \quad (3.4)$$

where the SIR [113] is defined by

$$h_{c_0, r_e, r'}^{SIR}(t - t_{c_0}(r_e, r')) = \int_{S_e} \frac{\delta\left(t - \frac{|s - r'|}{c_0}\right)}{|s - r'|} dS(s). \quad (3.5)$$

In practice the detection bandwidth of a transducer is limited and characterized by the EIR denoted by $h_{r_e}^{EIR}$, which is independent of the origin r' of the signal. The $h_{r_e}^{EIR}$ term is added to (3.4), to get the following expression for the acoustic signal originating at location r' and detected by a transducer at r_e

$$s_{r_e, r'}(t) = f_{r'} \cdot h_{r_e}^{EIR} * h_{c_0, r_e, r'}^{SIR} * p_{c_0}^N(t - t_{c_0}(r_e, r')), \quad (3.6)$$

where $*$ denotes temporal convolution. Note, that (3.6) simplifies to (3.4) when setting $h_{r_e}^{EIR} = \delta$, and to (3.2) when in additional setting $h_{c_0, r_e, r'}^{SIR} = \delta$.

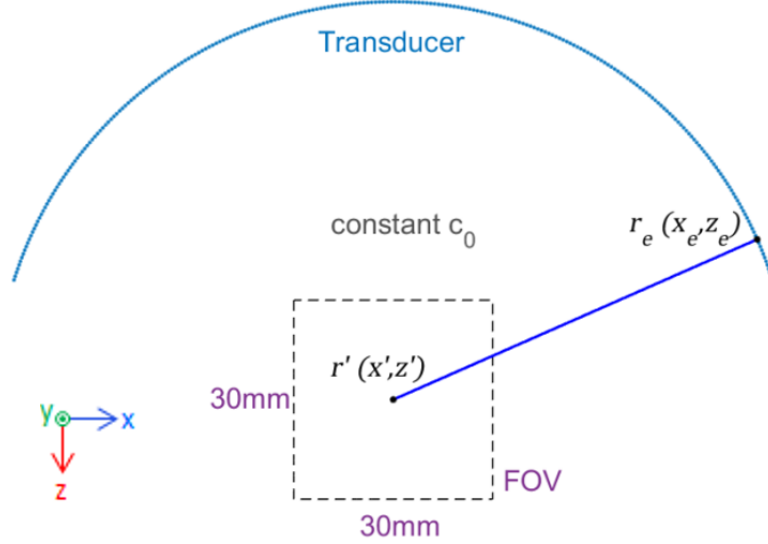


Figure 3.10: Schematic of limited view transducer using constant acoustic speed model. Illustration of propagation of pressure wave from a source point r' inside the FOV towards the transducer element r_e in the limited view transducer array, assuming homogenous propagation medium with constant acoustic speed c_0 . (Source: Adapted from [144], Copyright © 2020 IEEE)

The pressure signal $s_{r_e, r'}$ in (3.6) is sampled at T time points $t = n \cdot \Delta t$, where $n=0, 1, \dots, (T-1)$ and Δt is the sampling interval. To clearly distinguish between the continuous and the discrete signal, the sampling index was written in square brackets. The time index corresponding to the time of flight was denoted as n_0 and collecting the signals from all the points in the FOV, the following model for the measured acoustic signal with a constant speed of sound can be written as:

$$s_{r_e}[n] = \sum_{r' \in \text{FOV}} f_{r'} \cdot m_{r_e, r'}[n - n_0], \quad (3.7)$$

where

$$m_{r_e, r'}[n] = h_{r_e}^{EIR} * h_{c_0, r_e, r'}^{SIR} * p_{c_0}^N[n], \quad (3.8)$$

is the normalized contribution of a single spherical absorber at location $r' \in \text{FOV}$.

The pressure signal of length T samples, is recorded at the N locations of the transducer elements indexed by $r_e = 1, 2, \dots, N$. The location of the uniform spherical absorber r' in the FOV can be indexed by (i, j) where $i = 1, 2, \dots, P; j = 1, 2, \dots, P$, such that P^2 is the total number of uniform spherical absorbers in the FOV. Hence, (3.7) can be expressed in a matrix relation as

$$\begin{bmatrix} s_1 \\ s_2 \\ \vdots \\ s_N \end{bmatrix} = \begin{bmatrix} m_{1(1,1)} & m_{1(2,1)} & \dots & m_{1(P,1)} \\ m_{2(1,1)} & m_{2(2,1)} & \dots & m_{2(P,2)} \\ \vdots & \vdots & \vdots & \vdots \\ m_{N(1,1)} & m_{N(2,1)} & \dots & m_{N(P,P)} \end{bmatrix} \begin{bmatrix} f_{(1,1)} \\ f_{(2,1)} \\ \vdots \\ f_{(P,P)} \end{bmatrix}. \quad (3.9)$$

or,
$$s = \mathbf{M}f, \quad (3.10)$$

where
$$\mathbf{M} = \begin{bmatrix} m_{1(1,1)} & m_{1(2,1)} & \dots & m_{1(P,1)} \\ m_{2(1,1)} & m_{2(2,1)} & \dots & m_{2(P,2)} \\ \vdots & \vdots & \vdots & \vdots \\ m_{N(1,1)} & m_{N(2,1)} & \dots & m_{N(P,P)} \end{bmatrix} \quad (3.11)$$

is the model matrix of dimension $NT \times P^2$. Each element of the model matrix, $m_{r_e(i,j)}$ is a column vector of length T samples. Equations (3.1), (3.3), (3.5) - (3.9) comprise the complete model for the acoustic data acquisition at constant acoustic speed.

3.8. Discussion

This chapter has presented the concepts of transducer properties, reviewed transducer characterization methods, and introduced a general method to incorporate the transducer properties into the forward model of optoacoustic tomography. The chapter began with highlighting the importance of studying and characterizing the transducer properties for general optoacoustic tomographic imaging systems along with relevant literature. Thereafter, the concepts behind the key transducer properties of SIR and EIR were elaborated with description of methods of modelling or characterization of each of these impulse responses. Then the established methods of characterization of medical ultrasound transducers were reviewed. Since, ultrasound transducers are directly used for many optoacoustic tomography applications, the challenges of directly importing the standard pulse-echo characterized response was also discussed. The broadband nature of optoacoustic imaging demands for receive-mode characterization in full frequency spectrum. This was elaborated with reference to recently proposed methods suitable for characterization of transducers for optoacoustic tomography. Then the effects of transducer properties on several specifications of tomographic imaging was evaluated. Since majority of the thesis deals with characterization of resolution, only minimal

details were provided in this chapter. The characterization of image slice thickness, laser illumination profile and noise were demonstrated for a typical handheld tomographic imaging system. Finally, the modelling of optoacoustic wave detection using cascade of SIR and EIR was presented and the generalized incorporation of TIR into the forward model was presented with the assumption of constant acoustic speed.

The challenges of characterization of the TIR using purely experimental methods have been highlighted. A hybrid method used to characterize TIR using experimental measurement of EIR and numerically simulated SIR was traced in literature. However, this hybrid method has been so far implemented in cases of full angular view scanning systems considering constant acoustic propagation speed. There is still unmet need to characterize the TIR of the full handheld tomographic scanner with limited view transducer. This is particularly challenging due to the presence of significant acoustic mismatch between the coupling medium and sample. Methods to overcome this problem will be dealt in the next two chapters.

An efficient characterization of image slice thickness was presented using inclined suture phantom. The main finding was that with good accuracy it was possible to characterize a commercial (closed) system without any modifications using a 3D printed inclined suture phantom. The accuracy of this characterization was validated using the simulation of SIR map in the elevation plane. A limitation of the method was that it allowed characterization of slice thickness only at the location of the suture crossing and theoretically it was observed that slice thickness may not be uniform throughout the FOV. Also, the anomaly which was observed in the slice thickness prediction close to the transducer called for in depth investigation into the illumination profile measurements.

A simple method to characterize the incident laser irradiation was demonstrated. Like the previous method, this method was also suitable for commercial system in capturing the laser illumination profile with minimal modification. It was observed that the illumination was not uniform over the entire image slice. The outputs from two groups of fiber bundles results in formation of two blobs of illumination spots on the surface of the membrane. This was clearly visible in the reconstructed images of the turbid phantom mimicking soft tissue. It was several millimeters thick and was shifted by around 7 mm off the plane of highest transducer sensitivity. This is expected to severely effect the image quality. The region close to the skin will have strong out of plane signal while the regions deeper will have less fluence eventually leading to lower SNR. This can only be efficiently addressed with proper hardware configuration. Inspiration can be obtained from the studies which investigate the illumination angle and

localization for optimized light delivery [50], [138]. Other schemes including this offset into the forward models can also be explored in the future for compensating the effects of the inhomogeneous illumination.

The experiments to characterize background noise revealed two noise components – a) thermal noise arising from electronics and b) interference of low frequency noise generated from the switching mode power supplies. It was observed that the thermal noise can be modelled as a Gaussian noise with zero mean and is stable over time. However, the noise arising from interference of the switching in the power electronic circuit leads to fluctuating ring like artefacts across the frames. This is detrimental specially during unmixing of spectral stack to recover the chromophore maps. This is due to the fact that the pattern of this artefact changes from one frame to the next within the spectral stack. A deep learning method is in development using the characterized noise to eliminate this noise.

The modelling of the optoacoustic wave detection using linear time invariant systems as presented in this chapter has an imminent advantage of inclusion of the characterized responses of the components into the forward model. This also helps in proper understanding of the effects of each component which sets the stage for the analysis presented in the next chapters. The forward model including the transducer properties considering constant acoustic speed was introduced in the last section of this chapter. This will be used in the next chapter as a reference to compare the performance of the TIR models with added transducer/coupling medium properties based on the existing TIR forward model with constant acoustic speed.

Overall, this chapter introduces the concepts of key transducer properties SIR and EIR and also presents how these properties are expected to affect the image quality. The traditional methods for characterization of TIR are reviewed stating the advantages and gaps which still need to be addressed. Some specifications of a typical OAT system were discussed, and their implications were highlighted along with suggestions for future research directions. Finally, the linear time invariant model of the optoacoustic wave detection was presented which would be helpful to analyze the effects of each aspect of transducer modeling and also facilitates the inclusion of impulse response of each component.

4. A synthetic total impulse response for handheld tomography

This chapter introduces a TIR characterization method for handheld tomographic imaging systems. The previous chapter introduced the transducer properties and formulated the TIR model for the case of constant acoustic speed, and in this chapter, the forward model has been generalized to the case of refraction due to a significant acoustic mismatch between sample and coupling medium. To begin with refraction effects are modelled, then the SIR is simulated and thereafter EIR is derived and finally all the components are combined to obtain the synthetic TIR or sTIR model. The improvement of image quality is demonstrated using the sTIR models on physical phantoms and clinical measurements.

4.1. Motivation behind TIR characterization of handheld systems

Handheld scanners [31], [51], [52], [59] are suitable for clinical applications where the operator can simply position the handheld scanner in close contact with the skin applying regular ultrasound gel like established procedure in clinical ultrasound. Again, handheld transducers require transducer arrays with focused aperture and limited angular coverage enclosed with coupling medium in a chamber sealed with a flexible optically and acoustically transparent membrane. Hence, characterization of transducer array alone is not sufficient as the role of coupling medium and membrane interface becomes increasingly important. The mismatch between the acoustic properties of the tissue and the coupling medium can lead to refraction of ultrasound wave propagation ultimately adversely affecting image quality. Therefore, it is necessary to model and characterize the entire handheld probe.

Earlier work has demonstrated improvement in image resolution using EIR corrections for small-animal imaging systems with large angular projections [74], [105], [145]. The SIR correction has also been demonstrated to reduce aperture size related artefacts and nearfield artefacts in the case of animal imaging systems with large angular projections [74], [81], [146]. These techniques include the SIR into the forward model. Another technique to mitigate the SIR related affects was demonstrated in a post-filtering method [147]. Apart from investigating the individual effects of SIR and EIR, a TIR correction scheme has also been reported for small animal imaging system [74] with full angular coverage. This work also considers a constant acoustic propagation speed for developing the TIR model. While previous work with full-view acquisition systems has demonstrated image improvements after TIR correction, there is currently no systematic study that examines the effect of TIR correction in limited view acquisition geometries used for clinical handheld imaging [57], [92], [95], [148]. As mentioned

before a major challenge in clinical handheld scanners is the limited view acquisition geometry and coupling medium. A coupling medium of heavy water (D_2O) is often preferred to obtain good contrast of lipid, a clinically relevant endogenous chromophore [31], [149]. However, it appears that the acoustic speed mismatch between tissue and coupling medium may lead to refraction of acoustic waves which has not been thoroughly investigated. In addition to that the characterization of such handheld transducers becomes challenging due to the presence of delicate clinically compatible lasers since traditional dense grid scanning leads to laser overheating. As handheld scanners are increasingly considered for clinical studies [10], [23]–[25], [27], [36], an efficient TIR characterization becomes particularly important, as it relates to delivering high-fidelity images.

In this chapter, the aim is to decompose the TIR into its different components, to separately study/understand the refraction effects of the coupling medium, the spatial sensitivity field of the transducer array and the acousto-electric response of the transducer on the total impulse response of the handheld scanner shown in Figure 4.1a. It was hypothesized that refraction effects play a major role in image quality and their correction could lead to a more accurate model of TIR.

To achieve this goal, we propose a method to characterize the TIR of the clinical optoacoustic handheld system by using only one measurement of TIR and a detailed mathematical model. The main advantage of this approach is that it enables us to bypass the tedious procedure of conventional TIR measurements in dense grid of whole FOV. The proposed TIR model is called synthetic TIR or sTIR, as it is synthesized using experiments and numerical simulations. The sTIR model consists of simulated SIR and experimentally derived EIR. We demonstrate that the sTIR model can be effectively applied in case of significant mismatch of acoustic properties between sample and coupling medium. The refraction caused due to the mismatch of the acoustic speed between sample (eg. soft tissue) and coupling medium (eg. heavy water) alone can significantly influence image quality. Detailed analysis is provided on how the SIR depends on refraction. In order to model refraction and SIR; the shape of the transducer array and the membrane of the handheld scanner is modelled as illustrated in Figure 4.1b-d. The detailed SIR model including refraction was used to derive approximate EIR from experimentally measured TIR.

Finally, the sTIR forward model is used in model-based inversion scheme to demonstrate the improvement in resolution and accuracy of the reconstructed images throughout the FOV. To systematically study the effects of the components the sTIR –

refraction, SIR and EIR, six different forward models were constructed to evaluate each correction step. All the simulations and experiments are performed using the clinical handheld optoacoustic scanner as shown in the Figure 4.1a.

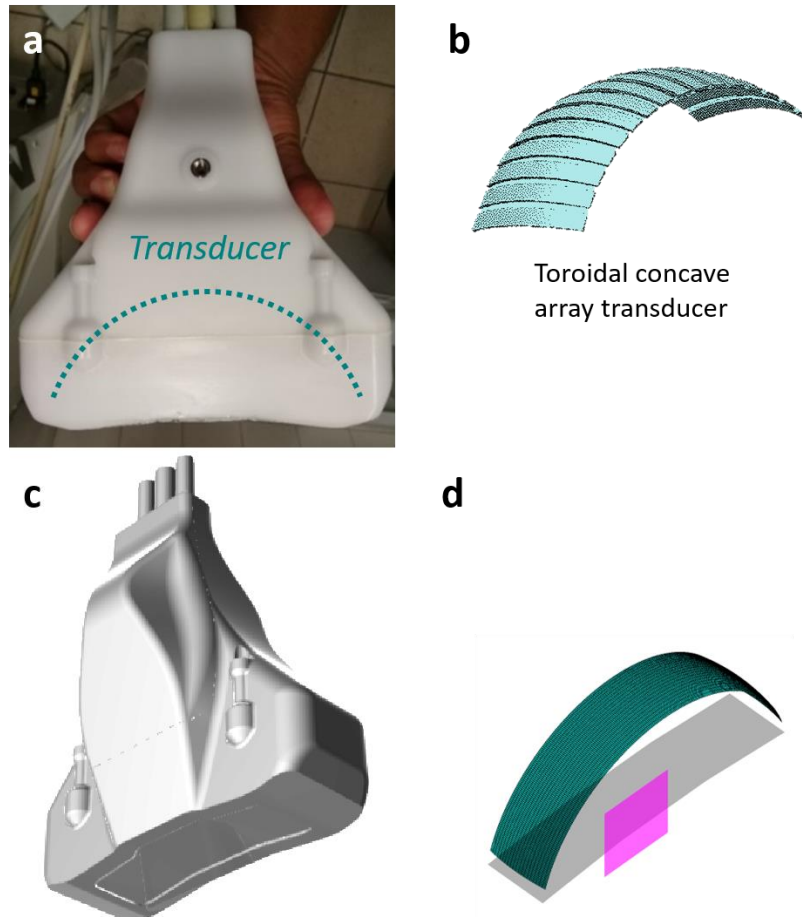


Figure 4.1: Modelling of the handheld scanner. (a) A photograph of the handheld optoacoustic scanner (b) Schematic of arrangement of elements in the transducer array (c) 3D model of the handheld scanner (d) Geometric model of the components of handheld probe. (Source: Panels (a) and (d) are self-designed; (b)-(c) are adapted from documents provided by iThera Medical)

4.2. Acoustic refraction

The acoustic refraction at the membrane interface between coupling medium and tissue is modelled as shown in the schematic in Figure 4.2. An acoustic response commencing from inside the tissue, propagates with acoustic speed c_t and gets refracted at the membrane interface and propagates with acoustic speed c_c in coupling medium, until being intercepted by the

transducer element at r_e . Fermat's principle was utilized to calculate the time-of-flight of the refracted ray as depicted by the blue solid line in Figure 4.2.

The point of incidence r_m on the membrane was determined, for each given pair of points (r', r_e) , by minimizing the total time-of-flight along the refracted ray $(r' - r_m - r_e)$ as

$$r_{c_c, c_t}^m(r_e, r') = \arg \min_{r_m \in \mu} \frac{(r_e - r_m)}{c_c} + \frac{(r_m - r')}{c_t}, \quad (4.1)$$

where $r_{c_c, c_t}^m(r_e, r')$ reveals the dependencies of r_m on the acoustic speed mismatch. μ denotes the set of all points on the membrane interface. The optimal time-of-flight for the refracted ray can be expressed as

$$t_{c_c, c_t}(r_e, r') = \frac{|r_e - r_{c_c, c_t}^m(r_e, r')|}{c_c} + \frac{|r_{c_c, c_t}^m(r_e, r') - r'|}{c_t}. \quad (4.2)$$

The equation (4.1) was solved with an algorithm based on golden section search and parabolic interpolation [150], [151], which enabled us to find the minimizer of the single variable function within a specified bound. The optoacoustic response generated in tissue by a uniform absorbing sphere at r' that is detected by an ideal point-like transducer with infinite detection bandwidth located at r_e in the coupling medium is given by

$$s_{r_e, r'}(t) = f_{r'} \cdot p_{c_c}^N(t - t_{c_c, c_t}(r_e, r')). \quad (4.3)$$

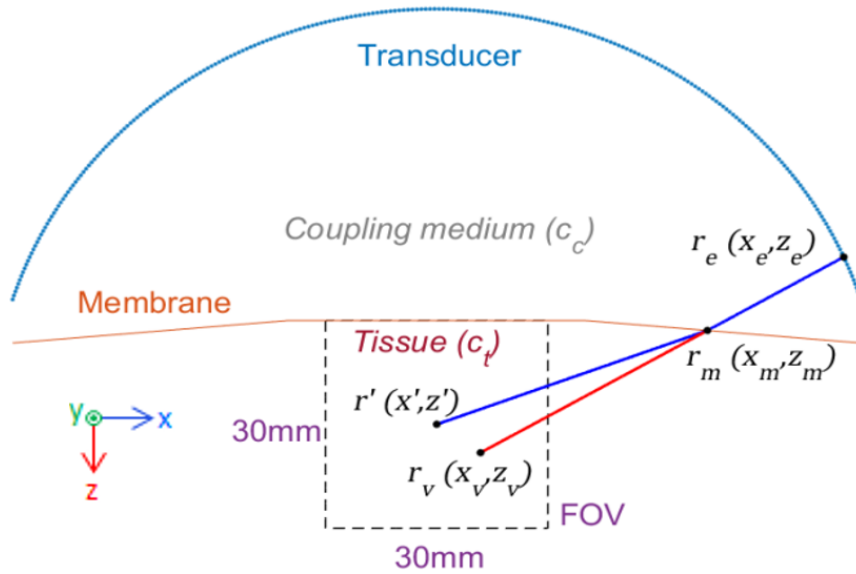


Figure 4.2: Schematic of limited view transducer using refraction model. Illustration of refraction of pressure wave originating from a source point r' inside the FOV, incident at membrane location r_m

and propagating towards the transducer element r_e in the limited view transducer array, assuming homogenous propagation medium with constant acoustic speed c_0 . (Source: Adapted from [144], Copyright © 2020 IEEE)

Since, the transducer used in this study is responsive only in a very short range (2-7MHz) of ultrasound frequency, the acoustic dispersion [152], [153] phenomenon being weak can be neglected in this case. Hence, it can be assumed that the wave shape does not change due to refraction across the membrane.

4.3. Dependence of SIR on refraction

Here the effect of refraction on the sensitivity field of the transducer is investigated. To do so the SIR in conjunction with the concept of virtual source is derived. Figure 4.2 illustrates that after an optoacoustic response originating from a source r' within the sample is refracted, the signal propagates towards the detector r_e along a different direction. After the refraction event, it propagates along the direction $(r_e - r_m)/|r_e - r_m|$ from r_m towards r_e . The variation of the point r_m with respect to the interception point on the transducer surface can be neglected because the distance between membrane and detector is significantly greater than the width of the transducer element. Subsequently, the wave is captured by the transducer element at r_e as if it originated from a virtual source located at a point r_v in the direction of r_m at a distance corresponding to the time of flight and travelled at the coupling speed of sound c_c along a straight line without being refracted. Accordingly, the location of the virtual point source can be derived as

$$r_{c_c, c_t}^v(r_e, r') = r_e - c_c \cdot t_{c_c, c_t}(r_e, r') \cdot \frac{r_e - r_m}{|r_e - r_m|}. \quad (4.4)$$

For ease of readability we abbreviate $r_v = r_{c_c, c_t}^v(r_e, r')$ to denote the virtual point. It is to be noted that $r_v = r'$ when $c_c = c_t$. An important observation was that, using virtual source in (3.5) the SIR (h_{c_c, r_e, r_v}^{SIR}) for an impulse starting at the virtual point r_v and travelling along a straight line with a constant acoustic speed c_c is identical to the SIR ($h_{c_c, c_t, r_e, r'}^{SIR}$) for an impulse starting at r' and travelling to the element r_e along the refracted path at the two different acoustic speeds c_c and c_t . The optoacoustic signal generated in the tissue by a uniform absorbing sphere

at r' , detected by an element located at r_e , with finite active surface area S_e and infinite bandwidth, can be written as

$$s_{r_e, r'}(t) = f_{r'} \cdot h_{c_c, c_t, r_e, r'}^{SIR} * p_{c_c}^N(t - t_{c_c, c_t}(r_e, r')), \quad (4.5)$$

where, the refraction-based SIR is given by

$$h_{c_c, c_t, r_e, r'}^{SIR}(t - t_{c_c, c_t}(r_e, r')) = \int_{S_e} \frac{\delta\left(t - \frac{|s - r_v|}{c_c}\right)}{|s - r_v|} dS(s). \quad (4.6)$$

The dependence of SIR on refraction was clearly observed by comparing (3.5) and (4.6).

4.4. TIR model based on refraction at membrane interface

To obtain the TIR model based on refraction at membrane surface, the EIR $h_{r_e}^{EIR}$ was added to (4.5). Then the measured signal as illustrated in Figure 4.3, can be decomposed into TIR components as:

$$s_{r_e, r'}(t) = f_{r'} \cdot h_{r_e}^{EIR} * h_{c_c, c_t, r_e, r'}^{SIR} * p_{c_c}^N(t - t_{c_c, c_t}(r_e, r')). \quad (4.7)$$



Figure 4.3: Schematic of signal decomposition. Decomposition of measured electrical into three components – Ideal “N”-shaped OA signal, Simulated SIR and approximate EIR. (Source: Adapted from [144], Copyright © 2020 IEEE)

It is to be noted that for $c_0=c_c=c_t$ (4.7) simplifies to constant acoustic speed case (3.6). The continuous time signals in (4.7) are sampled at the discrete $t = n \cdot \Delta t$, where $n=0,1,\dots,(T-1)$ and Δt is the sampling interval. Denoting the time-of-flight along the refracted path by n_R , the sampled signal can be written as

$$s_{r_e}[n] = \sum_{r' \in FOV} f_{r'} \cdot m_{r_e, r'}[n - n_R], \quad (4.8)$$

where,
$$m_{r_e, r'}[n] = h_{r_e}^{EIR} * h_{c_c, c_t, r_e, r'}^{SIR} * p_{c_c}^N[n]. \quad (4.9)$$

is the normalized response of a pixel at $r' \in \text{FOV}$. Equations (3.1), (4.1), (4.2), (4.4), (4.8) - (4.9) comprise the complete model for the acoustic data acquisition for refraction at an interface.

4.5. Synthetic TIR (sTIR)

The general TIR model for a handheld scanner was formulated in the last section. This section describes the simulation of SIR and experimental derivation the EIR to characterize the TIR of the clinical handheld tomographic system in the whole image plane. This TIR is termed as synthetic TIR (sTIR) since it was synthesized from experimental measurements and theoretical model. The synthesis of TIR was performed in four steps: (i) recording TIR at a location close to the center of FOV, (ii) simulation of the SIR based on refraction, (iii) approximate derivation of EIR by combining the TIR measurements and SIR simulation, (iv) construction of sTIR in the whole FOV by merging the numerically simulated SIR with the experimentally derived approximate EIR. It is to be noted that the approximate EIR used to generate sTIR is the representative mean EIR of the transducer elements in the array.

4.5.1. Measurement of TIR at center of FOV

A point source must be used to characterize the TIR and therefore a physical absorber of sub resolution dimension must be used as a target. Based on the center frequency [88] of the transducer used in this work the target should be much less than 200 μm in diameter to be qualified as point source. Again, too small a target of diameter $\sim 20 \mu\text{m}$ led to excessively less sensitivity. Therefore, a tradeoff was made and a single polyethylene microsphere of diameter 100 μm was placed roughly at the center of the FOV of the handheld scanner immersed in water bath as shown in the Figure 4.4. It is to be noted that the measured optoacoustic signals from all the elements of the transducer array contain the TIR of that location in the FOV.

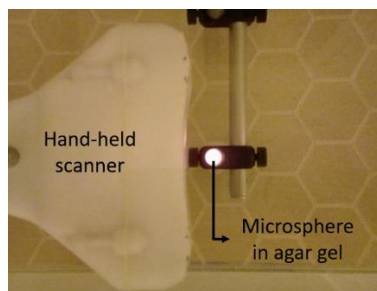


Figure 4.4: Photograph of signal measurement. Top view of the handheld probe setup showing scan of the microsphere phantom in the FOV of the handheld scanner.

4.5.2. Simulation of refraction-based SIR

The concept of virtual point was introduced to tackle the dependence of the SIR on refraction. As mentioned before the transducer used had a narrowband frequency response and for practical purpose it can be assumed that the shape of the optoacoustic wave was unaltered after refraction at the interface of coupling medium and sample. Hence, the SIR depends on the position of the virtual point relative to the transducer element considering constant acoustic speed of coupling medium. Based on this virtual point representation of optoacoustic source, we used the Field II program [115] which is efficient [154] for SIR computation with constant acoustic speed. The refraction based SIR in (4.8) was simulated by passing the co-ordinates of the virtual points as the field location and setting sound propagation speed to 1397 m/s [155], which is the acoustic speed in the heavy water (coupling medium of the handheld scanner) at room temperature. A square sub-aperture of dimension 50x50 μm , was used as unit of discretization of the active surface of the ultrasound transducer in Field-II. The dimension of the unit sub-aperture was chosen based on the scanning geometry [115], transducer size and center frequency. The sensitivity field of the handheld probe in the imaging plane was visualized by plotting the square root of energy of the SIR at each pixel. Figure 4.5c shows the sensitivity field (or SIR map) of the handheld scanner in the azimuthal plane (or image plane) considering refraction of sound waves at the membrane interface with acoustic speed in coupling medium as $c_c = 1397$ m/s and average tissue [156] acoustic speed as $c_t = 1540$ m/s. Similarly the sensitivity field of the handheld probe considering constant acoustic speed $c_0 = 1470$ m/s is shown in Figure 4.5d. Comparing the panels c and d of Figure 4.5 it is observed that refraction due to acoustic speed mismatch can severely distort the sensitivity field of the handheld scanners. This distortion has been highlighted using axial (red) and lateral (blue) line profiles across the highest sensitivity region of the SIR maps. The plots showing the comparison of the refraction-based SIR map (solid line) and the SIR map based on constant acoustic speed (dashed line) are provided in Figure 4.5e-f. It can be observed that due to refraction the sensitivity field has reduced and spatially shifted in the axial direction and spread across the lateral direction. It was demonstrated that modelling the effect of refraction on the SIR in case of handheld scanner is particularly important when it contains a coupling medium with significantly different acoustic property than the biological sample to be imaged.

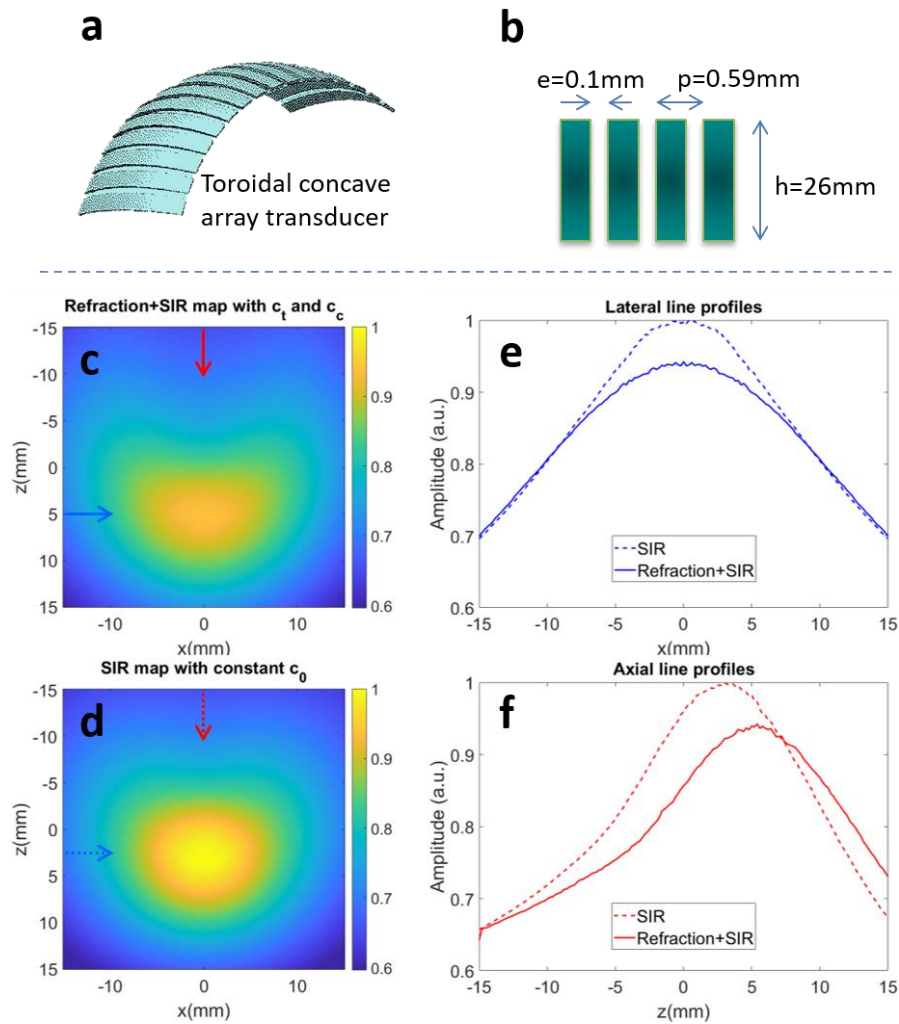


Figure 4.5: Simulation of refraction-based SIR. (a) Schematic of toroidal shaped transducer array (b) Dimensions and spacing between array elements (c) Azimuthal SIR map with refraction model (d) Azimuthal SIR map with constant acoustic speed model (e) Axial line profiles comparing SIR with constant acoustic speed model (dashed line) and SIR with refraction model (solid line). (f) Lateral line profiles comparing SIR with constant acoustic speed model (dashed line) and SIR with refraction model (solid line). (Source: Panels (c)-(f) are adapted from [144], Copyright © 2020 IEEE)

4.5.3. Derivation of approximate EIR

The EIR of the handheld optoacoustic probe can be derived using the measured signals containing the TIR and the simulated refraction-based SIR. It is to be noted that there are other factors of the imaging system which has not been accounted for in this work for example fluence effects, illumination source profile, Grüneisen parameter, etc. This combination of these parasitic parameters may affect the derived EIR. Therefore, the extracted EIR has been referred to as approximate EIR (or aEIR).

As stated earlier, that SIR is dependent on the location of the source relative to the transducer element and hence care must be taken during the extraction of aEIR from the measured TIR which also contains SIR. To ensure least contamination of SIR, the TIR measurements has been done at points located in the center of the FOV. This ensures that the modelled SIR is close to delta impulse and the obtained aEIR is independent of the FOV. The aEIR derivation method was developed to obey the fact that SIR effects are least close to the focus [106], [143], [146].

A normalized 'N'-shaped optoacoustic response from a homogenous solid sphere of diameter $D = 100 \mu\text{m}$ was modeled in (4.8) - (4.9) in accordance with the TIR measurements of the response of a solid polyethylene microsphere of diameter $100 \mu\text{m}$. The measure signal at each element e can be written as

$$s_{r_e, r'}[n] = f_{r'} \cdot h_{r_e}^{aEIR} * m_{r_e, r'}^R[n - n_R], \quad (4.10)$$

where,
$$m_{r_e, r'}^R[n] = h_{c_c, c_t, r_e, r'}^{SIR} * p_{c_c}^N[n], \quad (4.11)$$

can be treated as the response from the microsphere including SIR. It is to be noted that the aEIR can be derived from (4.10) - (4.11) by deconvolving the simulated component $m_{r_e, r'}^R$ out of the measured signal $s_{r_e, r'}$. This deconvolution was performed using Wiener filter and an estimate of the Gaussian noise with 0.1 as NSR (noise to signal power ratio) in Matlab. Under the assumption that all the transducer elements were identical, the aEIR of the whole transducer array was estimated by the arithmetic mean over all the elements as

$$h^{aEIR}[n] = \frac{1}{N_e} \sum_{e=1}^{N_e} h_{r_e}^{EIR}[n] \quad (4.12)$$

The derived aEIR is shown in the panels b-c of Figure 4.6 in time and frequency domain representations respectively. This aEIR is derived based on single point measurement at the center of the FOV. The solid line refers to the mean aEIR and the shaded bounds indicates the standard deviation at each time/frequency point.

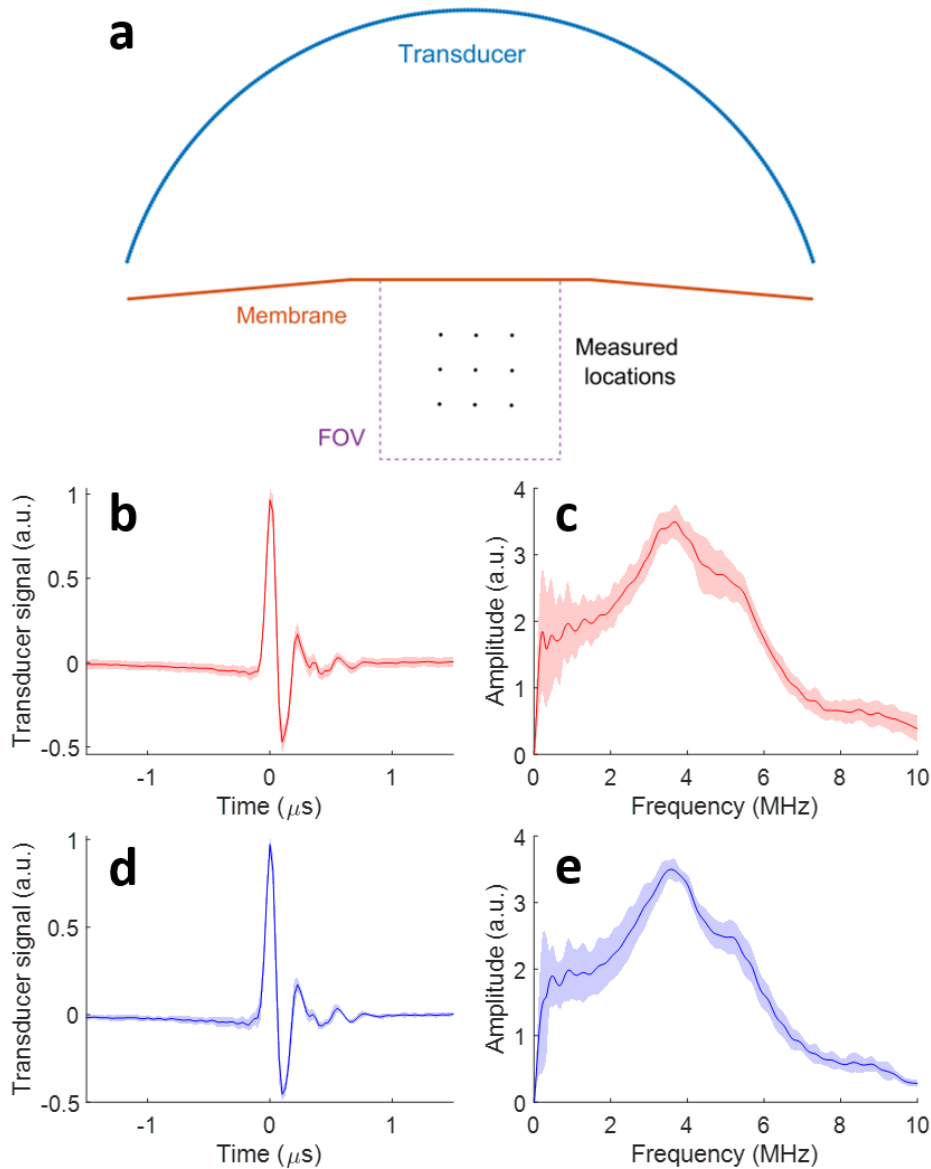


Figure 4.6: Experimentally derived aEIR and validation of simulated SIR. (a) Locations in FOV relative to the membrane interface where measurements were performed to validate the accuracy of simulated SIR. (b)-(c) Derived aEIR of all transducer elements measured at single location at the center of the FOV in time and frequency domains, respectively. (d)-(e) aEIR across different locations of FOV marked in panel (a) in time and frequency domains, respectively. Solid line indicates mean value and shaded boundary indicates standard deviation. (Source: Figure is adapted from [144], Copyright © 2020 IEEE)

4.5.4. Validation of the simulated SIR

Since simulated SIR was used to derive the aEIR, a question regarding the validation of the simulated SIR was inevitably raised. Hence, to address this and verify the accuracy of the simulated SIR, assessing the consistency of aEIR measured at different locations of FOV was needed. Since, the exact EIR depends solely on the electro-acoustic properties of the transducer element, and not on the relative location of the source, the derived aEIR was expected to be independent of the co-ordinates of the FOV. Subsequently additional measurements were performed in different locations spread across the whole FOV as shown in Figure 4.6a. h_{aEIR} for 9 different locations in the FOV were computed and it was found that they were consistent as shown in Figure 4.6d-e, where solid line indicates the mean and shading indicates the standard deviation. The Coefficient of Variation (CV) among the different aEIR responses was less than 0.05 indicating low variance and eventually enabled reliable use of this aEIR over the entire FOV and proving that the simulated SIR matches closely with experimental situation.

4.5.5. Synthesis of sTIR

Having all the components of the sTIR simulated or derived, the forward model can eventually be constructed. The derived aEIR from (4.12) and the simulated SIR from (4.6) can be incorporated into discretized pixel response of entire FOV of (4.10) to obtain the sTIR forward model, which is expressed as

$$s_{r_e}[n] = \sum_{r' \in FOV} f_{r'} \cdot h^{aEIR} * h_{c_c, c_t, r_e, r'}^{SIR} * p_{c_c}^N[n - n_R] \quad (4.13)$$

It is to be noted that (4.13) is to be treated as a comprehensive sTIR forward model consisting of all the components – refraction, SIR and aEIR, which are taken into account in this work.

4.5.6. sTIR forward models

The Table 1 shows the six different forward models used to sequentially study the effect of the sTIR components – refraction, SIR and aEIR from generation of acoustic waves to the formation of electrical signals.

Table 1: Forward models with SIR and TIR corrections based on constant acoustic speed and refraction. The table entries indicate the structure of the corresponding matrix elements.

M $\{m_{r_e, r'}[n]\}$	M_x $h^{SIR} = \delta; h^{aEIR} = \delta$	M_x^{SIR} (SIR correction) $h^{aEIR} = \delta$	M_x^{sTIR} (TIR correction)
M_0^x $c_c = c_t = c_0$	$p_{c_0}^N[n - n_0]$	$h_{c_0, r_e, r'}^{SIR} * p_{c_0}^N[n - n_0]$	$h_{r_e}^{aEIR} * h_{c_0, r_e, r'}^{SIR} * p_{c_0}^N[n - n_0]$
M_R^x $c_c \neq c_t$	$p_{c_c}^N[n - n_R]$	$h_{c_c, c_t, r_e, r'}^{SIR} * p_{c_c}^N[n - n_R]$	$h_{r_e}^{aEIR} * h_{c_c, c_t, r_e, r'}^{SIR} * p_{c_c}^N[n - n_R]$

The first row of Table 1 named M_0^x , shows the matrix elements of three different forward models based on constant acoustic speed c_c using (3.1) - (3.11): M_0 assumes ideal point transducer with infinite bandwidth, M_0^{SIR} assumes simulated SIR with infinite bandwidth and M_0^{sTIR} assumes simulated SIR with measured aEIR. In parallel the second row of Table 1 named M_R^x , shows the matrix elements of three different forward models based on refraction due to acoustic speed mismatch $c_c \neq c_t$ using (3.1), (4.1) - (4.9): M_R assumes ideal point transducer with infinite bandwidth, M_R^{SIR} assumes simulated SIR with infinite bandwidth and M_R^{sTIR} assumes simulated SIR with measured aEIR. M_R^{sTIR} indicates the complete model consisting of the proposed sTIR model. The constant acoustic speed-based models were included in this study to compare the proposed refraction models against the existing forward models. It can be observed that using $c_0 = c_c = c_t$ in (3.1), (4.1) - (4.9), the refraction-based models takes the form of constant acoustic speed models.

It is to be noted that the computation of the forward model for certain FOV and acoustic speed requires solving (4.1) and (4.6) $P^2 \times N$ times i.e., for each pair of transducer element and image pixel and this is one-time effort. The time required to compute model matrices M_R and M_R^{SIR} or M_R^{sTIR} for 151 x 301 pixels for a given 256-element array transducer are approximately 1hr and 3hrs, respectively. The computed model matrix once built can be stored for reconstruction of acquired datasets of size 2030 x 256 where 2030 is the length of samples acquired by each transducer. The time required to reconstruct each frame using the LSQR type method was 40 seconds. The computation times reported in this chapter are based on a computer with Intel® Core™ i7-6700K CPU @ 4.00 GHz.

4.6. Image correction using sTIR

The sTIR forward models generated in the last section were used to reconstruct the images to demonstrate the correction for TIR related effects on images. To begin with, a vivid description of the optoacoustic imaging platform has been presented to set the stage for understanding the scope of experiments. Subsequently, the design of the numerical and physical phantoms is reported based on which experimental results were derived. Finally, the clinical scans on human volunteers are detailed.

4.6.1. Description of the optoacoustic imaging platform

The handheld scanner version [31], [60] of the Multispectral Optoacoustic Tomography (MSOT) system was used to demonstrate the methods proposed [144] in this thesis. The photograph of the MSOT system is shown in Figure 4.7. As an optical excitation source, the system uses a pulsed laser (Spitlight 600 DPSS, Innolas Laser, Germany) tunable in the wavelength range of 700-980nm with a pulse length of approximately 8 ns. The pulsed laser is capable of operating at 25Hz to tune across 28 wavelengths in the range 700-980nm at steps of 10nm. This enables multi-spectral excitation of the sample. The optical illumination was coupled from the laser source to the handheld probe via a custom-made fiber bundle (CeramOptec, Germany). At the output (inside the handheld probe) the optical fiber endings were aligned along a rectangular slit of dimensions 40 x 1 mm². A diffuser was placed after the optical fiber ending to obtain a homogenous illumination on the surface of the sample. For detection of optoacoustic waves, a toroidal array of piezocomposite transducers was used from Imasonic, France. The transducer array had 256 elements arranged along azimuthal arc covering an angle of 145°. The radius of the transducer array was 60 mm in azimuthal plane. Each transducer element was cylindrically focused in the azimuthal plane or image plane (xz-plane) with a radius of curvature of 65mm in elevation plane. The chord height (in elevation) of a transducer element was 26 mm. Each transducer element was 0.49 mm thick and placed 0.59 mm away. Hence, the kerf (inter-elements spacing) was 0.1mm. The center frequency of the transducer was 4 MHz with a -6dB bandwidth of about 50% in the transmit/receive mode as characterized by the manufacturer. The sample facing side of the handheld scanning probe was sealed with optically transparent low-density polyethylene membrane for suitable handheld operation, and the cavity between the membrane and the concave transducer was filled with heavy water (D₂O) for acoustic coupling. The membrane was around 100 µm thick and was treated acoustically transparent for practical purpose of longitudinal travelling waves. The pre-amplified analog signals from the transducer were digitized at a sampling rate of 40MS/s with

an amplitude resolution of 12 bits using a custom built 256-channel analog-to-digital converter. The pulsed laser is synchronized to trigger the data acquisition (DAQ) with every laser pulse in a single-frame-per-pulse fashion.

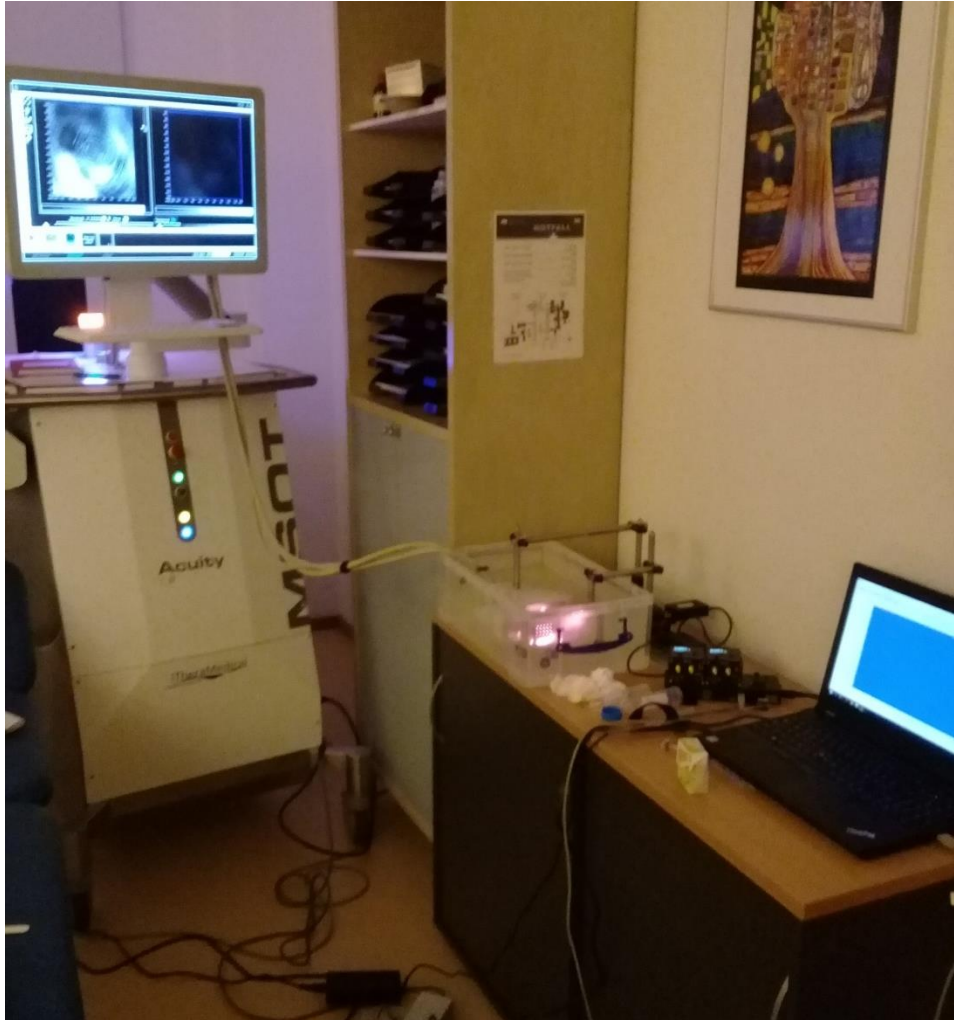


Figure 4.7: The handheld optoacoustic imaging system. Photograph showing the MSOT Acuity optoacoustic platform from iThera Medical GmbH and the handheld probe being characterized in water bath, using external motorized linear translation stages.

4.6.2. Image correction framework

The recorded signals were first preprocessed with a Butterworth bandpass filter in the frequency range of 100 kHz to 12 MHz to eliminate noise beyond the sensitivity range of the transducer in use. As it has been described earlier that EIR is independent of relative locations of the source and therefore the aEIR could be deconvolved from the preprocessed signals. The general forward model is written as

$$s' = \mathbf{M}f, \quad (4.14)$$

where s' is the column vector of the pre-processed signals. The six different forward models stated in Table 1 were used to demonstrate the SIR and sTIR correction in constant acoustic speed models and refraction models step-by-step. Hence, the forward model matrices were denoted by $\mathbf{M} \in \{M_R, M_R^{SIR}, M_R^{sTIR}, M_0, M_0^{SIR}, M_0^{sTIR}\}$. The equation (4.14) was inverted to find the optoacoustic image f by solving the regularized least squares problem

$$f_{sol} = \arg \min_f \|\mathbf{M}f - s'\|_2^2 + \lambda \|Lf\|_2^2, \quad (4.15)$$

where L denotes the identity matrix for standard Tikhonov regularization and λ denotes the regularization parameter. The LSQR type method was used to choose the regularization parameter [104], [157] which was based on simplex method. It is to be noted that addition of the SIR and aEIR reduces the sparsity and increasing the size of the model matrix. Therefore L-curve or GCV based automatic choice of regularization parameter cannot be used due to huge computational burden. The regularization parameter was chosen in a semi-automatic fashion such that no bias was introduced during comparison of reconstruction results using different forward models. Illustration of semi-automatic choice of regularization parameter is provided in Chapter 0.

4.6.3. Numerical phantoms

The proposed sTIR forward models were tested first using a numerical dot grid phantom as shown in Figure 4.9a. Further reconstruction results were generated using USAF target shown in Figure 4.10a. A fine resolution of 100 μm over the 30 mm FOV was used to discretize the ground truth of the numerical phantoms and optoacoustic signals were obtained using the sTIR model matrix M_R^{sTIR} and different levels of noise were added to obtain noisy signals with SNR in the range of 40dB to 5dB as shown in Figure 4.11. The reconstructions using numerical phantoms were performed on a coarse grid close to system resolution of 200 μm over the 30 mm FOV. Hence, inverse crime was avoided. The metric SSIM (Structural Similarity Index) [158], is based on visual perception of shapes and structures and was found to be best suited in this work to evaluate the performance of the method in those experiments where ground truths were available. The ground truths were in the range of [0, 1]. Therefore, the reconstructed images were first normalized by their maximum values and negative values were discarded as they do not represent meaningful optoacoustic contrast. Thereafter, SSIM of these normalized images were computed with respect to the ground truth and the reported SSIM values lie in the

reasonable range [0, 1]. Non-noisy signals were used to reconstruct the images shown in the Figure 4.9 while noisy signals with SNR of 20dB was used to produce the reconstructed images shown in Figure 4.10.

4.6.4. Experimental measurements

To validate the performance of the proposed sTIR method experiments using physical phantoms were necessary. Therefore, two types of phantoms were imaged using the handheld probe immersed in water. The first phantom was constructed by embedding a single polyethylene microsphere of diameter 100 μm in agar gel cylinder. It was used to characterize the EIR of the system and also experimentally measure the resolution of the system as shown in the Figure 4.8. The second physical phantom is shown in Figure 4.12, which was constructed by embedding a printed sheet of white paper in agar gel block. A dot grid pattern resembling the first numerical phantom was printed with black ink on the sheet of white paper. The diameter of these dots was approximately 200 μm and they were printed 4 mm apart. A 1.5% (w/v) agar gel solution was used to prepare all the phantoms. The experimental recordings of these phantoms were based on 700 nm illumination wavelength.

As an obvious next step, clinical scans were performed to demonstrate the image quality improvement using sTIR. Two handheld clinical scans were done non-invasively on the arms of healthy volunteers. A thin layer of ultrasound gel was applied on the skin surface to couple acoustic waves from tissue into the probe. Prior to the clinical scans, informed consent was received from the volunteers.

4.7. Results

This section reports the results of the experiments performed using the handheld scanner using the sTIR forward models. First, the improvement in system resolution using the proposed sTIR model was investigated. Thereafter the numerical simulations were performed to investigate the effects of the components of the sTIR model. Subsequently, the performance of the proposed method was validated using physical agar phantom with printed dot grid pattern. In order to study each correction step of sTIR forward model all the above-mentioned reconstructions were performed using all the six different models listed in Table 1. Finally, the performance of the sTIR model was evaluated on clinical scans obtained from healthy human volunteers.

4.7.1. Characterization of system resolution

The system resolution was characterized as a first step of experiments to understand how each aspect of transducer property affect the system resolution. To characterize the system resolution

a microsphere of sub-resolution diameter was used as a sample phantom. This phantom was scanned in two different regions – ROI_A and ROI_B of the FOV of the handheld scanner as shown in Figure 4.8a. It is to be noted that ROI_A was chosen close to the membrane of the scanner to access the effects of the interface of membrane and sample. The second ROI_B was chosen close to the center of the FOV to understand the effects deep inside the sample. Figure 4.8b shows the top view of the setup where the microsphere is being scanned by the handheld probe submerged in water. The schematic of the microsphere phantom in Figure 4.8c illustrates a 100µm microsphere embedded inside the Agar gel cylinder. The standard M₀ model (without including transducer properties) based reconstruction of the microsphere phantom at ROI_A considering constant acoustic speed is shown in Figure 4.8d. Strong artefacts were observed which can be attributed to the mismatch of acoustic speed. The panels Figure 4.8e-f display reconstructions of the microsphere at ROI_A based on M₀^{SIR} and M₀^{sTIR} respectively. It can be easily observed that SIR and TIR corrections based on constant acoustic speed could not mitigate the artefacts. However, the M_R based reconstruction mitigates the artefacts significantly as displayed in the Figure 4.8g. The M_R^{SIR} and M_R^{sTIR} reconstruction as shown in the panels Figure 4.8h-ifurther improves the resolution. The bar graph in Figure 4.8j compares the lateral and axial full width at half-maximum (FWHM) for images at ROI_A. It was observed that although resolution increases with SIR and sTIR correction, the M_R could not significantly enhance resolution. The reconstructed images of the microsphere at ROI_B using all the six models are displayed in the Figure 4.8k-p. The M₀ reconstruction in panel Figure 4.8k shows artefacts due to local acoustic speed mismatch which could not be mitigated by M₀^{SIR} and M₀^{sTIR} reconstructions like the previously mentioned results for ROI_A. It was again observed that with refraction correction (Figure 4.8n) the artefacts were eliminated. SIR and sTIR corrections along with refraction correction shows significant improvement in resolution as shown in the panels Figure 4.8o-p. Finally, the comparison of lateral and axial FWHM for all the six models are drawn in the bar plot of Figure 4.8q. It is important to note that with subsequent correction of properties of transducers from M₀ to M_R^{sTIR} not only each lateral and axial resolution improved but also the difference between the lateral and axial resolution significantly reduced indicating the improvement in isotropic shape of the microsphere. Overall, an axial resolution of around 200 µm was achieved using M_R^{sTIR} reconstruction.

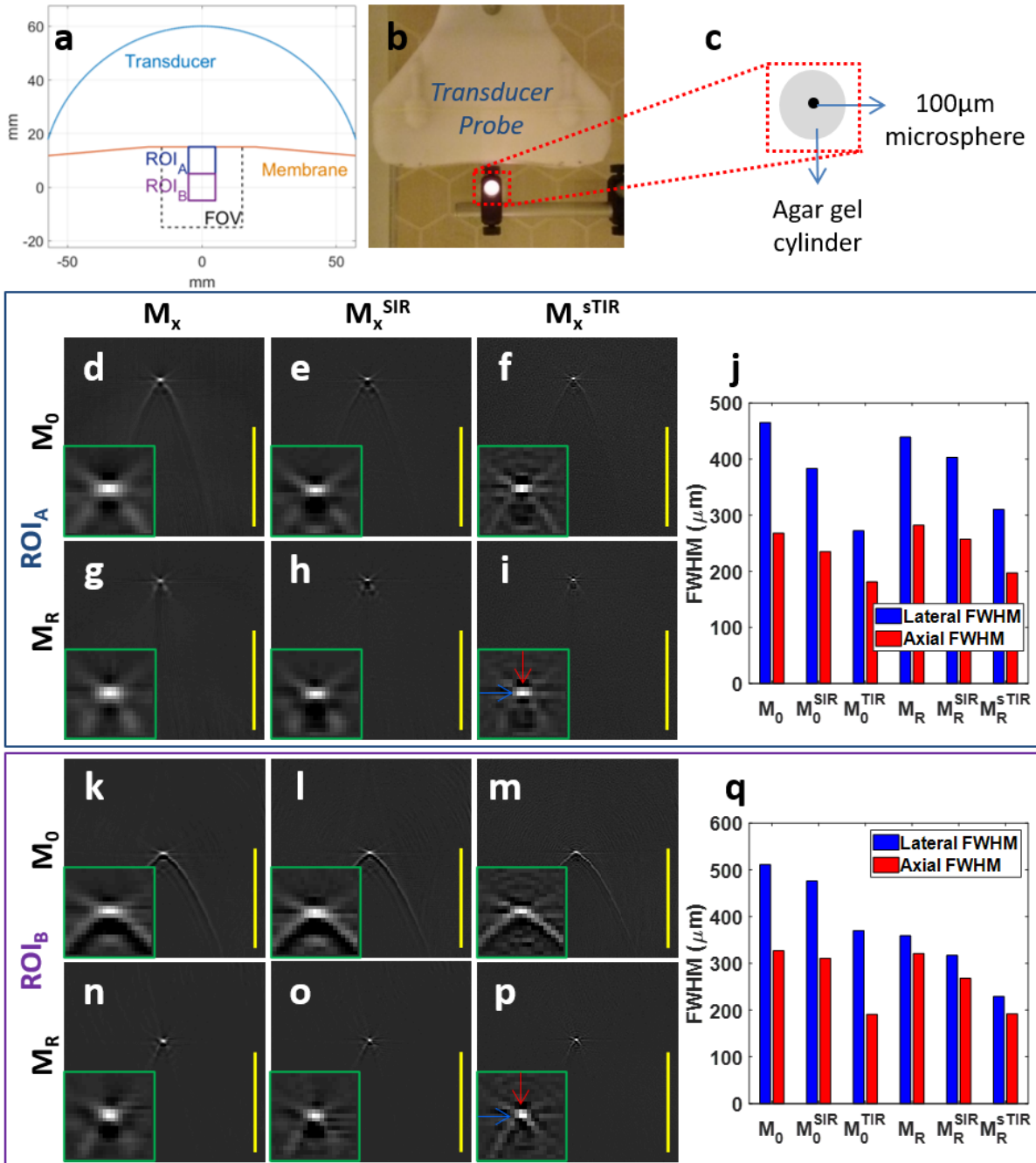


Figure 4.8: Improvement in system resolution using sTIR models. A microsphere with of sub-resolution dimension embedded in an agar cylinder was scanned in the FOV of the handheld scanner immersed in water bath using an excitation wavelength of 700 nm. **(a)** Schematic of the transducer array showing ROI_A and ROI_B, each measuring 10 x 10 mm, inside the FOV. **(b)** Photograph of the microsphere phantom being scanned with the handheld scanner. **(c)** Schematic of the single microsphere phantom. **(d-i)** Images of the microsphere located in ROI_A reconstructed using the M₀ forward model (upper row) or M_R forward model (lower row) in the absence of correction for transducer property (left column), with SIR correction (middle column) or sTIR correction (right column). The red and blue arrows indicate axial and lateral line profiles. A higher-magnification view of the microsphere is shown as an inset. **(j)** Comparison of lateral FWHM and axial FWHM in images at ROI_A. **(k-p)** Images of the

microsphere located in ROI_B reconstructed using the M_0 forward model (upper row) or M_R forward model (lower row) in the absence of correction for transducer property (left column), with SIR correction (middle column) or sTIR correction (right column). The red and blue arrows indicate axial and lateral line profiles. A higher-magnification view of the microsphere is shown as an inset. **(q)** Comparison of lateral FWHM and axial FWHM in images at ROI_B . Scale bar, 5 mm. (Source: Figure is adapted from [144], Copyright © 2020 IEEE)

4.7.2. Reconstruction using numerical phantoms

Reconstruction of numerical phantoms were performed to investigate the adverse effects of neglecting transducer properties in forward model. Results of reconstruction using two different numerical phantoms will be presented herein.

First the reconstruction results using the proposed sTIR forward models are reported on a numerical phantom of dot-grid pattern. Since a dot-grid pattern contains same unit absorber pixels throughout the FOV, it is expected to reveal the effects of transducer properties on the image in the spatial domain. The ground truth of the dot-grid numerical phantom is shown in Figure 4.9a and the schematic of the numerical phantom in the FOV of the transducer array is depicted in Figure 4.9b. Thereafter Figure 4.9c presents the M_0 (constant acoustic speed) reconstruction of the dot-grid pattern and a spatially non-uniform degradation of the image was observed. The intensity of the artefacts due to local mismatch in acoustic speed is the strongest at the top and bottom of the image and weakest at the middle. Subsequently this reveals the variation of relative mismatch in local acoustic speed throughout the FOV. Figure 4.9d-e displays that M_0^{SIR} and M_0^{sTIR} based reconstruction fails to mitigate the artefacts or bring all the locations of FOV “in focus”. Figure 4.9f displays the M_R based reconstruction where all the artefacts related to refraction effects are eliminated. Next the M_R^{SIR} correction displayed in panel Figure 4.9g shows mitigation of distortion effects caused by the transducer physical dimensions. Comparing the insets of panels Figure 4.9f-g one can notice the improvement of lateral symmetry after SIR correction. Finally, M_R^{sTIR} correction displayed in Figure 4.9h shows improved contrast and isotropic shape of the absorbers. Figure 4.9i-j compare the axial and lateral profiles across the absorber which is magnified in the insets. The M_R^{sTIR} reconstruction accurately localizes the absorbers in both the axial and lateral dimensions while the standard M_0 based reconstruction fails to do so. Finally, the structural similarity indices for the all the six reconstructed images were compared in Figure 4.9k. It is observed that refraction correction improves localization of the absorbers leading to general rise in similarity index and subsequent SIR and sTIR corrections further enhances the similarity index.

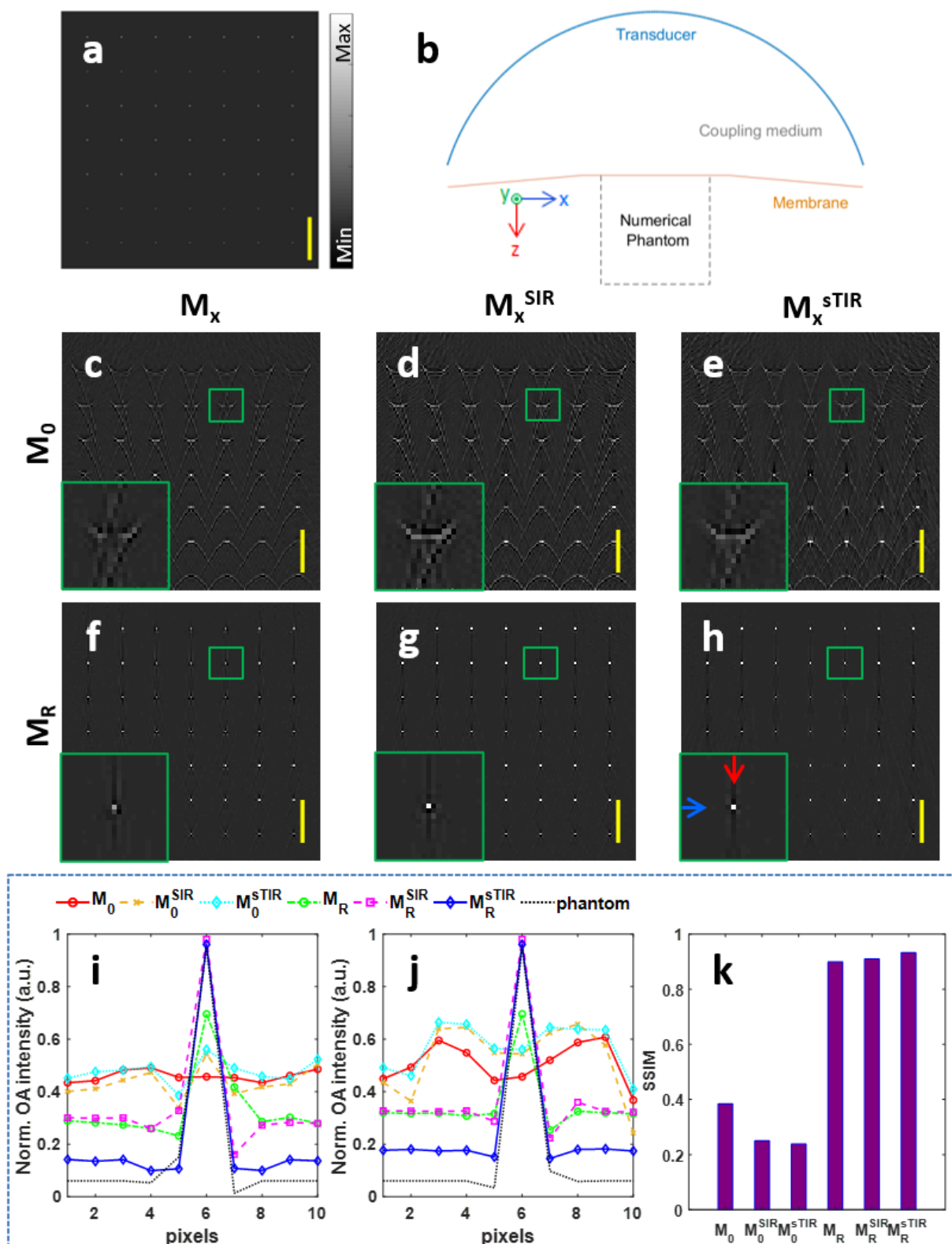


Figure 4.9: Reconstruction of numerical dot grid phantom to demonstrate the negative effects on image quality due to neglecting transducer properties. A numerical phantom of simulated dot grid pattern was simulated on the 30 x 30 mm FOV of a handheld probe, and noise-less signals were simulated using *sTIR* forward model. (a) Ground truth of the dot grid numerical phantom. (b) Schematic

of the numerical phantom in the FOV of the handheld probe. **(c-h)** Reconstructed images of the grid pattern using the M_0 forward model (*upper row*) or M_R forward model (*lower row*) without correction for transducer properties (*left column*), with SIR correction (*middle column*) or sTIR correction (*right column*). The axial and lateral line profiles are marked using red and blue arrows. Insets show zoomed in views of the reconstructed image boxed in green. **(i-j)** Plots of axial (*upper*) and lateral (*lower*) line profiles across images reconstructed using M_0 , M_0^{SIR} , M_0^{sTIR} , M_R , M_R^{SIR} , M_R^{sTIR} and phantom. **(k)** Structural similarity indices of reconstructions using all six models. Scale bar, 5 mm. (Source: Figure is adapted from [144], Copyright © 2020 IEEE)

After having the reconstruction results evaluated based on a simple dot-grid numerical phantom, a more complex numerical phantom based on USAF target was used to validate the negative effects of neglecting transducer properties in reconstruction. Figure 4.10a displays the ground truth of the numerically simulated USAF target. Figure 4.10b illustrates the schematic of the numerical phantom in the FOV of the handheld transducer. The forward model M_R^{sTIR} was used on the USAF pattern and noise was added to generate noisy signals with a signal-to-noise ratio (SNR) of 20 dB. Then the M_0 based reconstruction considering constant acoustic speed is displayed in Figure 4.10c. Artefacts from the acoustic speed mismatch caused severe degradation such that the numbers are not legible. Subsequent panels Figure 4.10d-e displays the reconstructed images of the USAF target based on M_0^{SIR} and M_0^{sTIR} . It can be easily noticed that correction for transducer properties could only enhance the contrast and yet fails to reduce the structural degradation. Figure 4.10f displays the M_R based reconstruction depicting significant structural improvement compared to the M_0 based reconstructions. Figure 4.10g-h shows the M_R^{SIR} and M_R^{sTIR} based reconstructions highlighting the significant improvement in contrast and partial improvement in structural quality. Figure 4.10i-j compare, respectively, the axial and lateral profiles through the horizontal and vertical set of lines in reconstructed images with all six models (Figure 4.10c-h), along with the ground truth phantom shown in Figure 4.10a. Reconstruction based on M_R^{sTIR} , but not M_0 , clearly resolves the set of vertical and horizontal lines. Consistent with this result, Figure 4.10k shows a much higher structural similarity index for M_R^{sTIR} reconstruction and gradual increase in the SSIM index with each step of correction. These results show that even in the presence of simulated noise, the refraction model-based reconstruction with SIR and sTIR correction improves structural quality.

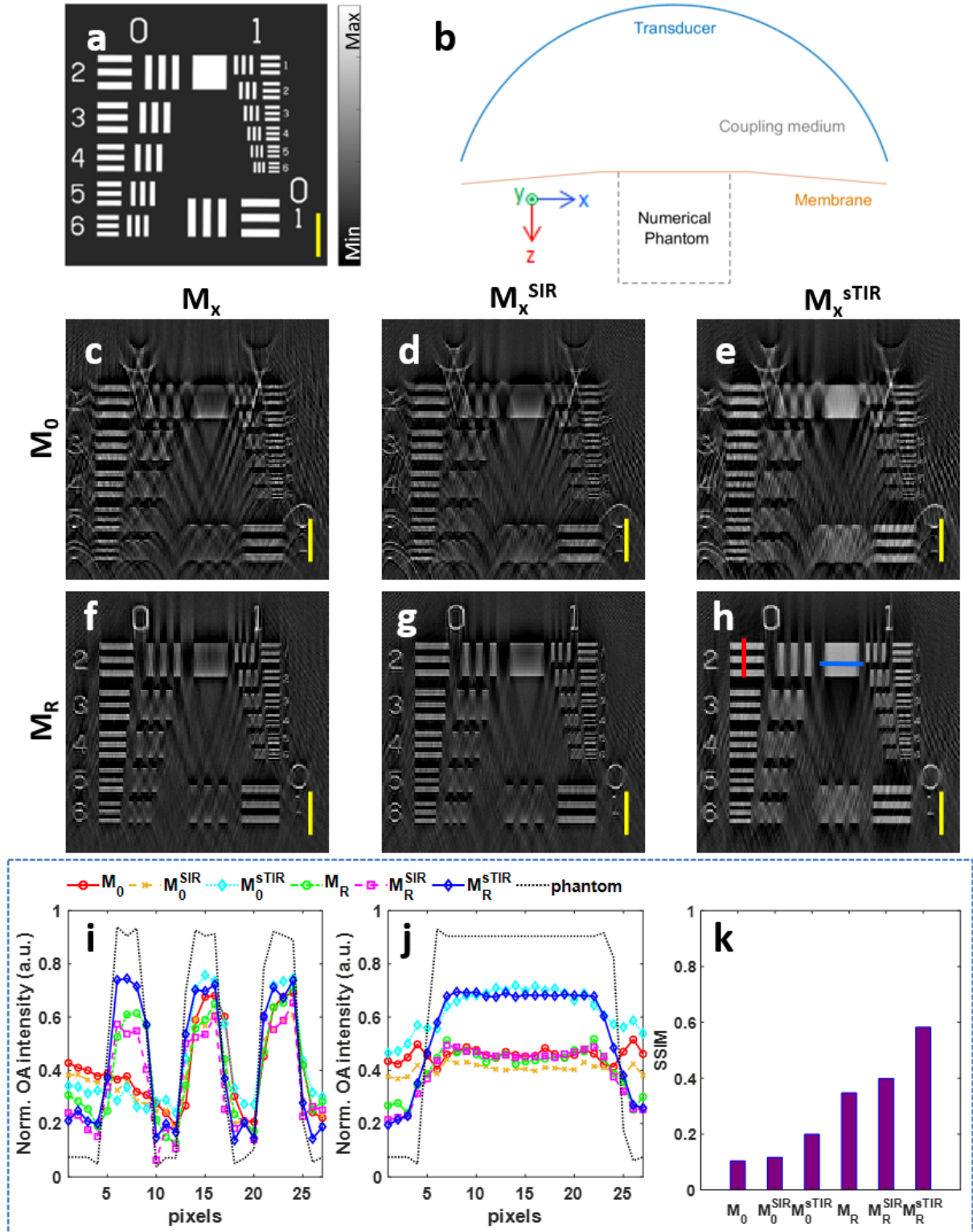


Figure 4.10: Reconstruction of numerical USAF target phantom to demonstrate the negative effects on image quality due to neglecting transducer properties. A numerical phantom of simulated USAF target on the 30 x 30 mm FOV of a handheld probe, and noisy signals were generated using sTIR forward model and added noise. (a) Ground truth of the USAF target phantom. (b) Schematic of the USAF target phantom in the FOV of the handheld probe. (c-h) Reconstructed images of the USAF target using the M_0 forward model (*upper row*) or M_R forward model (*lower row*) without correction for

transducer properties (*left column*), with SIR correction (*middle column*) or sTIR correction (*right column*). The axial and lateral line profiles are marked using red and blue lines. **(i-j)** Plots of axial (*upper*) and lateral (*lower*) line profiles across images reconstructed using M_0 , M_0^{SIR} , M_0^{sTIR} , M_R , M_R^{SIR} , M_R^{sTIR} and phantom. **(k)** Structural similarity indices of reconstructions using all six models. Scale bar, 5 mm. (Source: Figure is adapted from [144], Copyright © 2020 IEEE)

4.7.3. Evaluation of effect of noise on numerical simulation

So far reconstruction results on full FOV has been investigated with numerical phantoms and it was found M_R^{sTIR} (the complete sTIR) model is expected to offer the most improvement in terms of image quality both with non-noisy signals and signals with 20dB SNR. Before we move on to explore the proposed method with recorded data from the actual MSOT system, it is important to evaluate the effect of increasing noise on the reconstruction results. This is due to the fact that in practice the experimental recordings will have noise added from the detection instruments. Hence, the effect of increasing noise on the reconstruction results has been evaluated in terms of structural quality for both numerical phantoms – dot-grid and USAF. This has been accomplished by generating non-noisy signals using forward model M_R^{sTIR} on the high resolution (100 μm on 30mm FOV) ground truth and thereafter adding white Gaussian noise of varying level to achieve noisy signals with SNR in the range of 40dB to 5dB. Then, all the six forward models mentioned in Table 1 were used to reconstruct images on a lower resolution grid (200 μm on 30mm FOV) and SSIM for each image was calculated. Figure 4.11a-d shows the bar-graph plots of the SSIMs for dot-grid pattern. It is observed that the structural quality offered by M_R^{sTIR} continues to be highest until SNR of 10dB. Figure 4.11e-f shows the bar-graph plots of SSIMs for the more complex USAF pattern and interestingly it can be noticed that even though the overall structural quality drops with increasing noise levels, M_R^{sTIR} continues to offer the best structural quality.

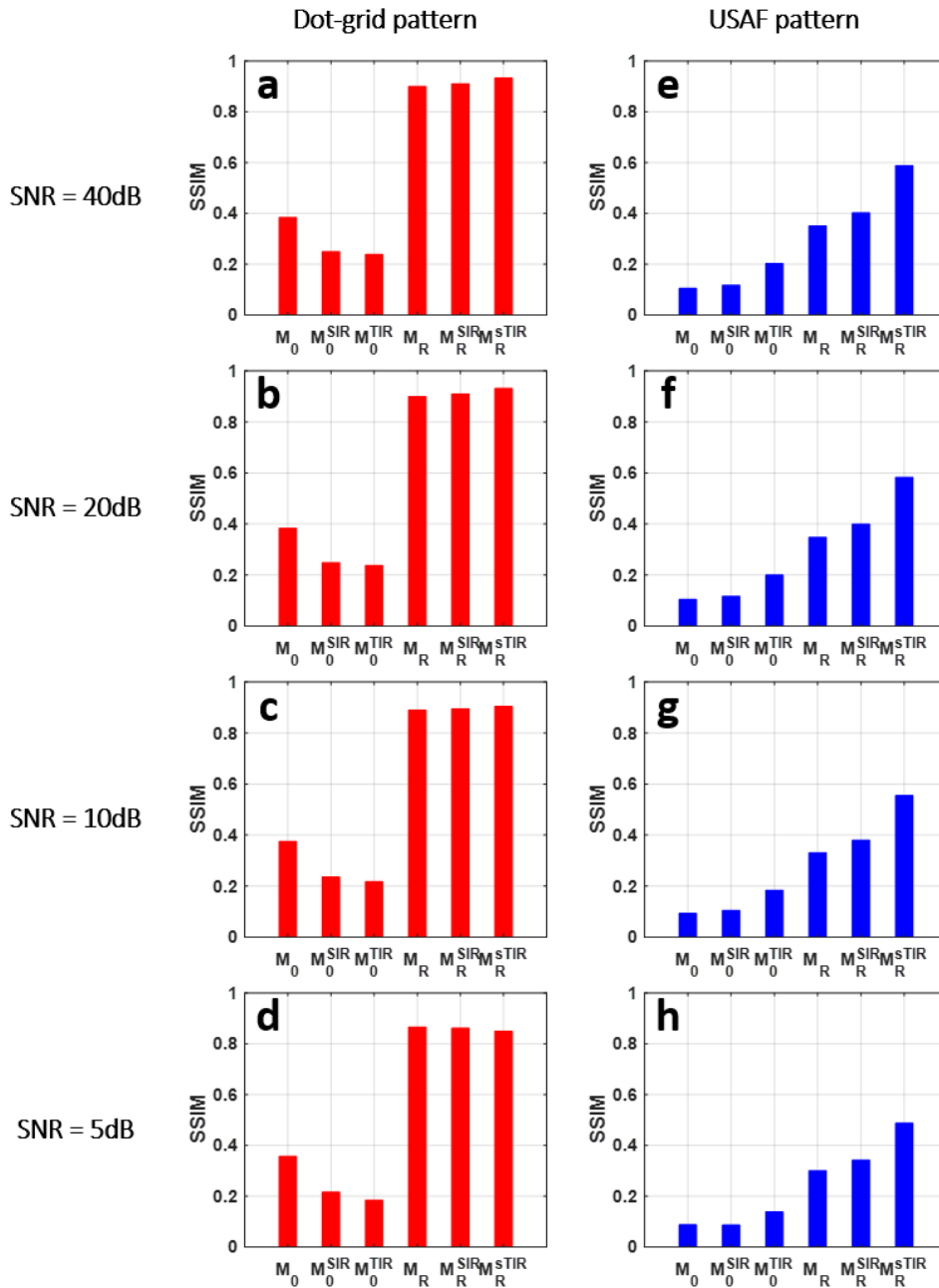


Figure 4.11: Evaluation of effect of increasing noise on the structural quality in reconstruction of numerical phantoms. Numerical phantoms were reconstructed using six each model from signals with SNR varying from 40dB to 4dB and SSIM was calculated. (a-d) SSIMs are based on reconstruction of dot-grid pattern. (e-h) SSIMs are based on reconstruction of USAF pattern. (Source: Figure is adapted from [144], Copyright © 2020 IEEE)

4.7.4. Experimental validation with physical phantom

As a next step the performance of the proposed sTIR model was validated with actual measurements from a physical phantom. In this case the dot-grid pattern shown in Figure 4.12a was printed on paper and embedded in agar gel and scanned in the FOV of the handheld scanner as shown as a top view in Figure 4.12b. The side view photograph of the phantom experiment setup is depicted in Figure 4.12c. The reconstructed image of the cross-sectional scan using M_0 is displayed in Figure 4.12d. The distortion in the image due to local acoustic speed mismatch is similar to what was observed in the previous case of dot-grid numerical phantom. Subsequent M_0^{SIR} and M_0^{sTIR} based reconstructions depicted in Figure 4.12e-f was not successful to mitigate the distortion throughout the FOV as anticipated from previous experimental results. The refraction corrected reconstruction using M_R is displayed in Figure 4.12g, where radical improvement is observed in terms of localization and shape of absorbers. Thereafter refraction-based SIR and sTIR corrections (M_R^{SIR} and M_R^{sTIR} based reconstruction) are depicted in Figure 4.12h-i. It is again observed that SIR correction improves the shape of absorbers and sTIR correction improves contrast and sharpness. The axial and the lateral profiles across the marked absorber are plotted in Figure 4.12j-k for all six forward models along with the phantom. Again, this illustrates the improvement in shape and contrast using the sTIR model. Finally, the bar plot in Figure 4.12l illustrates the structural similarity indices of all the images reconstructed with six forward models. It is again observed that refraction-based models offer significantly higher similarity indices compared to the constant acoustic speed models. The SSIM index offered by M_R^{sTIR} is slightly lower compared to the SSIM index offered by M_R^{SIR} and this irregularity can be due to the system noise and inaccuracy of the membrane model.

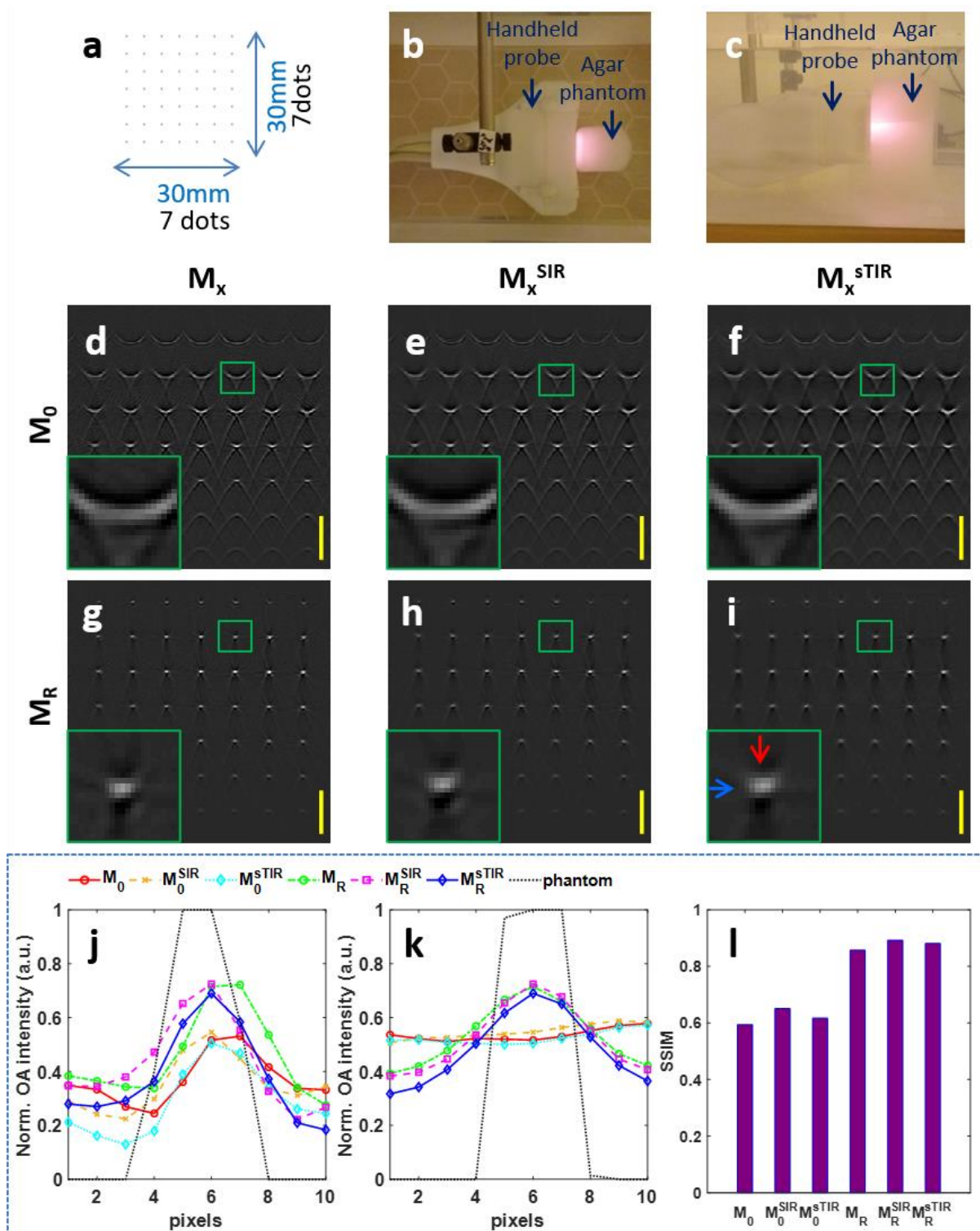


Figure 4.12: Improvement in reconstruction of physical phantom using the sTIR models. A physical phantom bearing a printed dot grid pattern was scanned with the handheld probe immersed in a water bath using excitation wavelength of 700nm. (a) Schematic of the dot grid pattern which was printed on paper. (b-c) Top and side view photographs of the agar phantom being scanned with the handheld probe. (d-i) Reconstructed images of the physical phantom using the M_0 forward model (upper row) or M_R forward model (lower row) without correction for transducer properties (left column), with SIR correction (middle column) or sTIR correction (right column). The axial and lateral line profiles are

marked using red and blue arrows. **(j-k)** Plots of axial (*upper*) and lateral (*lower*) line profiles across images reconstructed using M_0 , M_0^{SIR} , M_0^{sTIR} , M_R , M_R^{SIR} , M_R^{sTIR} and phantom. **(l)** Structural similarity indices of reconstructions using all six models. Scale bar, 5 mm. (Source: Figure is adapted from [144], Copyright © 2020 IEEE)

4.7.5. Clinical measurements

Moving away from laboratory phantoms it is important to evaluate if the proposed M_R^{sTIR} model could improve the clinical image quality in comparison to the standard M_0 model which is based on constant acoustic speed. Hence, the human forearm was scanned using the handheld scanner at two locations Scan 1 and Scan 2 as depicted in Figure 4.13. These regions in the forearm contain many shallow vessels that are good optical absorbers [67], [149] and has less density of hair. Melanin present in superficial hair acts a strong absorber in optoacoustic imaging and often hampers deeper imaging. For these two reasons inner side of the forearm was a suitable choice for clinical scans.

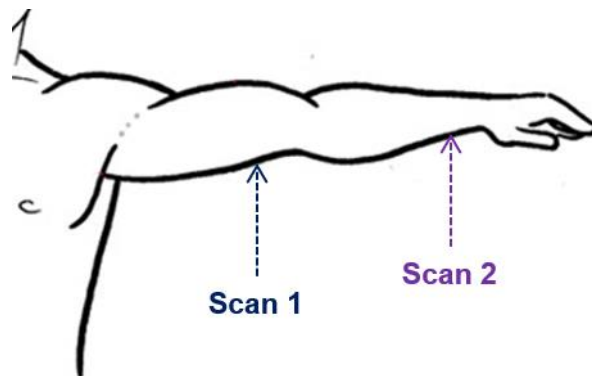


Figure 4.13: Schematic of locations of clinical scans. Locations of human forearm where two clinical scans were performed.

The cross-section tomographic image of Scan 1 using the model M_0 , based on constant acoustic speed and without TIR correction is depicted in Figure 4.14a. The acoustic speed has been chosen manually in order to optimize the image quality. Even though several longitudinal or cross section running vessels of varying sizes are observed, they appeared to be distorted. Figure 4.14b depicts the corresponding image of Scan 1 reconstructed using sTIR model. Selected cross-sectional and longitudinally running vessels marked in red, green and blue boxes are presented in higher magnification in panels Figure 4.14c-e and Figure 4.14f-h to highlight the improvement in vascular structures with sTIR correction. Comparison of panels Figure 4.14c-f one can easily observe the reduction of distortion in deeply seated vascular structure.

Comparing the panels Figure 4.14d-g it is observed that the sTIR model not only improves the sharpness of the vascular edge but also significantly suppresses background noise. A pair of longitudinal and cross-sectional vessels close to each other is shown in panels Figure 4.14e-h. Comparing these panels it can be easily observed that sTIR correction substantially improves structural quality of fine vessels and enhances resolution to around 200 μ m. This implies the usefulness of the proposed method in microvasculature imaging. Next the radial artery was imaged in Scan 2. The image corresponding to Scan 2 reconstructed using M_0 is displayed in Figure 4.14i depicting clear distortion of the radial artery. As usual constant acoustic speed for M_0 reconstruction has been chosen manually for optimal image quality. Figure 4.14j displays the M_R^{sTIR} based reconstruction or sTIR corrected reconstruction presenting some enhancement in the structural quality of radial artery (as marked with green box) and other surrounding vessels. The handheld scanning probe is usually pressed onto the skin surface for proper contact of the membrane with the skin surface. Since the rigid edges of the handheld probe is pressed upon the wrist, the cross-section of the radial artery is expected to appear as elliptical which seems to be recovered by sTIR correction. Nevertheless, the structural quality improvement of deep vascular structures in Scan 2 is not as strong as the one encountered in Scan 1 as depicted on comparison of zoomed in panels Figure 4.14k-m and Figure 4.14n-p. This could be accounted to the slight deformation of the membrane shape from flat (Scan1) to curved (Scan 2) as observed by comparing the reconstructed images of Scans 1 and 2 in the Figure 4.14. In general, it is observed that sTIR correction provides better image quality revealing more natural shape of vessels and reconstructing the skin line free of artefacts. Reconstruction of Scans 1 and 2 with all the six models listed in Table 1 are provided in Appendix A for detailed reference.

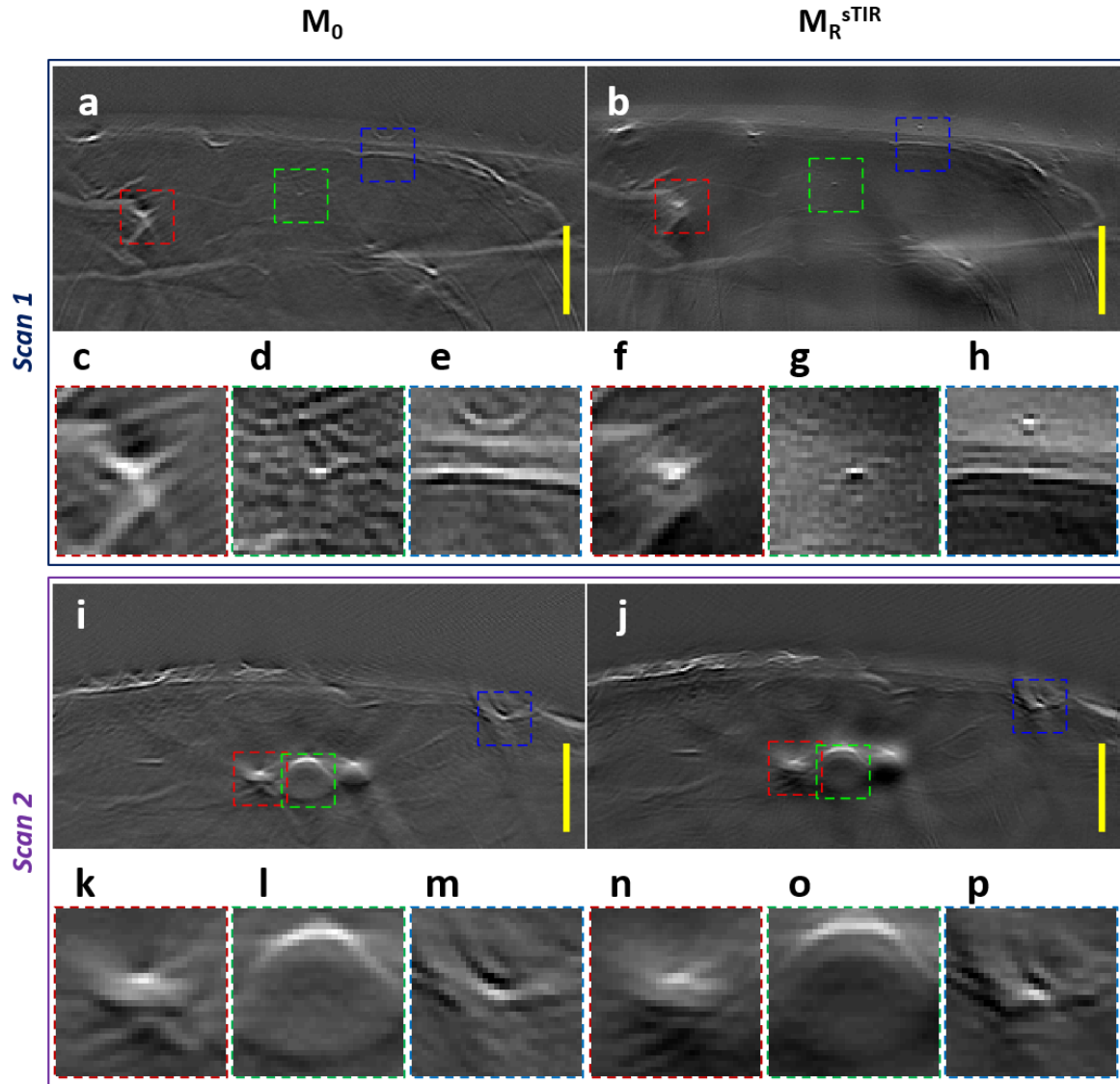


Figure 4.14: Improvement in reconstruction of clinical images using sTIR model. Non-invasive clinical scans were performed on healthy volunteers at two locations on the arm with the handheld probe using single excitation wavelength of 800 nm. **(a-b)** Reconstructed images of Scan 1 using M_0 and M_R^{sTIR} . **(c-e)** and **(f-h)** are higher magnification images of locations marked with red, green and blue boxes inside panels a and b respectively. **(i-j)** Reconstructed images of Scan 2 using M_0 and M_R^{sTIR} . **(k-m)** and **(n-p)** are higher magnification images of locations marked with red, green and blue boxes inside panels i and j respectively. Scale bar, 5 mm. (Source: Figure is adapted from [144], Copyright © 2020 IEEE)

4.7.6. Robustness of sTIR against variation of acoustic speed in tissue

It is a well-known fact that acoustic speed varies slightly in soft tissue depending on composition. For practical purposes, an average acoustic propagation speed is chosen to represent bulk tissue properties. The proposed sTIR reconstruction considers exact acoustic speed in coupling medium and an optimal acoustic speed in tissue representing the average acoustic propagation speed in tissue. By doing so the sTIR reconstruction offers the best spatial resolution throughout the field of view without refraction-based artefacts. On the contrary constant acoustic speed-based reconstruction suffers from refraction-based artefacts as the wave fronts do not converge. This phenomenon has been vividly demonstrated using the reconstruction of dot-grid phantoms. Hence, in practice while using constant acoustic speed-based reconstruction one must manually tune the value of c_0 to bring different regions of FOV to convergence. The biggest advantage of using the proposed model sTIR is that it provides accurate reconstruction throughout the FOV as demonstrated using previous reconstructions. To evaluate this robustness feature for clinical images, reconstructed performance must be tested with slight variation in the assumed acoustic speed. Scan 1 data was reconstructed using M_0 , assuming acoustic speed, c_0 varying from 1410m/s to 1420m/s in steps of 5m/s around the reference value of 1415m/s and displayed in the left column as shown in Figure 4.15a-c. The same data reconstructed using M_R^{sTIR} , assuming tissue acoustic speed c_t varying from 1450m/s to 1460m/s in steps of 5m/s around the reference value of 1455m/s are displayed in parallel as shown in Figure 4.15d-f. Insets of all panels show the zoomed-in images of the same vascular structure marked in red (M_0 reconstruction) and green (M_R^{sTIR} reconstruction). On comparison of the two columns of Figure 4.15, it can be observed that the proposed sTIR model or M_R^{sTIR} reconstruction offers less distortion in vascular structures. This is due to the fact that the acoustic wave fronts converge better with the proposed M_R^{sTIR} model compared to M_R^{sTIR} as anticipated.

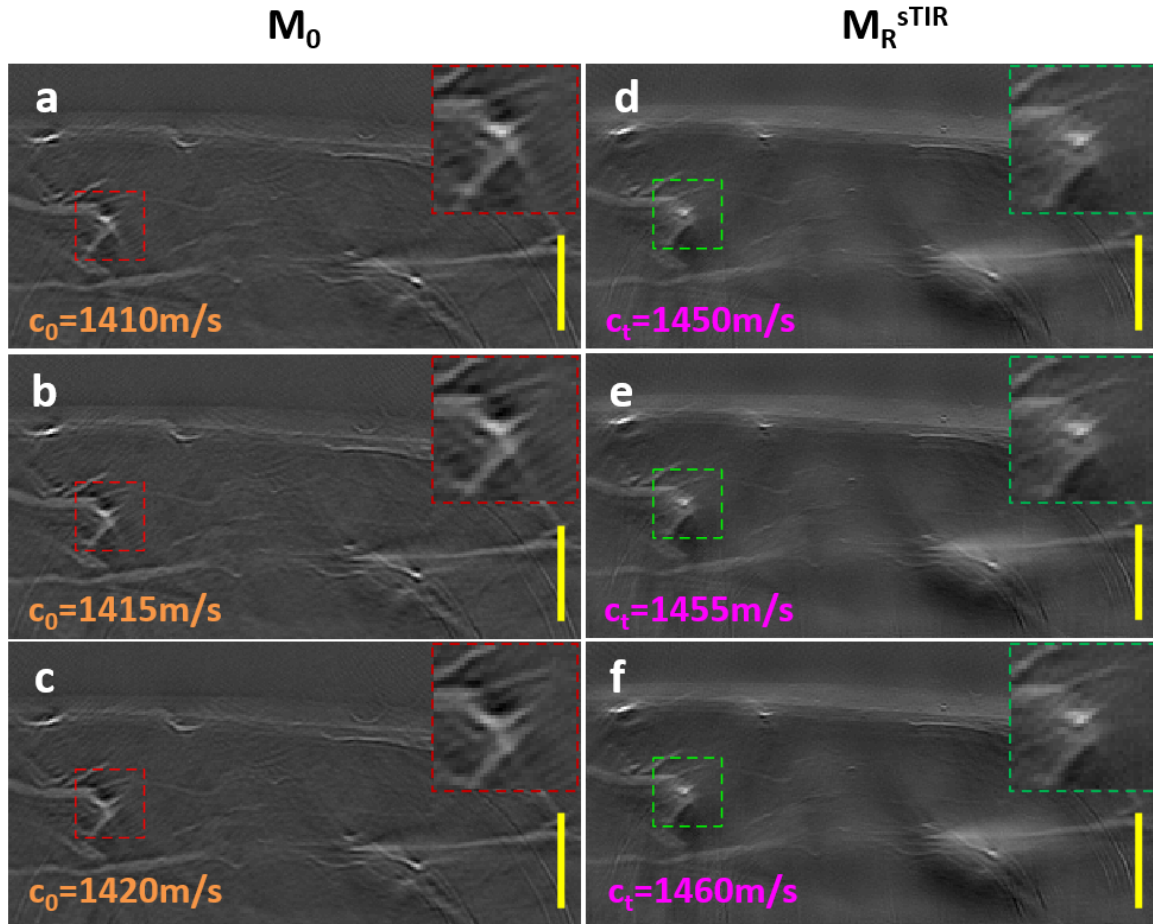


Figure 4.15: Evaluation of robustness of M_0 and M_R^{STIR} models against slight variation of acoustic speed in tissue. (a-c) Reconstruction of Scan 1 using model M_0 considering $c_0=1410$ m/s, $c_0=1415$ m/s and $c_0=1420$ m/s respectively. (d-e) Reconstruction of Scan 1 using model M_R^{STIR} considering $c_0=1450$ m/s, $c_0=1455$ m/s and $c_0=1460$ m/s respectively. Insets show the zoomed in views of the same vessel marked in red and green boxes for M_0 and M_R^{STIR} respectively. Scale bar, 5 mm. (Source: Figure is adapted from [144], Copyright © 2020 IEEE)

4.8. Discussion

In this chapter, a novel method of synthetic characterization of the handheld probe has been presented using TIR measurement at one location of the FOV and numerical modeling the refraction and SIR in the full-FOV of the handheld probe. It was hypothesized that the SIR being spatially dependent could be effectively modelled throughout the FOV and the spatially independent component EIR could be experimentally derived from at least one TIR measurement. Moreover, the accuracy of the simulated SIR has been verified to demonstrate that the experimentally derived EIR was independent of source of impulse. Thereafter, the synthetic TIR or sTIR was obtained by combining the modelled SIR with the experimentally derived approximate EIR (aEIR). It is important to note that the sTIR model takes into account the mismatch of acoustic speed between sample and coupling medium which is an important aspect of the limited view clinical handheld scanning probe. The sTIR forward model has also been incorporated into model-based reconstruction framework to produce considerable improvements in image quality throughout the FOV.

To study the components of sTIR, the entire pipeline of image generation has been modelled from generation of optoacoustic impulse to conversion into electrical signals. First, the refraction in propagation of acoustic waves have been modelled at the interface of the sample and the coupling medium. Second, the averaging of acoustic wave fronts on the active surface of the transducer has been modelled using SIR. In this step, the refraction has also been accounted using concept of virtual source. Third, the conversion of acoustic pressure to electrical signals is represented as aEIR. To systematically evaluate the various components of sTIR, namely – refraction, SIR and aEIR, six forward models were considered. Three refraction based forward models were constructed: for just refraction correction, for refraction-based SIR correction and for full refraction-based sTIR correction. To compare the performance with the existing methods, three constant acoustic speed-based models were constructed in parallel. Overall, the six models were used to report the experimental results in this chapter. Numerical simulations were presented to illustrate the negative effects of neglecting transducer properties in reconstruction algorithm. The proposed sTIR model significantly improved the system resolution as demonstrated by the reconstruction results of single microsphere phantom. The reconstruction results of the dot-grid physical phantom validate the performance of the proposed sTIR model and finally the image quality improvement was demonstrated using clinical scans from healthy volunteers.

Another important finding of the work presented in this chapter is that the spatially varying component, SIR depends on refraction of acoustic waves. The acoustic speed in heavy water at room temperature is 1397 m/s [155], which is fairly different from the average acoustic speed in tissue which is considered to be 1540 m/s [156]. This mismatch of acoustic speed across the membrane interface leads to significant refraction. The distortion of the sensitivity field in presence of refraction as presented in this chapter clearly indicates the importance of modelling SIR along with refraction which was achieved using the concept of virtual source. Hence, the proposed sTIR model has been developed using SIR based on refraction across the membrane surface. Consequently, the sTIR correction produced artefact-free images and achieved uniform accuracy throughout the FOV as it is evident from the reconstruction results of dot-grid phantoms. Also, it was observed that the numbers of the USAF chart were legible only in the images reconstructed with sTIR model including all the transducer properties. In general, it can be observed from most of the experimental results that refraction caused greater distortion compared to SIR or EIR, probably due to the configuration of the handheld probe used in this work which uses heavy water as a coupling medium. The reason behind this specific configuration is discussed in the next paragraph.

It has been found from previous studies [31], [60], [66]–[68] that heavy water is a suitable coupling agent in case of clinical handheld scanners. The advantages of using heavy water against water as a coupling medium for optoacoustic imaging lies in the fact that heavy water absorbs less in the near-infrared region making it easier to image clinically important endogenous chromophores such as hemoglobin and lipids [149], [159]. It is expected that the proposed sTIR model will facilitate the use of handheld probes with heavy water as coupling medium for clinical studies.

The resolution characterization presented in this chapter demonstrates enhancement in lateral and axial resolutions by 54% and 37% respectively, ultimately achieving approximately 230 μm in lateral dimension and 200 μm in axial dimension. The results from clinical reconstructions demonstrates visualization of vessels down to 200 μm diameter in depths of around 1.5 cm in tissue. This shows potential for imaging of smaller blood vessels under the skin and reveal signs of disease which induces changes in vascular structure [160], [161].

In summary, it was found that refraction produces strongest artefacts due to significant mismatch of acoustic speed across membrane. SIR correction slightly improves the shape of the absorbers and EIR correction improves the image resolution and contrast. Overall, sTIR correction with different speed of sound significantly enhances image accuracy compared to

standard constant acoustic speed enabling better visualization of vascular structures for clinical studies.

5. Characterization of individual transducer element response

This chapter introduces a robust characterization method for individual transducer element response and demonstrates improvement in image quality by including them into the forward model. The previous chapter describes the sTIR characterization method where the aEIR was the average response of all the transducer elements in the array. However, this chapter describes a robust characterization method of individual transducer element response calling it isTIR (individual synthetic Total Impulse Response) and illustrates improvement of image quality using isTIR. First the motivation behind the individual transducer characterization has been discussed. Then computational method and the experimental setup to derive the individual aEIR has been illustrated. Thereafter, image quality improvement using isTIR compared to previously demonstrated sTIR has been demonstrated using single microsphere and grid scan over different locations of FOV. Finally, the effect of individual transducer response on clinical image reconstruction has been analyzed.

5.1. Motivation

The electrical and physical properties of the transducer elements significantly influence the image quality in the context of tomographic imaging. If tomographic data is recorded using a single transducer element revolving around the sample [162] then characterization of the impulse response of that transducer element would be sufficient. Yet, in practice an array of transducer elements is used to simultaneously record data from different projections both in pre-clinical [20], [44] and clinical [31], [149] optoacoustic imaging systems. The main advantage of using array-based transducer is to facilitate simultaneous signal capture ultimately leading to higher scanning speeds. In such a case, the assumption of identical response for all transducer elements in the array may not be valid. In a typical optoacoustic tomographic system, the aperture of each element is large in the elevation to enable stronger sensitivity in the azimuthal plane. Hence, the microscopic deviation in shape (radius of curvature in elevation) would not significantly distort the captured signals and in addition to that modern machining practices are precise enough to neglect such miniscule errors. However, even slight variation of EIR from element-to-element can have pronounced effect on image quality as EIR is intricately linked to material, packing and electronics etc which are prone to manufacturing errors. For instance, the importance of characterization of such variability of individual transducer responses has been highlighted in ultrasound literature [91] for identification of defective elements and quality control [163] purposes. Failing to include such individual transducer

element response into the reconstruction algorithm may degrade the image quality in handheld optoacoustic tomography.

The main challenge to characterize an array based tomographic system lie in the arduous dense grid scan method and the problem is intensified by the acoustic property mismatch between sample and coupling medium. Now, as a first step to address this overall characterization problem the sTIR model has been proposed in the previous chapter. The EIR for each element was derived using simple deconvolution procedure based on TIR measurement of a single point which was not robust enough to measurement noise. Thereafter, derived EIRs from all the transducer elements in the array were averaged to obtain aEIR, which was used to build sTIR model. Hence, there was a need to develop a robust method to first characterize the aEIR of each transducer element.

5.2. Individual synthetic TIR (isTIR)

This section describes the characterization of isTIR in a step by step fashion with formulation of the problem using a system of linear equations and iterative least square solver to derive the aEIR of individual transducer elements. To begin with, the discrete optoacoustic forward equation is revisited. The pressure signal detected by a transducer element located at r_e due to an optoacoustic source located at r' was written in discrete form as

$$s_{r_e, r'}[n] = f_{r'} \cdot h_{r_e}^{aEIR} * m_{r_e, r'}^R[n - n_R], \quad (5.1)$$

where,

$$m_{r_e, r'}^R[n] = h_{c_c, c_t, r_e, r'}^{SIR} * p_{c_c}^N[n - n_R], \quad (5.2)$$

Here, $f_{r'}$ denotes the intensity of the reconstructed image which corresponds to the initial pressure at the location r' . The experimentally derived EIR for the transducer element located at r_e is denoted by $h_{r_e}^{aEIR}$, which is again temporally convolved with the numerically modelled term $m_{r_e, r'}^R$. The term $m_{r_e, r'}^R$ consists of numerically simulated term $h_{c_c, c_t, r_e, r'}^{SIR}$, the SIR of the transducer element and $p_{c_c}^N$, the numerically modelled optoacoustic response of a spherical absorber. It is important to note that the numerically modelled term $m_{r_e, r'}^R$ consists of the signal components which are dependent on refraction and in turn the location of the source r' , relative to the location of the transducer element r_e . The time of flight of the refracted acoustic wave from source to the transducer element via membrane interface is denoted by n_R . As described

in Chapter 3, this time of flight depends on the acoustic speed in coupling media and sample (e.g. soft tissue) denoted by c_t and c_c respectively. Next, the equations (5.1) and (5.2) will be used to derive the EIR for individual transducer elements.

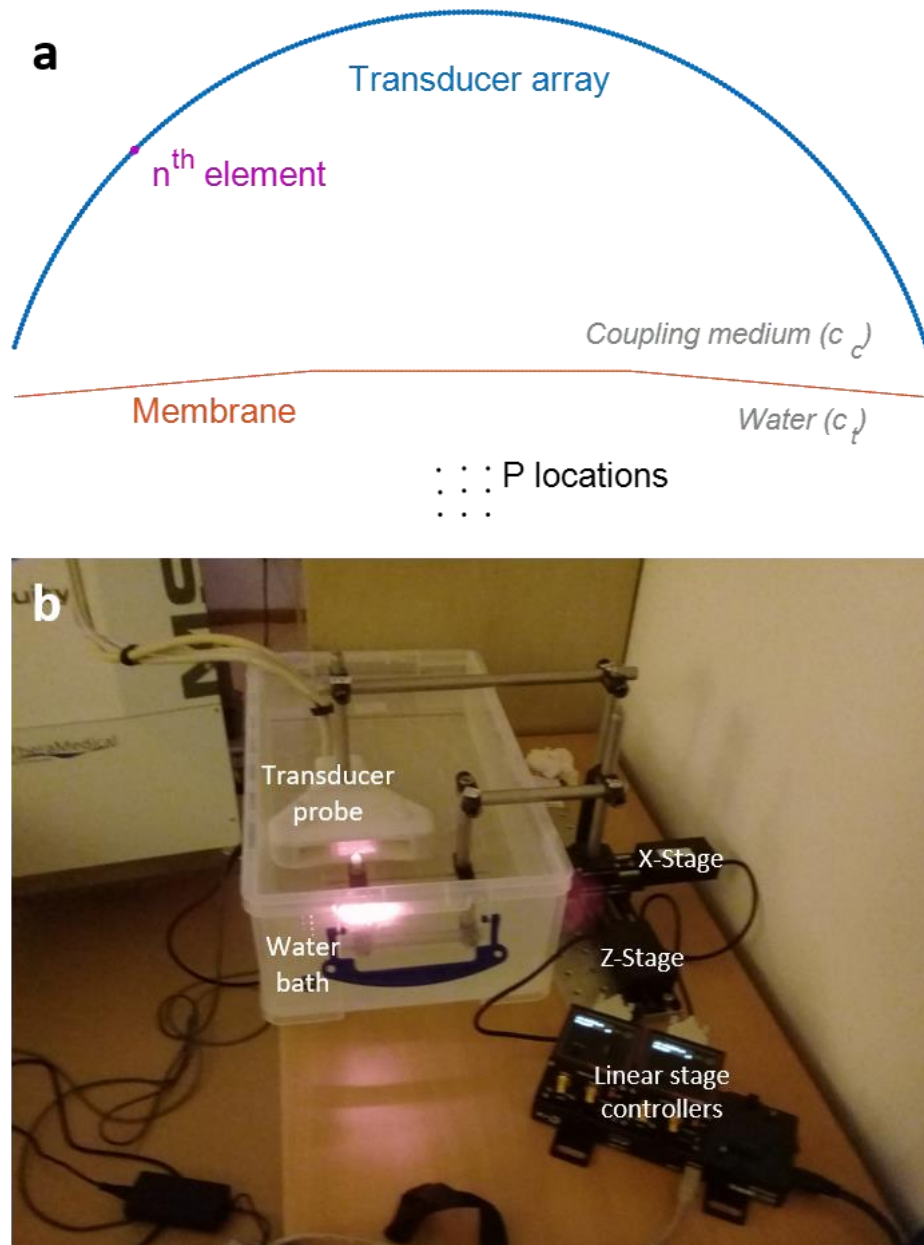


Figure 5.1: Characterization of individual transducer response. (a) Schematic of the handheld transducer array showing P locations where a microsphere was scanned to derive the individual aEIR of n^{th} element in the array. (b) Photograph of the measurement setup showing the physical realization of the individual aEIR derivation concept.

5.2.1. Measurements in multiple locations

Figure 5.1a shows the schematic of the individual EIR derivation concept. The goal was to derive the aEIR for n^{th} transducer element using an overdetermined system of linear equations using measurements at P locations. This concept was physically realized using the measurement setup shown in Figure 5.1b where multiple measurements of single microsphere were performed at P different locations of the FOV. The microsphere and the handheld transducer probe were submerged in a water bath during the measurements. The microsphere was placed in P different locations of FOV using a custom made 2-axis linear translation stage (Thorlabs, Inc. USA). The translation stages were programmed to place the microsphere sample to a location in the x-z plane using an external computer. Since the system described in this work is a commercial and closed one, the full-grid measurement could not be automated using trigger from external computer towards the MSOT system. First the microsphere was placed at a certain location and then the data was recorded using onboard controls in MSOT system. This experiment was only feasible as the grid was sparse ($P = 9$). The recorded signals represent the LHS (left hand side) of (5.1). After having the measurements done in a sparse grid, the corresponding locations of the microspheres were computed using refraction corrected reconstruction and information on these locations r' were fed to the input of the next step of SIR simulation.

5.2.2. Modelling of SIR and pixel response at measured locations

The SIR component $h_{c_c, c_t, r_e, r'}^{SIR}$ of the term $m_{r_e, r'}^R$ was simulated using Field-II [115] by discretizing the surface of the transducer element with square sub-apertures of $50 \mu\text{m}$ in length. Like previous approach the SIR has been computed using virtual source concept including the effects of refraction. The term $p_{c_c}^N$ was modelled as “N”-shaped [100] optoacoustic response from a homogenously absorbing solid sphere equal to the dimension of the microsphere used in the measurement which was $100 \mu\text{m}$ in diameter.

5.2.3. Derivation of individual aEIR

After having measured the signals on the LHS of (5.1) and modelled the $m_{r_e, r'}^R$ term on the right hand side of (5.1), the aEIR for n^{th} element $h_{r_e}^{aEIR}$ is now the unknown that needs to be determined. In this case each transducer element is indexed by $q = 1, 2, \dots, Q$, with $Q = 256$ being the total number of elements in the transducer array. Since, the same microsphere was used for all the P measurements, the term $f_{r'}$ can be dropped in (5.1) and a system of equations

can be constructed using P measurements (as depicted in Figure 5.1) at grid locations $p = 1, 2, \dots, P$ as

$$s_{q,p}[n] = h_q^{aEIR} * m_{q,p}^R[n - n_R], \quad (5.3)$$

The convolution using $m_{q,p}^R$ in (5.3) being a linear operation, can be done using Toeplitz matrix multiplication in order to obtain as a system of linear equations given by

$$\begin{bmatrix} s_{q,1} \\ s_{q,2} \\ \vdots \\ s_{q,P} \end{bmatrix} = \begin{bmatrix} Tm_{q,1}^R \\ Tm_{q,2}^R \\ \vdots \\ Tm_{q,P}^R \end{bmatrix} \cdot h_q^{aEIR}, \quad (5.4)$$

where $Tm_{q,p}^R$ represent the Toeplitz matrix corresponding to $m_{q,p}^R$ and h_q^{aEIR} denote the approximate EIR of q^{th} transducer element, which is yet to be determined.

Finally, the equation (5.4) can be solved using least squares to obtain the aEIR of the q^{th} transducer element as

$$h_q = \arg \min_{h_q} \|Th_q - s_q\|_2^2 + \lambda \|h_q\|_2^2, \quad (5.5)$$

where standard Tikhonov regularization was used and the optimal regularization parameter λ was determined using L-curve.

Using (5.5) the aEIR for all the 256 elements were derived as shown in the Figure 5.2. The variation of response from element-to-element is clearly observable from the EIR map across all 256 elements shown in Figure 5.2a. The energy of the aEIR responses were used to derive the sensitivity of the transducer elements. The normalized sensitivity profile is plotted in Figure 5.2b depicting considerable variation in sensitivity across elements.

5.2.4. isTIR forward model

The derived individual aEIR, h_q^{aEIR} for corresponding transducer elements denoted by $q = 1, 2, \dots, Q$, with $Q = 256$, can be combined with the numerically modelled terms – SIR and pixel responses to construct the isTIR forward model as

$$s_{r_e}[n] = \sum_{r' \in FOV} f_{r'} \cdot m_{r_e, r'}[n - n_R], \quad (5.6)$$

$$\text{where } m_{r_e, r'}[n] = h_q^{aEIR} * h_{c_c, c_t, r_e, r'}^{SIR} * p_{c_c}^N[n]. \quad (5.7)$$

Considering the location of pixels in the FOV be indexed by (i,j) where $i=1,2,\dots,M$ and $j=1,2,\dots,N$ for an image of dimensions $M \times N$ pixels, (5.7) takes the form of isTIR forward model matrix $M = [m_{q,(i,j)}]$. It is to be noted that the sTIR model included h^{aEIR} (from (4.12)), which is the average of the aEIRs of all transducer elements while isTIR model includes h_q^{aEIR} , which consists of aEIRs of all the 256 transducer elements. Finally, arranging the pixel responses in lexicographical order (5.6) can be written in forward matrix equation as

$$s = \mathbf{M}f, \quad (5.8)$$

which can be inverted to obtain the reconstructed image f .

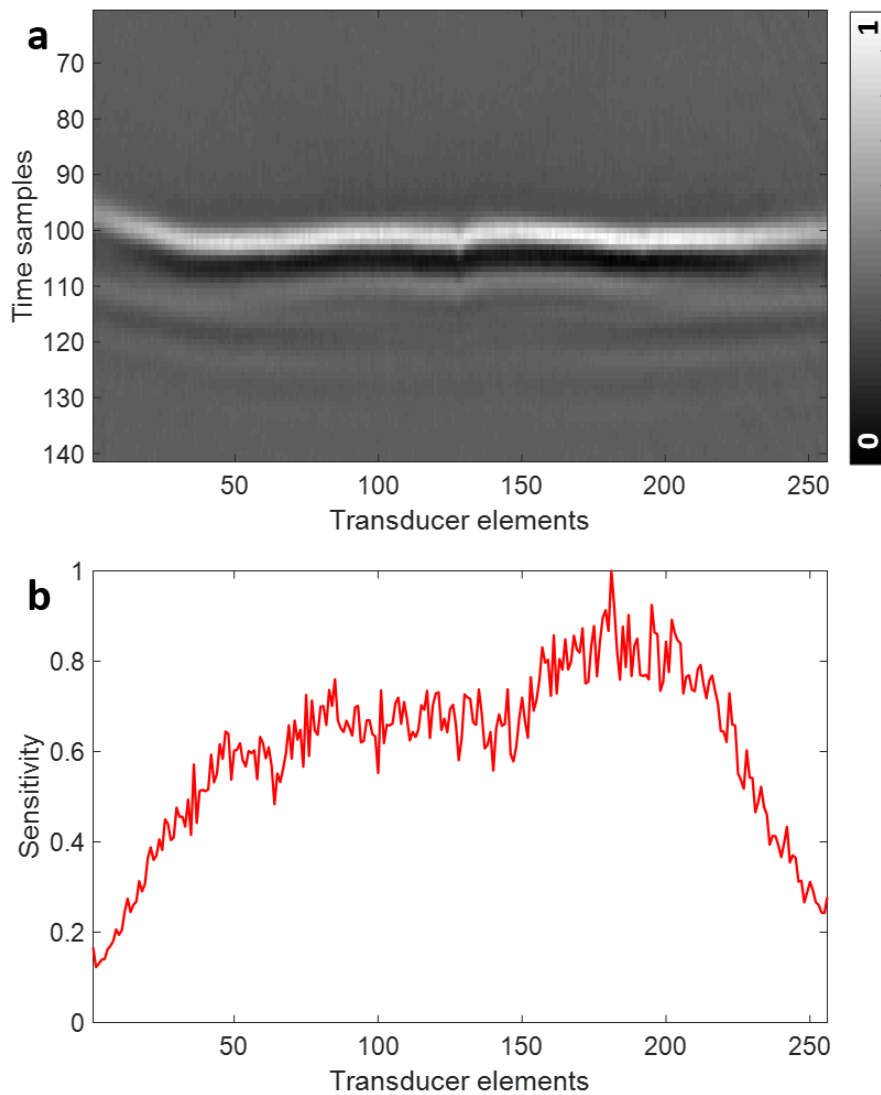


Figure 5.2: Variation of aEIR across transducer elements. (a) 2D matrix representation of element-to-element variation of aEIR with temporal response in vertical axis and transducer elements in the horizontal axis. **(b)** Normalized sensitivity profile across all the transducer elements.

5.3. Image correction using isTIR

The isTIR model generated in the last section will be used in the model-based reconstruction framework to demonstrate the improvements in image quality on correction for individual transducer responses. The performance of the isTIR model will be evaluated with respect to the previously developed sTIR model and hence to maintain uniformity in analysis throughout this thesis same optoacoustic imaging platform and reconstruction framework are used.

5.3.1. Image correction framework

As a first step, the recorded signals were preprocessed with a Butterworth bandpass filter with a lower cutoff of 100kHz to reject the dc component and other slow varying parasitic effects and a higher cutoff of 12MHz to reject the high frequency noise outside the sensitivity range of the transducer. Thereafter these preprocessed signals are lexicographically ordered to build the column vector s' of the discrete forward equation given by

$$s' = \mathbf{M}f, \quad (5.9)$$

where the two forward model matrices can be denoted by $\mathbf{M} \in \{M_R^{sTIR}, M_R^{iTIR}\}$ for sTIR and isTIR corrections respectively. The initial pressure f was reconstructed by inverting (5.9) using regularized least squares as described in (4.7) of Section 4.6. Note that isTIR includes the aEIR of each element into the forward model reducing the sparsity and increasing the size of the model matrix very similar to sTIR and hence conventional schemes for automatic choice of regularization parameters becomes computationally infeasible. Hence, a LSQR type method was used to choose the regularization parameter which will be discussed in detail in Chapter 0.

5.3.2. Experimental measurements

The experimental results presented to compare isTIR against sTIR were based on optoacoustic scans of three classes – single microsphere, grid of microspheres and clinical.

The single microsphere phantom was constructed by embedding a microsphere of diameter 100 μm in agar gel. The agar gel was prepared by a 1.5% (w/v) solution of agar. The approximate diameter of the microsphere used was smaller than the theoretically achievable resolution [88]. To obtain a measurement in a grid, this single microsphere agar phantom was placed in different locations of a rectangular 6x7 grid using a two-axis motorized translation stages. Assessing the quality of image reconstruction in different locations of the FOV would be suitable to judge the performance of the proposed isTIR method. The spacing between two consecutive grid locations in both x and z axis was around 3 mm.

For microsphere agar phantom optoacoustic data from multiple laser shots at a single wavelength – 700 nm was captured and the average over all the captured frames were considered for reconstruction to suppress background noise related to laser and data acquisition electronics.

As a final step, the performance of isTIR was compared to that of sTIR based on clinical scan of healthy human volunteer where the data was recorded at 800nm (isosbestic point of Hemoglobin absorption). To preserve uniformity in the thesis, the Scan 1 of upper arm from Subsection 4.7.5 was chosen to present the results in the next section. The presence of numerous small to medium sized vessels in the Scan 1 also favored this choice.

5.4. Results

This section presents the results of the experiments performed with the handheld scanner using the isTIR model which includes the responses from individual transducer elements in the array. To compare with the previously proposed method, the reconstruction results were also presented in parallel using sTIR which includes the average response of all the transducer elements in the array. First the system resolution has been characterized using a single microsphere and then the improvement of image quality in different parts of the FOV has been evaluated using the grid scan. Finally, the improvement in image quality of clinical scan will be presented.

5.4.1. Characterization of system resolution

The resolution achieved using the proposed isTIR reconstruction has been characterized using a single microsphere of diameter $\sim 100 \mu\text{m}$ placed roughly at the center of the FOV. Figure 5.3a shows the reconstructed image of the microsphere using the sTIR model and some star like artefacts are visible. Figure 5.3b shows the reconstructed image using the isTIR model. The images were normalized to their respective maximum values even though negative values are present. Comparing the two panels Figure 5.3a-b one can easily observe that isTIR eliminates the star like artefacts around the microsphere and tends to improve the isotropic shape of the spherical absorber. Figure 5.3c-d displays the corresponding images in panels Figure 5.3a-b trimming the negative values which are unreal optoacoustic contrast. Panels Figure 5.3c-d also highlight the enhancement in image quality on using isTIR model compared to sTIR model. In order to evaluate the improvement in isotropic shape, analysis in the Fourier domain would be useful due to rotation property of 2D Fourier transform and hence the log of magnitudes of the 2D Fourier transforms of the reconstructed images using sTIR and isTIR models are presented

in Figure 5.3e-f respectively. It is to be noted that the resolution measured as the FWHM of the line profile across the microsphere image would correspond to the radius of the circular disc in the Fourier domain. The resolution achieved using isTIR was around 125 μm which was marked in cyan dashed circle in the panels Figure 5.3e-f. Comparing the panels Figure 5.3e-f it can be easily noticed that with isTIR reconstruction the circular disc is more uniform compared to that of the sTIR model indicating strong isotropic shape improvement on correction of individual transducer responses. Also, the dashed green lines mark the limited view sectors where the transducer fails to capture information due to limited angular coverage of the curved array. It is also observed that isTIR correction attempts to fill in the blind sector to smoothen out the abrupt transition implying reduction of streak artefacts [86].

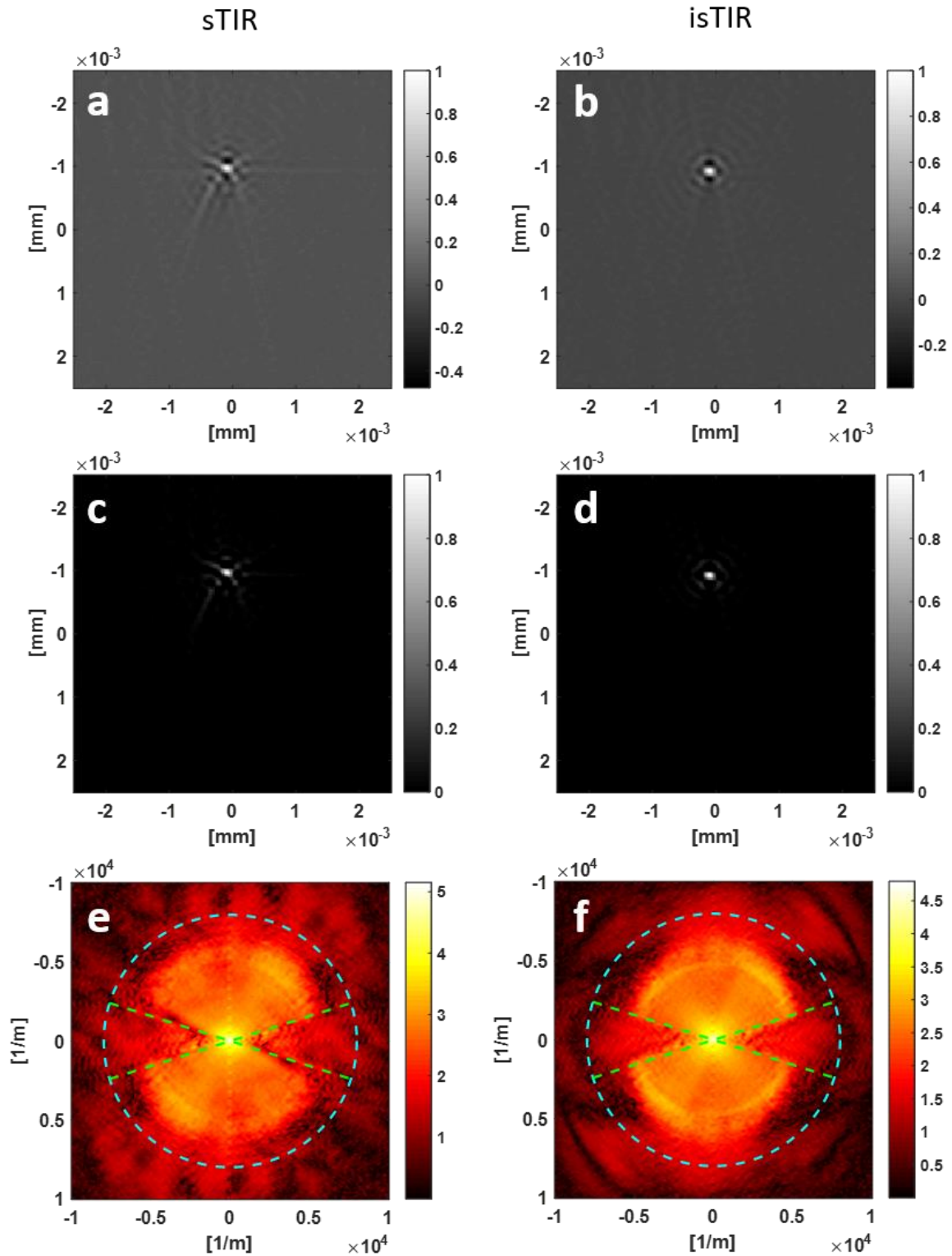


Figure 5.3: Improvement in isotropy and resolution. (a-b) Images of the single microsphere located approximately at the center of the FOV of the handheld scanner, using sTIR and isTIR models, respectively. (c-d) Images with negative values trimmed to zero corresponding to panels a and b, respectively. (e-f) 2D Fourier transforms of the images reconstructed using sTIR and isTIR models, respectively.

5.4.2. Reconstruction of grid scan

After having observed significant improvement in isotropic resolution using the isTIR model, it would be imperative to evaluate the reconstruction quality in other locations of FOV of the handheld scanner. Here we present the results of reconstruction of the grid scan of the microsphere phantom. Figure 5.4a displays the reconstruction of the grid scan in a bigger FOV of dimension 20 mm x 20 mm using the sTIR model. On the other hand, Figure 5.4b displays the reconstruction of grid scan in the same FOV using isTIR model. A superficial comparison of panels Figure 5.4a-b reveal that isTIR model eliminates the short streak artefacts at almost all the absorber locations. To validate this observation a closer look is required and hence zoomed in images would be suitable. However, to avoid pixilation high resolution reconstructions were performed with 25 μm image discretization and zoomed in images were rendered. Figure 5.4c presents the zoomed in images of locations 1-4 marked in magenta in the sTIR reconstruction. Similarly, Figure 5.4d presents the zoomed in images of the same locations 1-4 marked in cyan in the isTIR reconstruction. Comparing panels Figure 5.4c-d it is again evident that the isTIR model in most cases reduces or rather eliminates the artefacts and preserves the isotropic resolution closely representing the microspheres as circularly shaped absorbers.

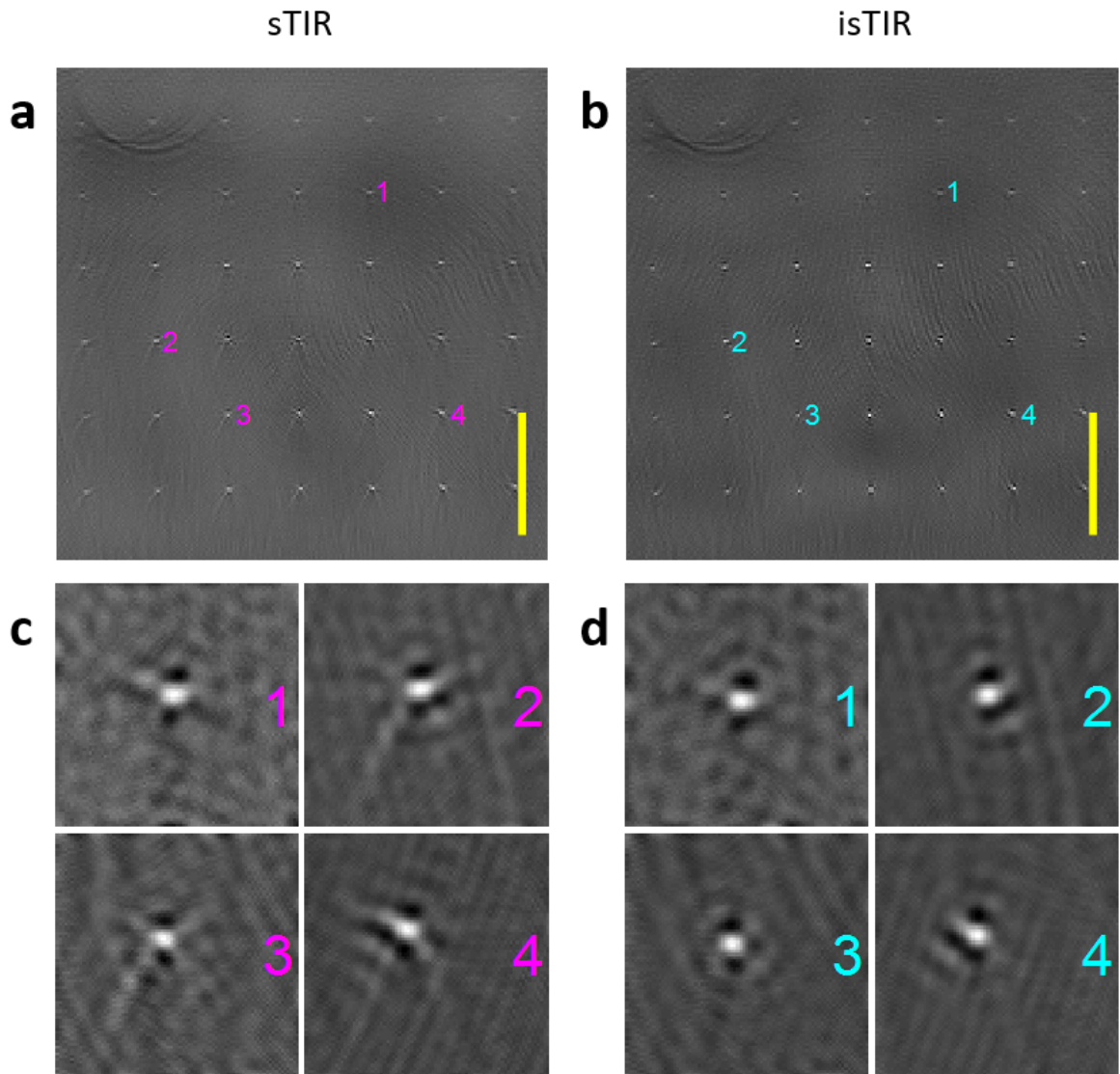


Figure 5.4: Improvement in isotropic resolution throughout the FOV of the grid scan. (a-b) Images of microsphere grid reconstructed using sTIR and isTIR respectively. Scale bar is 5mm. (c-d) Zoomed images of microspheres at corresponding locations 1-4 marked in the panels a and b using magenta (sTIR) and cyan (isTIR) respectively.

5.4.3. Clinical measurements

Convinced with the promising results from phantom experiments as a final step the performance of the isTIR is evaluated on Scan 1 data, recorded from upper arm of healthy volunteer. Figure 5.5a shows the image of Scan 1 reconstructed using sTIR model and Figure 5.5b shows the reconstructed image of the same dataset using isTIR model. Both the reconstructions were performed on the data recorded based on single wavelength 800 nm which is the isosbestic point of Hemoglobin absorption. Comparing panels - Figure 5.5a-b visually, it was not easy to observe any considerable improvement on using isTIR model apart from slight improvement in contrast. Once again high resolution zoomed in image were reconstructed to judge the improvement in image quality rendered by isTIR model. Figure 5.5c-d shows the zoomed in images of the locations in panels Figure 5.5a-b marked with magenta using dashed box (sTIR reconstruction) and solid box (isTIR reconstruction) respectively. Figure 5.5e shows the cross-sectional line profiles across a vessel with dashed red line (sTIR) or blue line (isTIR). Only slight improvement in resolution and contrast was observed. Again, Figure 5.5f-g displays the zoomed in images of the locations in panels Figure 5.5a-b marked with cyan using dashed box (sTIR reconstruction) and solid box (isTIR reconstruction) respectively. Figure 5.5h shows the cross-sectional line profiles across the horizontal vessels with dashed red line (sTIR) or blue line (isTIR). Comparing the lines profiles only meagre improvement in resolution and contrast was observed. Overall, the improvement in image quality using the isTIR reconstruction in clinical datasets was not as significant as it was reported in case of physical phantoms.

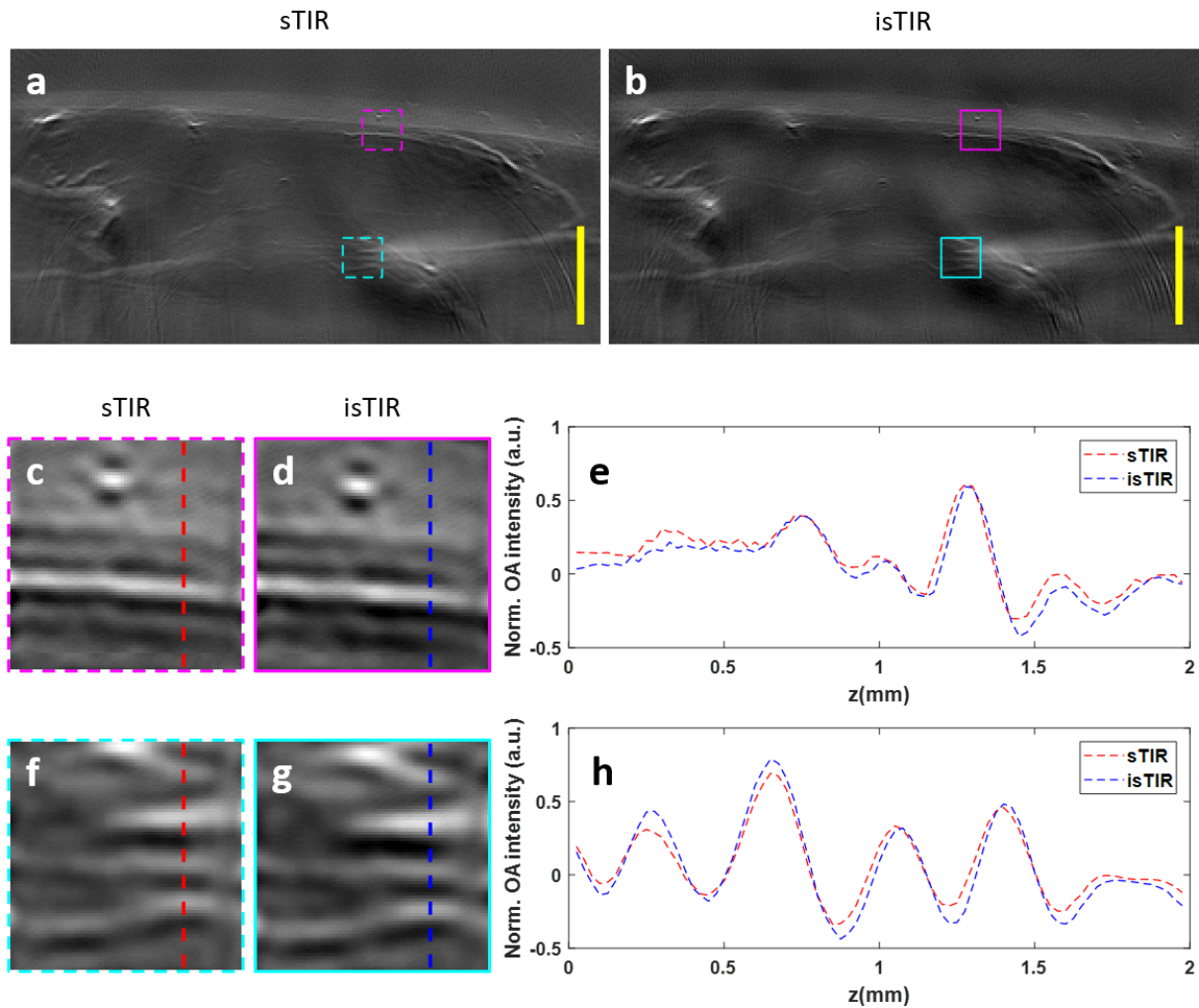


Figure 5.5: Improvement in clinical images. (a-b) Images of Scan 1 reconstructed using sTIR and isTIR models, respectively. (c-d) Zoomed images of locations in panels a and b marked with magenta using dashed (sTIR) or solid (isTIR) boxes. (e) Plots comparing the line profiles across the horizontal running vessel in panels c and d using red (sTIR) and blue (isTIR). (f-g) Zoomed images of locations in panels a and b marked with cyan using dashed (sTIR) or solid (isTIR) boxes. (h) Plots comparing the line profiles across the horizontal running vessels in panels f and g using red (sTIR) and blue (isTIR).

5.5. Discussion

This chapter presented a robust characterization method to capture the responses of individual transducer elements in the handheld array in a challenging setting of significant acoustic speed mismatch between sample and coupling medium. The negative effects of the individual transducer responses on image quality has been highlighted. In addition to that the isTIR model has been presented which incorporates the individual aEIR of each transducer element into the forward model. The performance of the isTIR model was compared to the previously demonstrated sTIR model with average transducer aEIR using optoacoustic scan of single microsphere phantom. To evaluate the reconstruction accuracy in the FOV of the scanner, a grid scan of the microsphere was also presented. Lastly, the performance was tested on clinical scans recorded from healthy human volunteer.

To derive the individual transducer response, signal measurements were performed from a microsphere at few locations in the FOV of the handheld scanner. Thereafter, a system of equations was formulated using the modelled OA response of the sphere and the SIR of the transducer. The Toeplitz matrix representation was used to obtain an overdetermined system of linear equations which was solved using regularized least squares to obtain the approximate EIR of each transducer element in the array. Later these responses were integrated into the forward model with other simulated (OA response and SIR) components to construct the isTIR model. Same model-based reconstruction framework was used as stated in previous chapter, to report the results of reconstruction from phantoms and clinical scans.

The most important observation in this chapter was that the correction of individual transducer response significantly improved the isotropic resolution as spotted from the vanishing of the streak like artefacts in the reconstruction of the microsphere phantoms. A closer look using Fourier 2D transform revealed that isTIR reconstruction led to a smoothness in the angular direction clearly indicating that usage of the isTIR model led to an image closely resembling the natural shape of a microsphere. The reduction of streak like artefacts was also observed in the reconstructed image of the grid scan of microspheres placed at different locations. It is important to note that such deeper investigation of isotropy in resolution required reconstruction in a fine resolution grid which was possible due to core advantage of the proposed forward model that they can be generated at any custom ROI in the FOV.

It was also observed that even though isTIR reconstruction demonstrated considerable improvement in case of phantoms, similar scale of improvement in image quality was not

observed in the case of clinical scans. The isTIR model delivered only marginally better resolution and contrast in rendering of vascular structures. It is to be noted that all results presented in this work were based on discrete pixel modelled using a homogenous solid sphere. As a future scope the pixels for high resolution reconstruction could suitably be modelled as overlapping spheres with Gaussian distribution [164], [165]. Also, non-negative constrained inversion utilizing projected conjugate gradient method [166] could also be considered. An extended version of the work presented in this chapter was published (2nd publication as mentioned in list of publications at the end of this document).

In summary it was found that individual transducer characterization indeed reveals element-to-element variability in responses and sensitivity often identifying faulty detectors. Including these into the forward model improves the isotropy in resolution of the reconstructed image and thereby reducing streak like artifacts as noticed from the phantom reconstructions. However, the improvement in overall image quality correcting for individual transducer responses in case of clinical scans remains insignificant.

6. Efficient inversion for optoacoustic image reconstruction with sTIR

This chapter describes an efficient inversion method utilizing hybrid regularization to tackle the problem of model matrix becoming a dense matrix due to incorporation of transducer properties. The model-based image reconstruction framework consists of the final step of inversion which maps the preprocessed signals to the reconstructed image by inverting the forward model. Inversion is an important problem of research in the domain of optical and optoacoustic image reconstruction. Depending on the reconstruction method used, a suitable inversion scheme is chosen. The reconstruction method proposed in this thesis incorporates transducer responses into the forward model resulting in a dense model matrix. This leads to unrealistic computational load for obtaining a regularized solution using conventional methods. The motivation behind search for efficient inversion scheme is discussed in the first section. Then the theoretical concepts behind the hybrid regularization based on bidiagonalization is reviewed. Thereafter the implementation of one such hybrid regularization called LSQR based inversion is discussed which was used in the reconstructions presented in this thesis. Finally, the results of using LSQR based inversion in the context of handheld optoacoustic scanner geometry is discussed with proposal for future research directions.

6.1. Motivation behind the hybrid regularization

Model-based reconstruction methods offer the advantage of inclusion of various properties related to the components of the imaging system [17]. This enables sophisticated modelling of the image formation process to achieve better image quality. Complex forward models including exclusive models of imaging components may lead to accurate reconstruction but at the cost of longer inversion times [97]. On the other hand, too much approximation may lead to faster reconstruction but at the cost of poor image quality. Therefore, a tradeoff must be made to choose the right model with inversion efficiency. Accurate forward models would not require regularization, and Moore-Penrose pseudo-inverse will be sufficient to obtain accurate solution. The advantage of pseudo-inverse is that it only depends on the imaging system characteristics and furthermore, regularization is not required to obtain the solution for the recorded data. However, the limitation lies in the fact that complex forward models cannot be inverted due to huge memory requirements. Optoacoustic data is recorded at limited number of locations around the sample and therefore regularization is often used to obtain a reasonable solution for the ill-posed problem. Again, regularization depends on the dataset to be reconstructed, and hence it is desirable to automatically choose the regularization parameter for

each reconstruction. Forward models where transducers are approximated as point detectors with infinite bandwidth considerations can exploit the sparsity of the model matrix to achieve reasonably fast inversion times [97], [98]. For example, Figure 6.1a illustrates that a mathematically modelled OA response consists of a large number of zeros which can be used to build a sparse model matrix. Figure 6.1b on the other hand shows the recorded signal with almost all non-zero elements. The recorded signal consists of TIR as discussed in Chapter 4 and this eventually reduces the sparsity of the forward model matrix and increases the memory requirement of the model matrix. The dense model matrix due to the inclusion of transducer properties prohibits the use of Moore-Penrose pseudo-inverse, where reconstruction results are independent of the recorded data. Also, obtaining a regularized least squares solution becomes ineffective due to unreasonably long computation times. In addition to that using conventional L-curve based choice of regularization parameter becomes impossible due to the shortage of storage memory of the matrix. The improvement of image quality due with inclusion of sTIR outweighs the computational costs in many clinical studies. Therefore, there was a need to explore inversion schemes to complement with the advantages of the sTIR forward model.

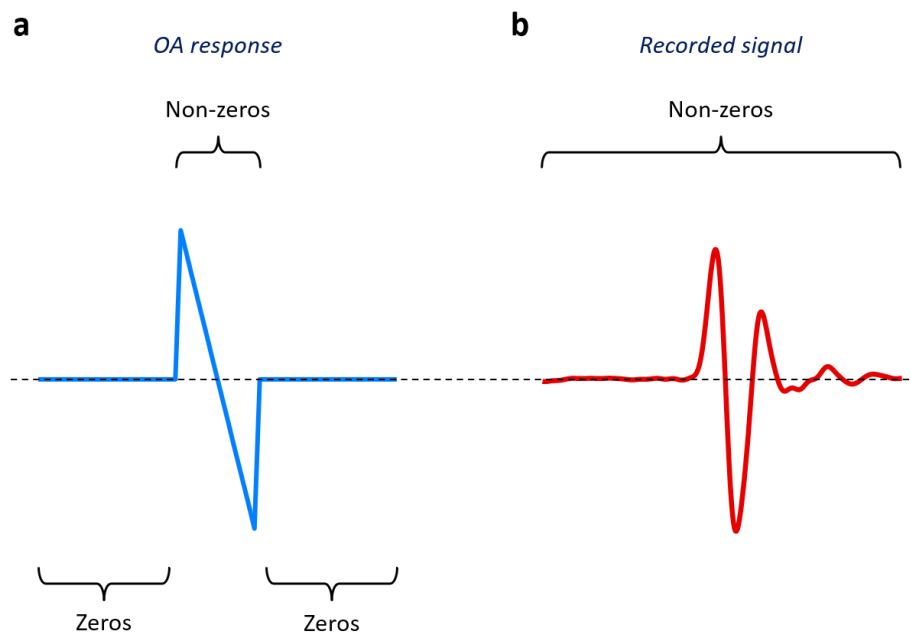


Figure 6.1: Zeros in modelled signals. (a) Ideal OA response showing significant number of zeros. (b) Recorded signals containing TIR showing absence of zeros.

There are three classes of regularization which can be used for tomographic inversion problems such as direct, iterative and hybrid [167]. The most common direct regularization methods are TSVD, Tikhonov and Damped SVD, etc are only suitable for inversion of smaller model matrices typically for smaller FOV. Iterative regularization methods like conjugate gradient and LSQR are suitable for inversion of large and sparse matrices which originate for tomographic reconstruction in large FOV [92], [97], [103]. These methods have been used for model matrices using point detector approximation. The typical sTIR/isTIR models for the clinical reconstructions in 30 mm x 15 mm FOV (used in this thesis) was a sparse matrix of dimension 273408 x 45451 occupying a storage memory of around 3.3 gigabytes. Hybrid regularization based on bidiagonalization schemes are known to be effective for such large and sparse models [168]–[170]. The next section briefly describes the concept of hybrid regularization based on bidiagonalization.

6.2. Hybrid regularization based on bidiagonalization

The iterative methods which are often used to solve large scale inversion problems uses bidiagonalization and with each iteration the bidiagonal matrix builds up in size until convergence. The hybrid regularization can be achieved by modifying the iterative LSQR method by using a direct internal regularization at each step of the iterative process [167]. This can be achieved by using direct regularization scheme such as Tikhonov in each step of QR factorization of the bidiagonal matrix B_k and continuing the process of Lanczos bidiagonalization process to build up the bidiagonal matrix B_k . However, it is important to derive theoretically the equivalence between the solutions obtained using bidiagonalization regularization and the LSQR solution of damped least squares.

Let us consider the system of linear equations $Ax = b$, where b is the set of measurements and the forward model is denoted by A . The solution is denoted by x , which represents the image to be reconstructed. First, the solution using bidiagonalization regularization will be derived. In LSQR method, Lanczos bidiagonalization is used on the model matrix A to compute three matrices – the left orthogonal matrix $U_k \equiv [u_1, u_2, \dots, u_k]$, the right orthogonal matrix $V_k \equiv [v_1, v_2, \dots, v_k]$ and the bidiagonal matrix B_k . After k iterations, the Lanczos bidiagonalization process produces [170]

$$b = \beta_1 u_1 = \beta_1 U_{k+1} e_1, \quad (6.1)$$

$$AV_k = U_{k+1} B_k, \quad (6.2)$$

$$A^T U_{k+1} = V_k B_k^T + \alpha_{k+1} v_{k+1} e_{k+1}^T, \quad (6.3)$$

where e_k is the k^{th} unit vector. The main diagonal of the matrix B_k contains the scalars α_k while the lower subdiagonal contains the scalars β_k . For least squares solution of $Ax = b$ one would require the residual norm be minimized

$$\min_{x \in S} \|Ax - b\|_2^2, \quad (6.4)$$

where S denotes the k -dimensional subspace spanned by the first k vectors of v_i . The solution is required in the form $x^{(k)} = V_k y^{(k)}$ for some $y^{(k)}$ of length k . The corresponding residual is defined as $r^{(k)} = b - Ax^{(k)}$. Using (6.1) one can write

$$r^{(k)} = \beta_1 U_{k+1} e_1 - AV_k y^{(k)}, \quad (6.5)$$

Using (6.2) one can write

$$r^{(k)} = U_{k+1} (\beta_1 e_1 - B_k y^{(k)}), \quad (6.6)$$

With U_k having orthonormal columns, the projected problem to be solved is

$$\min_{y^{(k)}} \|\beta_1 e_1 - B_k y^{(k)}\|_2^2. \quad (6.7)$$

Now, the if the projected problem for some integer k is to be regularized using standard Tikhonov where $L = I$ or identity matrix, then [170]

$$\min_y \|\beta_1 e_1 - B_k y\|_2^2 + \lambda^2 \|y\|_2^2, \quad (6.8)$$

or,
$$\min_y \left\| \begin{bmatrix} B_k \\ \lambda I \end{bmatrix} y - \begin{bmatrix} \beta_1 e_1 \\ 0 \end{bmatrix} \right\|_2^2. \quad (6.9)$$

Then the update $y_\lambda^{(k)}$ is given as the closed form solution [170]

$$y_\lambda^{(k)} = (B_k^T B_k + \lambda^2 I)^{-1} \beta_1 B_k^T e_1. \quad (6.10)$$

Next, the LSQR solution of the damped least squares [171] will be derived by adding the standard Tikhonov regularization at the beginning to solve $Ax = b$ using

$$\min_x \|Ax - b\|_2^2 + \lambda^2 \|x\|_2^2, \quad (6.11)$$

or,

$$\min_x \left\| \begin{bmatrix} A \\ \lambda I \end{bmatrix} x - \begin{bmatrix} b \\ 0 \end{bmatrix} \right\|_2^2. \quad (6.12)$$

And the solution satisfies the symmetric system [171] given by

$$\begin{bmatrix} I & A \\ A^T & -\lambda^2 I \end{bmatrix} \begin{bmatrix} r \\ x \end{bmatrix} = \begin{bmatrix} b \\ 0 \end{bmatrix}, \quad (6.13)$$

Thereafter, application of Lanczos bidiagonalization process [171] to the above system gives

$$\begin{bmatrix} I & B_k \\ B_k^T & -\lambda^2 I \end{bmatrix} \begin{bmatrix} t_{k+1} \\ y_k \end{bmatrix} = \begin{bmatrix} \beta_1 e_1 \\ 0 \end{bmatrix}, \quad (6.14)$$

$$\begin{bmatrix} r_k \\ x_k \end{bmatrix} = \begin{bmatrix} U_{k+1} & 0 \\ 0 & V_k \end{bmatrix} \begin{bmatrix} t_{k+1} \\ y_k \end{bmatrix},$$

It can be observed from (6.14) that y_k is the solution of another damped least square problem given by

$$\min_{y_k} \left\| \begin{bmatrix} B_k \\ \lambda I \end{bmatrix} y_k - \begin{bmatrix} \beta_1 e_1 \\ 0 \end{bmatrix} \right\|_2^2, \quad (6.15)$$

whose closed form solution can be written as

$$y_k = (B_k^T B_k + \lambda^2 I)^{-1} \beta_1 B_k^T e_1. \quad (6.16)$$

Finally, comparing (6.9), (6.10) with (6.15), (6.16) the equivalence between the solutions using bidiagonalization regularization and the damped least squares is established. Hence, bidiagonalization regularization can be effectively used in our case with standard Tikhonov as the internal regularization from the beginning of the iteration of the Lanczos process. However, there is a still a need to find the optimal regularization parameter in hybrid regularization. This will be addressed in the next section.

6.3. LSQR based choice of regularization parameter

The previous section dealt with the concept of hybrid regularization based on bidiagonalization and established equivalence with the solution of damped least squares. However, since regularization depends on the recorded data, it is important to choose the regularization parameter in an automated fashion. This problem has been addressed in the domain of diffuse optical tomography (DOT) [157]. The authors used LSQR-type method to find optimal regularization parameter in an automated fashion. The performance of this method has also been tested in photoacoustic tomographic reconstruction [172]. However, this demonstration was only on synthetic numerical phantom with data recorded in full angular view. Inspired by the effectiveness of this LSQR-type method, the same approach has been adopted in this work

for real experimental datasets acquired in limited angular view of handheld scanner. The algorithm [157], [172] used to determine optimal regularization depends on finding the optimal number of iterations in the following way –

- (i) Estimation of the optimal λ , for each iteration k (λ_{opt}^k) using the Simplex method in the range of $[0 \lambda_{max}]$
- (ii) Computation of x^k for the given iteration with $\lambda = \lambda_{opt}^k$ using (6.10).
- (iii) Estimation of residual norm $r^k = \|M \cdot f_{sol} - s\|_2^2$ for the given iteration. The optimal number of iterations, k_{opt} is obtained at the minimal value of residual norm r^k and optimal regularization is given as $\lambda_{opt} = \lambda_{opt}^{k_{opt}}$

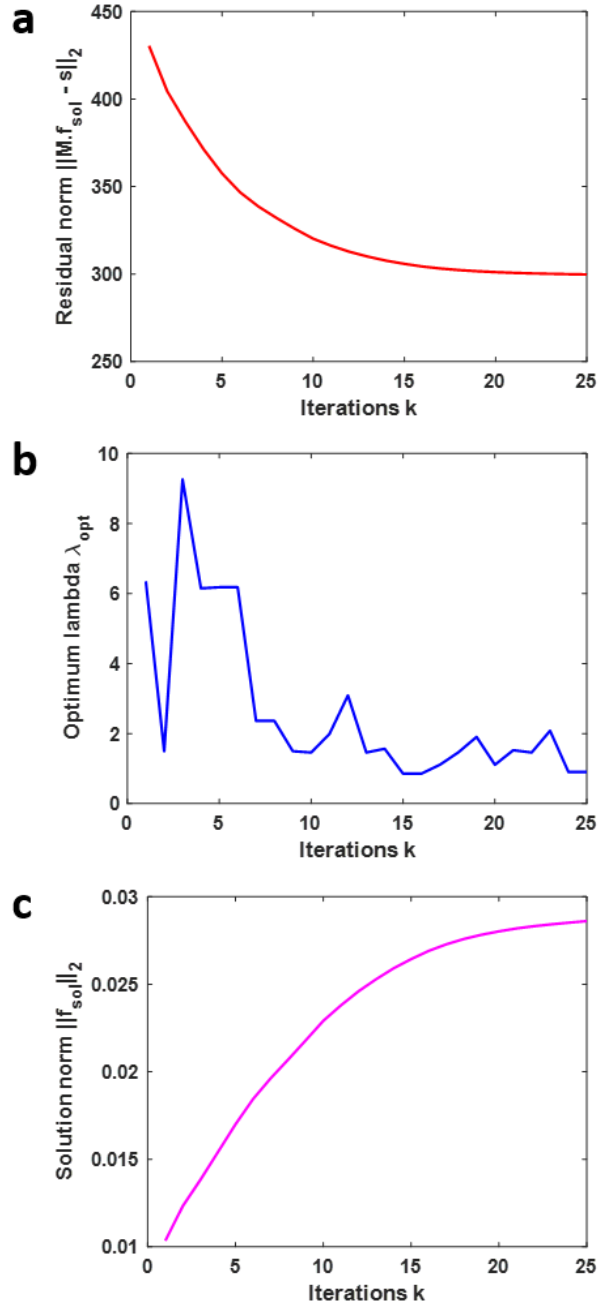


Figure 6.2: Hybrid regularization. Plots of residual norms, optimum lambda, and solution norms against number of iterations for sTIR reconstruction of clinical scan 1 dataset. **(a)** Plot of residual norm $\|M_R^{sTIR} f_{sol} - s\|_2$ against iterations k, **(b)** Plot of λ_{opt} against iterations k, and **(c)** Plot of $\|f_{sol}\|_2$ against iterations k.

The minima found in the plots of residual norm vs iterations led to the automatic choice of the optimal regularization parameter in the studies which used numerically simulated phantoms with full angular view of data acquisition [104], [157]. However, in the case of actual experimental dataset with limited view it was observed that the residual norm gradually settles to a certain value without providing a minima. Figure 6.2 shows the dynamics of residual norm,

optimal lambda and the solution norm by increasing the number of iterations for an exemplary dataset Scan 2 with sTIR reconstruction. It can be easily observed from Figure 6.2a that the residual norm reaches a saturation after 15th iteration and also the optimal lambda varies within a small range after 15th iteration as observed from Figure 6.2b. The iteration was stopped here and the solution corresponding to 15th iteration was chosen as beyond this iteration the “vertical stripes”-like noise start increasing even though the residual norm does not increase. This phenomenon is explained in the next paragraph in the context of choosing regularization parameter. The computation of the optimal lambda using a maximum of 25 iterations took approximately 5 mins and it was observed that the optimal lambda is fairly the same for a particular clinical dataset. Thereafter using fixed lambda for reconstruction of each frame took less than 40 seconds. All reconstructions were performed on a computer with Intel® Core™ i7-6700K CPU @ 4.00 GHz.

The choice of regularization parameter for the two models M_0 and M_R^{sTIR} is illustrated in Figure 6.3, where zoomed in images of a vessel were shown by increasing number of LSQR iterations and comparing the effect of regularization using the two models. Figure 6.3a,b shows the reconstructed images of Scan 1 dataset using the forward models M_0 and M_R^{sTIR} respectively. M_0 represents the conventional forward model based on constant acoustic speed and without inclusion of transducer properties while M_R^{sTIR} represents the forward model including the transducer properties and refraction effect due to mismatch of acoustic speed of sample and coupling medium. An ROI is chosen as marked in green dashed box showing the cross-section of a small blood vessel with no other strongly absorbing vessel in the vicinity. Therefore, the surrounding region can be treated as background. The zoomed images of the designated ROI for increasing number of iterations of the hybrid regularization are compared for M_0 and M_R^{sTIR} models in the Figure 6.3c. In the case of M_0 reconstruction (as shown in the top row of Figure 6.3c) it was observed that in the first few iterations sharp vessels appear with somewhat noisy background. However, with more iterations of the hybrid regularization beyond $k=2$, the high frequency noise represented by vertical stripes start appearing and become stronger. This was due to the fact the conventional model M_0 does not capture various system parameters such as transducer properties and the discontinuity in wave propagation medium. Stronger regularization starts producing high frequency noise mostly vertical lines probably because the transducer array has limited angular coverage. These artifacts might be due to the sparse nature of the model matrix, and probably the biagonalization procedure might not be efficient enough to handle sparse matrices. Hence, for fair comparison of image quality against the sTIR model, the iteration was stopped at $k=2$. The effects of hybrid regularization using the

M_R^{sTIR} model is shown in the bottom row of Figure 6.3c. It was observed that in the first few iterations the image looks blurry. This is due to the fact that the sTIR model has accounted for many physical parameters of the transducer probe and captured the effects of the actual system. The regularization can be stronger to find the appropriate solutions which can fit the recorded data. This could be one reason why there were no appearance of vertical stripes in the background until approximately 20th iteration. However, these vertical stripe like background noise starts appearing slowly beyond $k=20$. Therefore, the iteration was stopped at $k=20$ to choose the optimal regularized solution. It is important to note that in the chosen solution, the edges of the small blood vessels appear to be sharp indicating that the resolution is intact. The background appears to be smooth with low noise levels indicating higher image quality. Note that the present choice of regularization parameter is still not automatic. To choose regularization parameter automatically in this hybrid regularization method, an efficient stopping criterion must be defined which is discussed in the next section as a future scope.

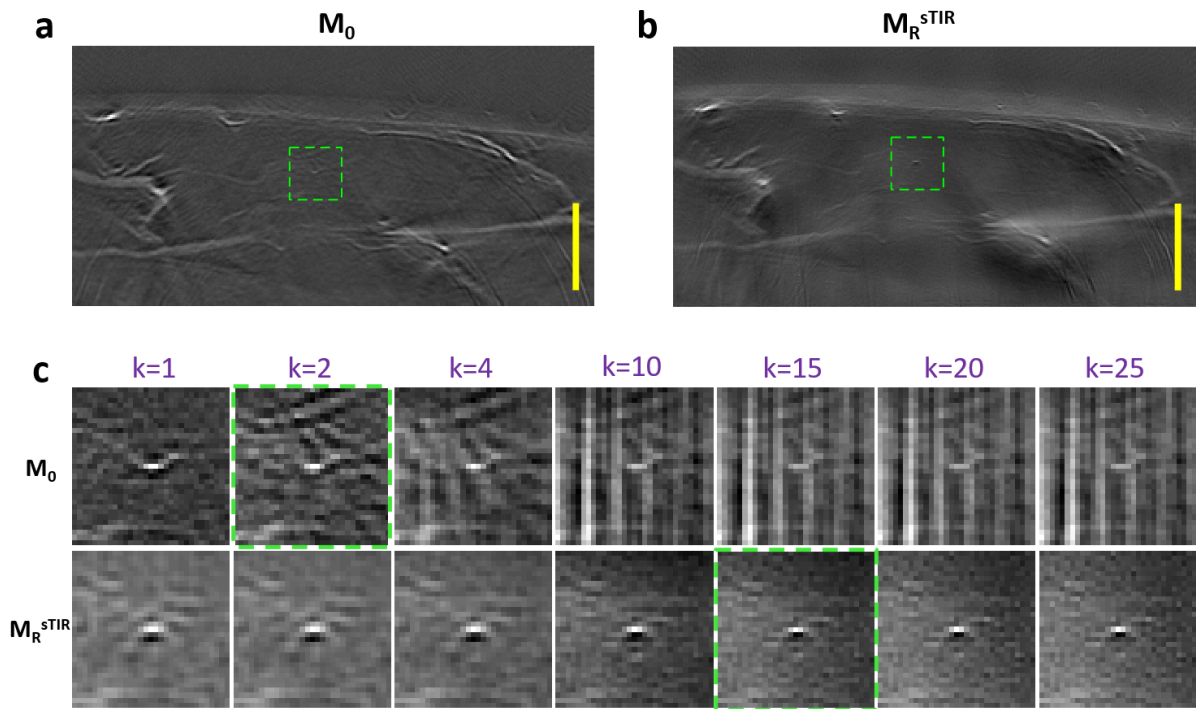


Figure 6.3: Illustration of choice of the regularization parameter using hybrid regularization method. (a) Reconstruction of Scan 1 data using the M_0 forward model. **(b)** Reconstruction of Scan 1 data using the sTIR forward model. **(c)** Zoomed-in images of locations marked in green with increasing number of iterations, which is denoted by k . Scale bar, 5 mm. (Source: Figure is adapted from supplementary document of [144], Copyright © 2020 IEEE)

6.4. Discussion

This chapter addressed the problem of computational burden due to inclusion of transducer properties into the forward model. The forward models in traditional model-based optoacoustic reconstruction exploits the sparsity of the model matrix to achieve efficient inversion. However, the inclusion of various physical properties of the imaging system reduces the sparsity of the forward model leading to the increased inversion times and often renders it impossible to use conventional methods to choose optimal regularization parameter. The benefits of development of forward models including TIR of the imaging system outweighs the computational load and hence the motivation behind the search for efficient regularization methods suitable for more comprehensive forward models such as sTIR/isTIR models was discussed. The bidiagonalization method which is a hybrid between iterative and direct regularization method was found to be suitable for the inversion of sTIR model and therefore theoretical description of this hybrid regularization method was provided. The equivalence between the bidiagonalization regularization and the LSQR based damped least squares was also established citing relevant literature. The LSQR based hybrid method to choose the regularization parameter which has already been used in photoacoustic tomographic image reconstruction was reviewed. The same LSQR type method was also used to solve the inverse problem in this work with reasonably good computational efficiency.

The main observation of the work presented in this chapter was that the implementation of the LSQR type method [157] to choose optimal regularization parameter in this case is not yet fully automatic as it was presented in the case of numerical phantom reconstruction [172]. This was probably since the transducer used in this thesis gathered data in limited angular view and the problem was more ill-posed. In addition to that in the actual recorded data consists of noise from different sources. One way to make this implementation of LSQR type method automatically choose regularization parameter for real datasets acquired from handheld scanners is to find a stopping criterion. Finding a suitable stopping criterion based on the noise levels of the imaging system/relative change in the residual norm can be considered as a direction of future research.

In summary it was shown that the development of comprehensive transducer model alone is not enough as it increases the computational time of inversion ultimately making it painful to use such sophisticated models (e.g. sTIR) for reconstruction of datasets from longitudinal clinical studies. Research on efficient inversion schemes is also necessary. Hence,

the presented hybrid regularization-based inversion along with sTIR model together offers a suitable solution towards high quality image reconstruction with good efficiency.

7. Conclusion

This chapter summarizes the achievements of the presented work towards the advancement of clinical handheld OAT imaging. The current limitations are discussed, and scope of future research directions are also provided.

7.1. Conclusive summary

Prior to the research developed in this thesis, existing model-based reconstruction was used to reconstruct the images from the data recorded by the limited view handheld probe for clinical optoacoustic imaging. Such models assumed the transducers to be point detectors with infinite bandwidth. Typically, water was used as a coupling medium in the proof-of-concept design of the handheld OAT scanners. However, it was envisioned that water being significantly absorbing at around 970 nm would make it difficult to image lipids and water deep inside soft tissue specifically in breast tissue. Therefore, the clinical handheld MSOT was equipped with heavy water as the coupling medium. The implications of such an upgrade on image quality was never thoroughly investigated. Even though model-based reconstruction schemes were earlier developed to include transducer properties, there were two major problems to import such schemes directly to clinical handheld MSOT imaging – i) existing TIR model-based reconstruction methods were based on constant acoustic speed and ii) thorough experimental characterization of handheld MSOT was a challenging task. Hence, there was a special need to develop an efficient method to characterize the entire handheld scanning probe and design reconstruction methods to incorporate the properties of the handheld transducer.

The primary goal of the work presented in this thesis was to develop an efficient method to characterize the clinical handheld MSOT scanner and include the transducer properties into the forward model to increase reconstruction accuracy. The secondary goal of the work was to investigate other aspects of the handheld scanner such as – image slice thickness, noise and illumination heterogeneity, which play a crucial role in determining the diagnostic value of the handheld MSOT system.

First, the optoacoustic wave detection mechanism starting from initial pressure generation to detection of electrical signals was mathematically modelled. The SIR and EIR due to transducer shape and material properties of the transducer were included using cascade of LTI systems. The physics of refraction of acoustic wave across the media interface was also taken into account. The dependence of the SIR on the refraction was explored and the concept of virtual source was introduced to numerically compute SIR in the context of refraction of

acoustic waves. Using measurement of signal from a microsphere of dimension lower than the resolution of the system, the aEIR of the entire transducer array was derived. The temporal convolution of such experimentally derived aEIR with the numerically modelled refraction-based SIR was termed as sTIR. This sTIR was then used to demonstrate significantly higher reconstruction accuracy using physical phantoms and clinical scans. Numerical phantoms were also used to demonstrate the adverse effects in image quality on neglecting the transducer properties. It was observed that refraction has stronger effects on image distortion in terms of localization. SIR and EIR was responsible for improving the image sharpness and contrast. Overall, sTIR led to a five-fold improvement in structural quality compared to conventional model-based reconstruction using a point detector and constant acoustic speed. The main advantage of the proposed sTIR model is that reconstruction results are robust and uniform throughout the FOV for a chosen pair of acoustic speed of tissue and coupling medium, while the image quality using conventional model-based reconstruction with a constant acoustic speed is not uniform throughout the FOV. Another big advantage of the sTIR characterization method proposed in the work is that it requires only one measurement from a point source in the imaging domain to derive the average EIR of the entire transducer array. Therefore, tedious full FOV dense experimental characterization of TIR can be avoided, which is risky for closed system or a commercial system such as MSOT Acuity.

The sTIR model used the average aEIR for all the transducer elements in the array. Some variation was observed among the aEIRs of the different transducer elements within the transducer array and the derivation of aEIR was not robust. Therefore, it was hypothesized that the derivation of individual aEIR of transducer elements and inclusion of them into the forward model could further improve the image quality. The individual aEIR derivation problem was formulated using a system of linear equations $\mathbf{Ax} = \mathbf{b}$, with x being the individual aEIR for one element and \mathbf{b} consisting of few measurements of point source in the FOV. The coefficient matrix \mathbf{A} was constructed using simulated SIRs corresponding to the locations of measurements in the FOV. Thereafter, regularized least square solver was used to obtain the aEIR for individual elements. This set of individual aEIRs were found to be robust to experimental noise. The isTIR model was constructed by combining the individual aEIRs with the simulated SIR based on refraction. The isTIR model was used to reconstruct images of microspheres located in a grid spanning the FOV. It was observed that the isTIR model improves the image quality throughout the FOV such that the reconstructed absorbers resemble more like a circle compared to those obtained with sTIR model. A detailed analysis using 2D Fourier transform of one such microsphere image reveals that correcting for individual transducer element response leads to

significant enhancement of isotropic resolution. Also, the performance of the isTIR model was evaluated using clinical scans. It was observed that the improvements in image quality in terms of resolution was not substantial in the clinical images.

It was observed that the inclusion of transducer properties, reduced the sparsity of the forward model matrix ultimately increasing the memory requirement i.e. a dense matrix. This led to unexceptional increase in inversion time. Also, conventional techniques to select optimal regularization parameter using L-curve became impractical. Hybrid regularization schemes were explored where direct internal regularization is used in each step of iteration to solve a large-scale problem. The LSQR type regularization was utilized to choose a suitable regularization parameter with a reasonable inversion time. Therefore, the advantages of much better image quality using the sTIR/isTIR models justified the exploration of LSQR type method to reduce the computational burden. Overall, the sTIR/isTIR forward model combined with the LSQR type inversion scheme is expected to raise the image quality of clinical handheld imaging.

The image slice thickness of the clinical handheld scanner was characterized using inclined suture phantom with varying angles. It was demonstrated that the slice thickness of the modelled sensitivity field map matched with that of the experimentally derived slice thickness in most of the FOV apart from the location close to the membrane. To investigate this anomaly the illumination profile of the handheld scanner was investigated, and it was observed that there was an offset of 7 mm from the plane of highest acoustic sensitivity. Also, there were two illumination spots arising from two groups of fiber bundles. The effect of these manifested in the reconstructed image of the phantom mimicking soft tissue. The noise present in the data acquisition was also characterized and the Gaussian trend of the background noise was estimated.

Overall, the presented impulse response correction methods combined with the hybrid regularization method is expected to improve the quality of images ultimately enhancing the diagnostic value of the handheld OAT systems.

7.2. Future outlook

The characterization and correction methods presented in this work makes it possible to efficiently capture a subset of properties of the clinical handheld scanners and provides a

framework to improve the image quality significantly. However, this comes at a computational cost which still needs to be addressed to achieve real time inversion.

The TIR models presented in this work captures the effects of refraction, SIR and EIR of the handheld scanner. The approximate EIR derived assumes ideal laser pulse, negligible ultrasound attenuation and negligible optical fluence decay. As a future direction of research, the effects of finite duration laser pulse, ultrasound attenuation and optical fluence decay can be incorporated into the forward model. This is particularly important with future exploration of clinical handheld system with LEDs instead of Lasers. The presented TIR model does not consider the heterogeneity in acoustic speed within soft tissue. Such a varying acoustic speed distribution in soft tissue can be additionally incorporated into the forward model as a future work.

The results presented throughout the work was based on a fixed membrane model which was based on the line approximation of the rigid edges of front face. During clinical scans, some pressure is applied to ensure proper contact of the scanner surface and the skin. This leads to slight deformation of the non-rigid membrane which seals the coupling medium inside the transducer cavity. The deformed membrane takes the shape of the curvature of the skin and thus deviates from the fixed membrane model. This led to minor distortion of vascular structures close to the membrane interface. The slight change in the membrane shape does not affect the recovery of deeper structures so clinical studies concerning subcutaneous vessels, fat and muscle can effectively use the proposed model. Constructing forward TIR model for a particular membrane model is computationally time consuming and needs to be optimized. However, for clinical examination of skin surface and superficial vasculature, it is imperative that more flexible models are explored in the future which can adapt to the changes in membrane shape.

The slice thickness of an optoacoustic tomographic system can be measured as exhibited in this work, and this information would be helpful in the future for defining step size during multiple cross-sectional scans in y-axis for generating 3D reconstructions of clinical datasets. This slice thickness characterization method also paves the way for a verification method to evaluate impulse response correction in the elevation direction.

With the current implementation, it takes around 5 hours to compute a TIR model and it takes approximately 2.3GB of storage space in disc. The time required to compute the TIR model can be reduced by exploiting the symmetry of the array and parallelizing the SIR computation in Field-II using GPU acceleration. The LSQR method to obtain regularized solution was demonstrated in this work. The regularization parameters were chosen when the

change in the residual error is insignificant (for the case of very less noise in the reconstructed image). This choice can be made automated in the future by defining a suitable stopping criterion. The noise characterization presented may offer some insight in choosing a stopping criterion which can be taken up as a future extension of this work. Note that the forward model and inversion presented all throughout the work is in time domain. It is well known that the frequency domain reconstruction techniques enjoy faster computation exploiting efficiency of FFTs. A frequency domain approach to implement TIR correction can also be promising in terms of faster reconstruction. A combination of the aforementioned ideas can be used together with GPU acceleration to achieve real time inversion in the future.

Appendix A

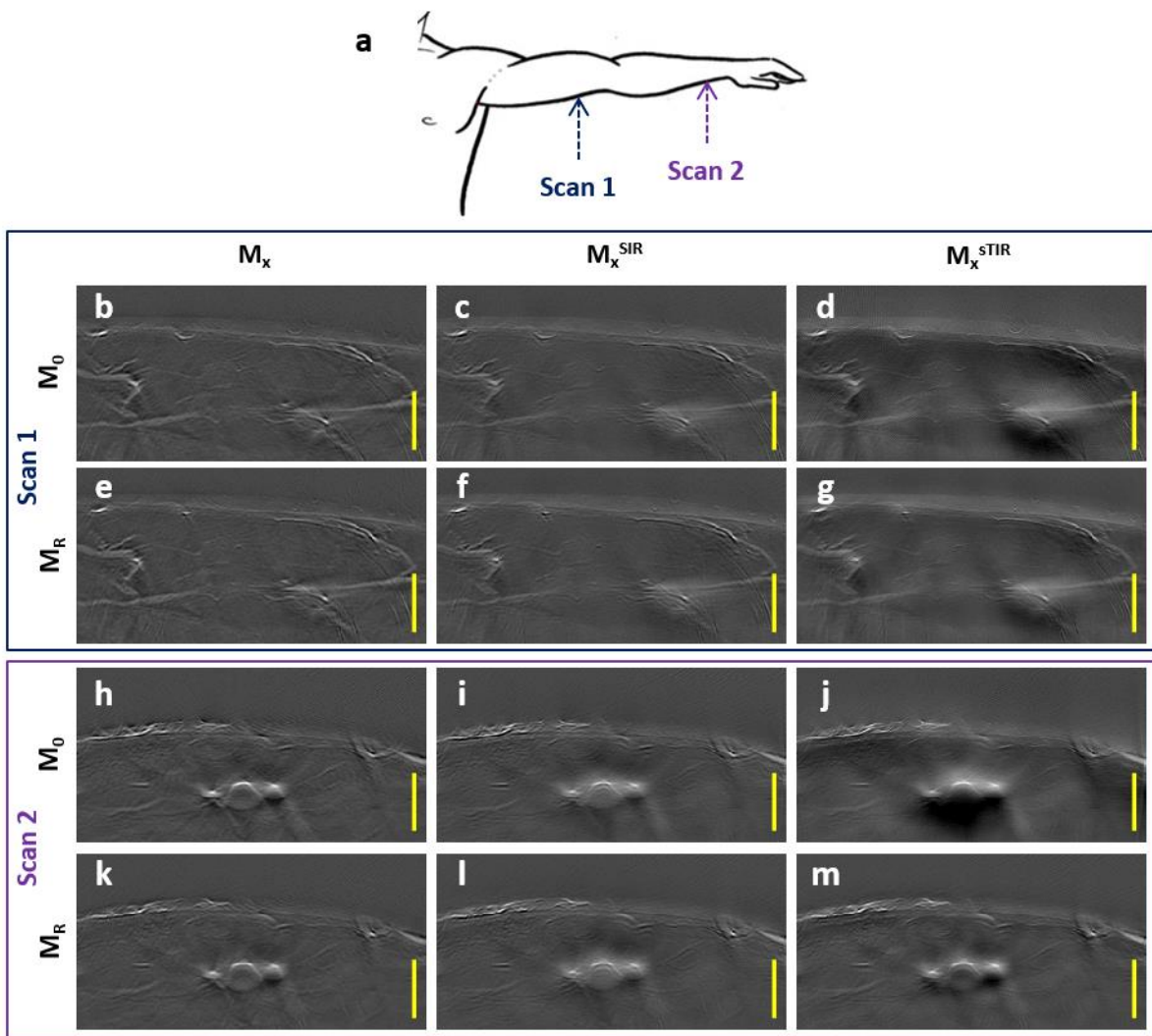


Figure A.1: Improved reconstruction of clinical datasets Scan 1 and Scan 2 through correcting for refraction and transducer properties. (a) Schematic of the scanning locations. (b-g) Images of the Scan 1 data reconstructed using the M_0 forward model (upper row) or M_R forward model (lower row) in the absence of transducer correction geometry (left column), with SIR correction (middle column) or sTIR correction (right column). (h-m) Images of the Scan 2 data reconstructed using the M_0 forward model (upper row) or M_R forward model (lower row) in the absence of transducer correction geometry (left column), with SIR correction (middle column) or sTIR correction (right column). Scale bar, 5 mm. (Source: Figure is adapted from supplementary document of [144], Copyright © 2020 IEEE)

Bibliography

- [1] J. H. Scatliff and P. J. Morris, "From Roentgen to magnetic resonance imaging: the history of medical imaging.," *N. C. Med. J.*, vol. 75, no. 2, pp. 111–113, 2014.
- [2] P. Balchandani and T.P. Naidich, "Ultra-High-Field MR Neuroimaging," *Am J Neuroradiol*, vol. 36, no. 7, pp. 1204–1215, 2015.
- [3] L. Fass, "Imaging and cancer: A review," *Mol. Oncol.*, vol. 2, no. 2, pp. 115–152, 2008.
- [4] R. L. Siegel, K. D. Miller, and A. Jemal, "Cancer statistics, 2020," *CA. Cancer J. Clin.*, vol. 70, no. 1, pp. 7–30, 2020.
- [5] M. L. James and S. S. Gambhir, "A molecular imaging primer: Modalities, imaging agents, and applications," *Physiol. Rev.*, vol. 92, no. 2, pp. 897–965, 2012.
- [6] L. V. Wang and S. Hu, "Photoacoustic tomography: In vivo imaging from organelles to organs," *Science (80-.)*, vol. 335, no. 6075, pp. 1458–1462, 2012.
- [7] V. Ntziachristos, J. Ripoll, L. V. Wang, and R. Weissleder, "Looking and listening to light: The evolution of whole-body photonic imaging," *Nat. Biotechnol.*, vol. 23, no. 3, pp. 313–320, 2005.
- [8] A. Taruttis and V. Ntziachristos, "Advances in real-time multispectral optoacoustic imaging and its applications," *Nat. Photonics*, vol. 9, no. 4, pp. 219–227, 2015.
- [9] M. Xu and L. V. Wang, "Photoacoustic imaging in biomedicine," *Rev. Sci. Instrum.*, vol. 77, no. 4, 2006.
- [10] P. K. Upputuri and M. Pramanik, "Recent advances toward preclinical and clinical translation of photoacoustic tomography: a review," *J. Biomed. Opt.*, vol. 22, no. 4, p. 041006, 2016.
- [11] S. Tainter and A. G. Bell, "SELENIUM AND THE PHOTOPHONE," *Nature*, vol. 23, no. Sept, pp. 500–503, 1880.
- [12] R. A. Kruger, "Photoacoustic ultrasound," *Med. Phys.*, vol. 21, no. 1, pp. 127–131, 1994.
- [13] A. A. Oraevsky, S. L. Jacques, and F. K. Tittel, "Measurement of tissue optical properties by time-resolved detection of laser-induced transient stress," *Appl. Opt.*, vol. 36, no. 1, p. 402, 1997.
- [14] R. A. Kruger, P. Liu, A. Y. R. Fang, and C. R. Appledorn, "Photoacoustic ultrasound_reconstruction tomography.pdf," *Am. Assoc. Phy Med*, 1995.
- [15] V. G. Andreev *et al.*, "Optoacoustic tomography of breast cancer with arc-array transducer," *Biomed. Optoacoustics*, vol. 3916, pp. 36–47, 2000.
- [16] L. V. Wang, "Tutorial on photoacoustic microscopy and computed tomography," *IEEE J. Sel. Top. Quantum Electron.*, vol. 14, no. 1, pp. 171–179, 2008.
- [17] A. Rosenthal, V. Ntziachristos, and D. Razansky, "Acoustic Inversion in Optoacoustic Tomography: A Review," *Curr. Med. Imaging Rev.*, vol. 9, no. 4, pp. 318–336, 2014.

- [18] G. Lu and B. Fei, “Medical hyperspectral imaging: a review,” *J. Biomed. Opt.*, vol. 19, no. 1, p. 010901, 2014.
- [19] B. T. Cox, S. R. Arridge, and P. C. Beard, “Estimating chromophore distributions from multiwavelength photoacoustic images,” *J. Opt. Soc. Am. A*, vol. 26, no. 2, p. 443, 2009.
- [20] V. Ntziachristos and D. Razansky, “Molecular imaging by means of multispectral optoacoustic tomography (MSOT),” *Chem. Rev.*, vol. 110, no. 5, pp. 2783–2794, 2010.
- [21] B. Cox, J. G. Laufer, S. R. Arridge, and P. C. Beard, “Quantitative spectroscopic photoacoustic imaging: a review,” *J. Biomed. Opt.*, vol. 17, no. 6, p. 061202, 2012.
- [22] Z. Guo, L. Li, and L. V. Wang, “On the speckle-free nature of photoacoustic tomography,” *Med. Phys.*, vol. 36, no. 9, pp. 4084–4088, 2009.
- [23] I. Steinberg, D. M. Huland, O. Vermesh, H. E. Frostig, W. S. Tummers, and S. S. Gambhir, “Photoacoustic clinical imaging,” *Photoacoustics*, vol. 14, no. May, pp. 77–98, 2019.
- [24] M. Heijblom, W. Steenbergen, and S. Manohar, “Clinical photoacoustic breast imaging: The twente experience,” *IEEE Pulse*, vol. 6, no. 3, pp. 42–46, 2015.
- [25] W. Choi, E. Y. Park, S. Jeon, and C. Kim, “Clinical photoacoustic imaging platforms,” *Biomed. Eng. Lett.*, vol. 8, no. 2, pp. 139–155, 2018.
- [26] S. Mallidi, G. P. Luke, and S. Emelianov, “Photoacoustic imaging in cancer detection, diagnosis, and treatment guidance,” *Trends Biotechnol.*, vol. 29, no. 5, pp. 213–221, 2011.
- [27] K. S. Valluru and J. K. Willmann, “Clinical photoacoustic imaging of cancer,” *Ultrasonography*, vol. 35, no. 4, pp. 267–280, 2016.
- [28] D. Hanahan and R. A. Weinberg, “Hallmarks of cancer: The next generation,” *Cell*, vol. 144, no. 5, pp. 646–674, 2011.
- [29] Q. Shao, E. Morgounova, C. Jiang, J. Choi, J. Bischof, and S. Ashkenazi, “In vivo photoacoustic lifetime imaging of tumor hypoxia in small animals,” *J. Biomed. Opt.*, vol. 18, no. 7, p. 076019, 2013.
- [30] M. Gerling *et al.*, “Real-time assessment of tissue hypoxia In Vivo with combined photoacoustics and high-frequency ultrasound,” *Theranostics*, vol. 4, no. 6, pp. 604–613, 2014.
- [31] G. Diot *et al.*, “Multispectral Optoacoustic Tomography (MSOT) of human breast cancer,” *Clin. Cancer Res.*, vol. 23, no. 22, pp. 6912–6922, 2017.
- [32] S. A. Ermilov *et al.*, “Laser optoacoustic imaging system for detection of breast cancer,” *J. Biomed. Opt.*, vol. 14, no. 2, p. 024007, 2009.
- [33] R. A. Kruger, C. M. Kuzmiak, R. B. Lam, D. R. Reinecke, S. P. Del Rio, and D. Steed, “Dedicated 3D photoacoustic breast imaging,” *Med. Phys.*, vol. 40, no. 11, 2013.
- [34] T. Kitai *et al.*, “Photoacoustic mammography: Initial clinical results,” *Breast Cancer*, vol. 21, no. 2, pp. 146–153, 2014.
- [35] M. Heijblom *et al.*, “The state of the art in breast imaging using the Twente Photoacoustic Mammoscope: results from 31 measurements on malignancies,” *Eur.*

Radiol., vol. 26, no. 11, pp. 3874–3887, 2016.

- [36] Y. Zhou, G. Li, L. Zhu, C. Li, L. A. Cornelius, and L. V. Wang, “Handheld photoacoustic probe to detect both melanoma depth and volume at high speed in vivo,” *J. Biophotonics*, vol. 8, no. 11–12, pp. 961–967, 2015.
- [37] C. P. Favazza, O. Jassim, L. A. Cornelius, and L. V. Wang, “In vivo photoacoustic microscopy of human cutaneous microvasculature and a nevus,” *J. Biomed. Opt.*, vol. 16, no. 1, p. 016015, 2011.
- [38] V. S. Dogra *et al.*, “Preliminary results of ex vivo multispectral photoacoustic imaging in the management of thyroid cancer,” *Am. J. Roentgenol.*, vol. 202, no. 6, pp. 552–558, 2014.
- [39] V. Dogra *et al.*, “Multispectral photoacoustic imaging of prostate cancer: Preliminary ex-vivo results,” *J. Clin. Imaging Sci.*, vol. 3, no. 1, pp. 1–7, 2013.
- [40] A. Aguirre, Y. Ardeshirpour, M. M. Sanders, M. Brewer, and Q. Zhu, “Potential role of coregistered photoacoustic and ultrasound imaging in ovarian cancer detection and characterization,” *Transl. Oncol.*, vol. 4, no. 1, pp. 29–37, 2011.
- [41] J. Weber, P. C. Beard, and S. E. Bohndiek, “Contrast agents for molecular photoacoustic imaging,” *Nat. Methods*, vol. 13, no. 8, pp. 639–650, 2016.
- [42] A. De La Zerda *et al.*, “Carbon nanotubes as photoacoustic molecular imaging agents in living mice,” *Nat. Nanotechnol.*, vol. 3, no. 9, pp. 557–562, 2008.
- [43] G. P. Luke, D. Yeager, and S. Y. Emelianov, “Biomedical applications of photoacoustic imaging with exogenous contrast agents,” *Ann. Biomed. Eng.*, vol. 40, no. 2, pp. 422–437, 2012.
- [44] D. Razansky *et al.*, “Multispectral opto-acoustic tomography of deep-seated fluorescent proteins in vivo,” *Nat. Photonics*, vol. 3, no. 7, pp. 412–417, 2009.
- [45] B. Wang *et al.*, “Plasmonic intravascular photoacoustic imaging for detection of macrophages in atherosclerotic plaques,” *Nano Lett.*, vol. 9, no. 6, pp. 2212–2217, 2009.
- [46] B. Wang *et al.*, “Intravascular photoacoustic imaging of lipid in atherosclerotic plaques in the presence of luminal blood,” *Opt. Lett.*, vol. 37, no. 7, p. 1244, 2012.
- [47] Y. Sun, E. S. Sobel, and H. Jiang, “First assessment of three-dimensional quantitative photoacoustic tomography for in vivo detection of osteoarthritis in the finger joints,” *Med. Phys.*, vol. 38, no. 7, pp. 4009–4017, 2011.
- [48] J. Jo *et al.*, “Photoacoustic tomography for human musculoskeletal imaging and inflammatory arthritis detection,” *Photoacoustics*, vol. 12, no. July, pp. 82–89, 2018.
- [49] M. W. Schellenberg and H. K. Hunt, “Hand-held optoacoustic imaging: A review,” *Photoacoustics*, vol. 11, no. February, pp. 14–27, 2018.
- [50] K. Sivasubramanian, V. Periyasamy, K. K. Wen, and M. Pramanik, “Optimizing light delivery through fiber bundle in photoacoustic imaging with clinical ultrasound system: Monte Carlo simulation and experimental validation,” *J. Biomed. Opt.*, vol. 22, no. 4, p. 041008, 2016.
- [51] S. Liu *et al.*, “Handheld Photoacoustic Imager for Theranostics in 3D,” *IEEE Trans. Med. Imaging*, vol. 38, no. 9, pp. 2037–2046, 2019.

- [52] C. Kim, T. N. Erpelding, L. Jankovic, M. D. Pashley, and L. V. Wang, “Deeply penetrating in vivo photoacoustic imaging using a clinical ultrasound array system,” *Biomed. Opt. Express*, vol. 1, no. 1, p. 278, 2010.
- [53] A. Garcia-Urbe *et al.*, “Dual-Modality photoacoustic and ultrasound imaging system for noninvasive sentinel lymph node detection in patients with breast cancer,” *Sci. Rep.*, vol. 5, no. April, pp. 1–8, 2015.
- [54] J. Yuan *et al.*, “Real-time photoacoustic and ultrasound dual-modality imaging system facilitated with graphics processing unit and code parallel optimization,” *J. Biomed. Opt.*, vol. 18, no. 08, p. 1, 2013.
- [55] K. Daoudi *et al.*, “Handheld probe integrating laser diode and ultrasound transducer array for ultrasound/photoacoustic dual modality imaging,” *Opt. Express*, vol. 22, no. 21, p. 26365, 2014.
- [56] P. K. Upputuri and M. Pramanik, “Performance characterization of low-cost, high-speed, portable pulsed laser diode photoacoustic tomography (PLD-PAT) system,” *Biomed. Opt. Express*, vol. 6, no. 10, p. 4118, 2015.
- [57] J. Kim *et al.*, “Programmable Real-time Clinical Photoacoustic and Ultrasound Imaging System,” *Sci. Rep.*, vol. 6, no. April, pp. 1–11, 2016.
- [58] X. L. Deán-Ben and D. Razansky, “Portable spherical array probe for volumetric real-time optoacoustic imaging at centimeter-scale depths,” *Opt. Express*, vol. 21, no. 23, p. 28062, 2013.
- [59] A. Buehler, M. Kacprowicz, A. Taruttis, and V. Ntziachristos, “Real-time handheld multispectral optoacoustic imaging,” *Opt. Lett.*, vol. 38, no. 9, p. 1404, 2013.
- [60] G. Diot, A. Dima, and V. Ntziachristos, “Multispectral opto-acoustic tomography of exercised muscle oxygenation,” *Opt. Lett.*, vol. 40, no. 7, p. 1496, 2015.
- [61] P. Hai *et al.*, “Label-free high-throughput detection and quantification of circulating melanoma tumor cell clusters by linear-array-based photoacoustic tomography,” *J. Biomed. Opt.*, vol. 22, no. 04, p. 1, 2016.
- [62] S. A. Ermilov *et al.*, “Development of laser optoacoustic and ultrasonic imaging system for breast cancer utilizing handheld array probes,” vol. 717703, no. February 2009, p. 717703, 2009.
- [63] A. Becker *et al.*, “Multispectral optoacoustic tomography of the human breast : characterisation of healthy tissue and malignant lesions using a hybrid ultrasound-optoacoustic approach,” 2017.
- [64] A. Dima and V. Ntziachristos, “In-vivo handheld optoacoustic tomography of the human thyroid,” *Photoacoustics*, vol. 4, no. 2, pp. 65–69, 2016.
- [65] M. E. N. G. Y. Ang *et al.*, “Photoacoustic / ultrasound dual imaging of human thyroid cancers : an initial clinical study,” vol. 8, no. 7, pp. 3449–3457, 2017.
- [66] H. Yang *et al.*, “Soft ultrasound priors in optoacoustic reconstruction: Improving clinical vascular imaging,” *Photoacoustics*, vol. 19, no. February, p. 100172, 2020.
- [67] A. Karlas *et al.*, “Flow-mediated dilatation test using optoacoustic imaging: a proof-of-concept,” *Biomed. Opt. Express*, vol. 8, no. 7, p. 3395, 2017.
- [68] A. Karlas *et al.*, “Multispectral optoacoustic tomography of muscle perfusion and

- oxygenation under arterial and venous occlusion: A human pilot study,” *J. Biophotonics*, vol. 13, no. 6, pp. 1–9, 2020.
- [69] I. Stoffels *et al.*, “Metastatic status of sentinel lymph nodes in melanoma determined noninvasively with multispectral optoacoustic imaging,” vol. 7, no. 317, 2015.
- [70] Y. Zhou, C. Sc, J. Se, W. Sterry, E. Stockfleth, and A. S. Reflectance, “Noninvasive Determination of Melanoma Depth using a Handheld Photoacoustic Probe,” vol. 137, pp. 1370–1372, 2017.
- [71] Y. Zhou, G. Li, L. Zhu, C. Li, L. A. Cornelius, and L. V. Wang, “Handheld photoacoustic probe to detect both melanoma depth and volume at high speed in vivo,” *J. Biophotonics*, vol. 8, no. 11–12, pp. 961–967, 2015.
- [72] F. Knieling, C. Neufert, A. Hartmann, C. Jing, U. Alexander, and M. J. Waldner, “Multispectral Optoacoustic Tomography for Assessment of Crohn’s Disease Activity,” *N. Engl. J. Med.*, no. March, pp. 1747–1751, 2017.
- [73] P. Burgholzer, G. J. Matt, M. Haltmeier, and G. Paltauf, “Exact and approximative imaging methods for photoacoustic tomography using an arbitrary detection surface,” *Phys. Rev. E - Stat. Nonlinear, Soft Matter Phys.*, vol. 75, no. 4, pp. 1–10, 2007.
- [74] K. Wang, S. Ermilov, R. Su, H.-P. Brecht, A. Oraevsky, and M. Anastasio, “An imaging model incorporating ultrasonic transducer properties for three-dimensional optoacoustic tomography,” *IEEE Trans. Med. Imaging*, vol. 30, no. 2, pp. 203–214, 2011.
- [75] G. Paltauf, P. R. Torke, and R. Nuster, “Modeling photoacoustic imaging with a scanning focused detector using Monte Carlo simulation of energy deposition,” *J. Biomed. Opt.*, vol. 18, no. 3, pp. 035001–7, 2018.
- [76] C. Huang, K. Wang, L. Nie, L. V. Wang, and M. A. Anastasio, “Full-wave iterative image reconstruction in photoacoustic tomography with acoustically inhomogeneous media,” *IEEE Trans. Med. Imaging*, vol. 32, no. 6, pp. 1097–1110, 2013.
- [77] S. Bu *et al.*, “Model-based reconstruction integrated with fluence compensation for photoacoustic tomography,” *IEEE Trans. Biomed. Eng.*, vol. 59, no. 5, pp. 1354–1363, 2012.
- [78] T. Berer, I. A. Veres, H. Grün, J. Bauer-Marschallinger, K. Felbermayer, and P. Burgholzer, “Characterization of broadband fiber optic line detectors for photoacoustic tomography,” *J. Biophotonics*, vol. 5, no. 7, pp. 518–528, 2012.
- [79] J. Zhang, M. A. Anastasio, P. J. La Rivière, and L. V. Wang, “Effects of different imaging models on least-squares image reconstruction accuracy in photoacoustic tomography,” *IEEE Trans. Med. Imaging*, vol. 28, no. 11, pp. 1781–1790, 2009.
- [80] B. T. Cox, S. R. Arridge, and P. C. Beard, “Photoacoustic tomography with a limited-aperture planar sensor and a reverberant cavity,” *Inverse Probl.*, vol. 23, no. 6, 2007.
- [81] A. Rosenthal, V. Ntziachristos, and D. Razansky, “Model-based optoacoustic inversion with arbitrary-shape detectors,” *Med. Phys.*, vol. 38, no. 7, pp. 4285–4295, 2011.
- [82] M. W. Kim, G. S. Jeng, M. O’Donnell, and I. Pelivanov, “Correction of wavelength-dependent laser fluence in swept-beam spectroscopic photoacoustic imaging with a hand-held probe,” *Photoacoustics*, vol. 19, no. January, p. 100192, 2020.

- [83] L. Ulrich *et al.*, “Spectral correction for handheld optoacoustic imaging by means of near-infrared optical tomography in reflection mode,” *J. Biophotonics*, vol. 12, no. 1, pp. 1–16, 2019.
- [84] B. E. Treeby, “Acoustic attenuation compensation in photoacoustic tomography using time-variant filtering,” *J. Biomed. Opt.*, vol. 18, no. 3, p. 036008, 2013.
- [85] G. F. Pinton, J. Dahl, S. Rosenzweig, and G. E. Trahey, “A heterogeneous nonlinear attenuating full-wave model of ultrasound,” *IEEE Trans. Ultrason. Ferroelectr. Freq. Control*, vol. 56, no. 3, pp. 474–488, 2009.
- [86] J. Friel and E. T. Quinto, “Artifacts in Incomplete Data Tomography with Applications to Photoacoustic Tomography and Sonar,” *SIAM J. APPL. MATH*, vol. 75, no. 2, pp. 703–725, 2015.
- [87] L. Yao and H. Jiang, “Photoacoustic image reconstruction from few-detector and limited-angle data,” *Biomed. Opt. Express*, vol. 2, no. 9, p. 2649, 2011.
- [88] M. Xu and L. V. Wang, “Analytic explanation of spatial resolution related to bandwidth and detector aperture size in thermoacoustic or photoacoustic reconstruction,” *Phys. Rev. E - Stat. Physics, Plasmas, Fluids, Relat. Interdiscip. Top.*, vol. 67, no. 5, p. 15, 2003.
- [89] T. D. Khokhlova, I. M. Pelivanov, and A. A. Karabutov, “Optoacoustic tomography utilizing focused transducers: The resolution study,” *Appl. Phys. Lett.*, vol. 92, no. 2, pp. 2006–2009, 2008.
- [90] M. Haltmeier and G. Zangerl, “Spatial resolution in photoacoustic tomography: Effects of detector size and detector bandwidth,” *Inverse Probl.*, vol. 26, no. 12, 2010.
- [91] B. G. Tomov, S. E. Diederichsen, E. Thomsen, and J. A. Jensen, “Characterization of Medical Ultrasound Transducers,” *IEEE Int. Ultrason. Symp. IUS*, vol. 2018-October, pp. 3–6, 2018.
- [92] X. L. Deán-Ben, A. Özbek, and D. Razansky, “Accounting for speed of sound variations in volumetric hand-held optoacoustic imaging,” *Front. Optoelectron.*, vol. 10, no. 3, pp. 280–286, 2017.
- [93] M. A. A. Caballero, A. Rosenthal, A. Buehler, D. Razansky, and V. Ntziachristos, “Optoacoustic determination of spatio-temporal responses of ultrasound sensors,” *IEEE Trans. Ultrason. Ferroelectr. Freq. Control*, vol. 60, no. 6, pp. 1234–1244, 2013.
- [94] K. Wang, R. Su, A. A. Oraevsky, and M. A. Anastasio, “Investigation of iterative image reconstruction in three-dimensional optoacoustic tomography,” *Phys. Med. Biol.*, vol. 57, no. 17, pp. 5399–5423, 2012.
- [95] A. Karlas *et al.*, “Cardiovascular optoacoustics: From mice to men – A review,” *Photoacoustics*, vol. 14, no. March, pp. 19–30, 2019.
- [96] B. T. Cox, S. Kara, S. R. Arridge, and P. C. Beard, “k-space propagation models for acoustically heterogeneous media: Application to biomedical photoacoustics,” *J. Acoust. Soc. Am.*, vol. 121, no. 6, p. 3453, 2007.
- [97] A. Rosenthal, D. Razansky, and V. Ntziachristos, “Fast semi-analytical model-based acoustic inversion for quantitative optoacoustic tomography,” *IEEE Trans. Med. Imaging*, vol. 29, no. 6, pp. 1275–1285, 2010.

- [98] X. L. Deán-Ben, V. Ntziachristos, and D. Razansky, “Acceleration of optoacoustic model-based reconstruction using angular image discretization,” *IEEE Trans. Med. Imaging*, vol. 31, no. 5, pp. 1154–1162, 2012.
- [99] J. Prakash, A. S. Raju, C. B. Shaw, M. Pramanik, and P. K. Yalavarthy, “Basis pursuit deconvolution for improving model-based reconstructed images in photoacoustic tomography,” *Biomed. Opt. Express*, vol. 5, no. 5, p. 1363, 2014.
- [100] G. J. Diebold, T. Sun, and M. I. Khan, “Photoacoustic monopole radiation in one, two, and three dimensions,” *Phys. Rev. Lett.*, vol. 67, no. 24, pp. 3384–3387, 1991.
- [101] C. G. A. Hoelen, F. F. M. de Mul, R. Pongers, and A. Dekker, “Three-dimensional photoacoustic imaging of blood vessels in tissue,” *Opt. Lett.*, vol. 23, no. 8, p. 648, 1998.
- [102] M. Xu and L. V. Wang, “Universal back-projection algorithm for photoacoustic computed tomography,” *Phys. Rev. E - Stat. Nonlinear, Soft Matter Phys.*, vol. 71, no. 1, pp. 1–7, 2005.
- [103] G. Paltauf, J. A. Viator, S. A. Prahl, and S. L. Jacques, “Iterative reconstruction algorithm for optoacoustic imaging,” *J. Acoust. Soc. Am.*, vol. 112, no. 4, pp. 1536–1544, 2002.
- [104] C. B. Shaw, J. Prakash, M. Pramanik, and P. K. Yalavarthy, “Least squares QR-based decomposition provides an efficient way of computing optimal regularization parameter in photoacoustic tomography,” *J. Biomed. Opt.*, vol. 18, no. 8, p. 080501, 2013.
- [105] D. Van De Sompel, L. S. Sasportas, J. V. Jokerst, and S. S. Gambhir, “Comparison of deconvolution filters for photoacoustic tomography,” *PLoS One*, vol. 11, no. 3, pp. 1–28, 2016.
- [106] M. Á. Araque Caballero, A. Rosenthal, J. Gateau, D. Razansky, and V. Ntziachristos, “Model-based optoacoustic imaging using focused detector scanning,” *Opt. Lett.*, vol. 37, no. 19, p. 4080, 2012.
- [107] A. Rosenthal, V. Ntziachristos, and D. Razansky, “Optoacoustic methods for frequency calibration of ultrasonic sensors,” *IEEE Trans. Ultrason. Ferroelectr. Freq. Control*, vol. 58, no. 2, pp. 316–326, 2011.
- [108] J. Kim, J. Y. Kim, S. Jeon, J. W. BAIK, S. H. Cho, and C. Kim, “Super-resolution localization photoacoustic microscopy using intrinsic red blood cells as contrast absorbers,” *Light Sci. Appl.*, vol. 8, no. 1, p. 103, 2019.
- [109] Y. Han, L. Ding, X. L. D. Ben, D. Razansky, J. Prakash, and V. Ntziachristos, “Three-dimensional optoacoustic reconstruction using fast sparse representation,” *Opt. Lett.*, vol. 42, no. 5, p. 979, 2017.
- [110] J. Prakash, S. Mandal, D. Razansky, and V. Ntziachristos, “Maximum Entropy Based Non-Negative Optoacoustic Tomographic Image Reconstruction,” *IEEE Trans. Biomed. Eng.*, vol. 66, no. 9, pp. 2604–2616, 2019.
- [111] G. E. Tupholme, “Generation of acoustic pulses by baffled plane pistons,” *Mathematika*, vol. 16, no. 2, pp. 209–224, 1969.
- [112] P. R. Stepanishen, “The Time-Dependent Force and Radiation Impedance on a Piston in a Rigid Infinite Planar Baffle,” *J. Acoust. Soc. Am.*, vol. 49, no. 3, pp. 841–849,

- 1971.
- [113] A. Jensen, “Calculation of Pressure Fields from Arbitrarily Shaped, Apodized, and Excited Ultrasound Transducers,” vol. 39, no. 2, pp. 262–267, 1992.
 - [114] J. A. Jensen, “A New approach to calculating spatial impulse responses,” *Proc. IEEE Ultrason. Symp.*, vol. 2, pp. 1755–1759, 1997.
 - [115] J. A. Jensen, “FIELD: A Program for Simulating Ultrasound Systems,” *Med. Biol. Eng. Comput.*, vol. 34, no. SUPPL. 1, pp. 351–352, 1996.
 - [116] T. L. Szabo, *Diagnostic Ultrasound Imaging: Inside Out*. 2014.
 - [117] K. K. Shung and M. J. Zipparo, “Ultrasonic transducers and arrays,” *IEEE Eng. Med. Biol. Mag.*, vol. 15, no. 6, pp. 20–30, 1996.
 - [118] G. S. Kino, *Acoustic Waves: Devices, Imaging, and Analog Signal Processing*, vol. 100. 1987.
 - [119] W. P. Mason, *Physical Acoustics, Volume 1-*. Academic Press, 1964.
 - [120] M. Redwood, “Transient Performance of a Piezoelectric Transducer,” *J. Acoust. Soc. Am.*, vol. 33, no. 4, pp. 527–536, 1961.
 - [121] D. A. Leedom, R. S. Krimholtz, and G. L. Matthaei, “Equivalent Circuits for Transducers Having Arbitrary Asymmetrical Piezoelectric Excitation,” *IEEE Trans. Sonics Ultrason.*, vol. 19, no. 4, pp. 427–435, 1972.
 - [122] L. V. Wang and J. Yao, “A practical guide to photoacoustic tomography in the life sciences,” *Nat. Methods*, vol. 13, no. 8, pp. 627–638, 2016.
 - [123] E. B. Miller and D. G. Eitzen, “Ultrasonic Transducer Characterization at the NBS,” *IEEE Trans. Sonics Ultrason.*, vol. 26, no. 1, pp. 28–36, 1979.
 - [124] J. A. Jensen and M. F. Rasmussen, “Safety assessment of advanced imaging sequences I: Measurements,” *IEEE Trans. Ultrason. Ferroelectr. Freq. Control*, vol. 63, no. 1, pp. 120–127, 2016.
 - [125] T. Marhenke, S. J. Sanabria, B. R. Chintada, R. Furrer, J. Neuenschwander, and O. Goksel, “Acoustic field characterization of medical array transducers based on unfocused transmits and single-plane hydrophone measurements,” *Sensors (Switzerland)*, vol. 19, no. 4, pp. 1–17, 2019.
 - [126] J. Gu and Y. Jing, “Modeling of wave propagation for medical ultrasound: A review,” *IEEE Trans. Ultrason. Ferroelectr. Freq. Control*, vol. 62, no. 11, pp. 1979–1993, 2015.
 - [127] R. J. Bobber, “General Reciprocity Parameter,” vol. 39, no. 4, pp. 680–687, 1966.
 - [128] D. Cassereau, D. Guyomar, and M. Fink, “Time deconvolution of diffraction effects—Application to calibration and prediction of transducer waveforms,” *J. Acoust. Soc. Am.*, vol. 84, no. 3, pp. 1073–1085, 1988.
 - [129] A. L. Lopez-Sanchez and L. W. Schmerr, “Determination of an ultrasonic transducer’s sensitivity and impedance in a pulse-echo setup,” *IEEE Trans. Ultrason. Ferroelectr. Freq. Control*, vol. 53, no. 11, pp. 2101–2112, 2006.
 - [130] G. R. Harris, “Hydrophone Measurements In Diagnostic Ultrasound Fields,” *IEEE*

- Trans. Ultrason. Ferroelectr. Freq. Control*, vol. 35, no. 2, pp. 87–101, 1988.
- [131] N. Felix, D. Certon, L. Ratsimandresy, M. Lethiecq, and F. Patat, “1D ultrasound array: Performances evaluation and characterization by laser interferometry,” *Proc. IEEE Ultrason. Symp.*, vol. 2, pp. 1191–1194, 2000.
- [132] B. E. Treeby, J. Jaros, A. P. Rendell, and B. T. Cox, “Modeling nonlinear ultrasound propagation in heterogeneous media with power law absorption using a k -space pseudospectral method,” *J. Acoust. Soc. Am.*, vol. 131, no. 6, pp. 4324–4336, 2012.
- [133] L. W. Schmerr, A. Lopez-Sanchez, and R. Huang, “Complete ultrasonic transducer characterization and its use for models and measurements,” *Ultrasonics*, vol. 44, no. SUPPL., pp. 753–757, 2006.
- [134] K. R. Erikson, “Tone-Burst Testing of Pulse-Echo Transducers,” no. 1, pp. 7–14, 1979.
- [135] D. H. Turnbull and F. Stuart Foster, “Fabrication and characterization of transducer elements in two-dimensional arrays for medical Ultrasound imaging,” *Proc. - IEEE Ultrason. Symp.*, vol. 39, no. 4, pp. 629–632, 1991.
- [136] J. Rebling, O. Warshavski, C. Meynier, and D. Razansky, “Optoacoustic characterization of broadband directivity patterns of capacitive micromachined ultrasonic transducers,” *J. Biomed. Opt.*, vol. 22, no. 4, p. 041005, 2016.
- [137] V. Periyasamy and M. Pramanik, “Monte Carlo simulation of light transport in turbid medium with embedded object—spherical, cylindrical, ellipsoidal, or cuboidal objects embedded within multilayered tissues,” *J. Biomed. Opt.*, vol. 19, no. 4, p. 045003, 2014.
- [138] G. S. Sangha, N. J. Hale, and C. J. Goergen, “Adjustable photoacoustic tomography probe improves light delivery and image quality,” *Photoacoustics*, vol. 12, no. April, pp. 6–13, 2018.
- [139] A. M. Winkler, K. Maslov, and L. V. Wang, “Noise-equivalent sensitivity of photoacoustics,” *J. Biomed. Opt.*, vol. 18, no. 9, p. 097003, 2013.
- [140] E. R. Hill, W. Xia, M. J. Clarkson, and A. E. Desjardins, “Identification and removal of laser-induced noise in photoacoustic imaging using singular value decomposition,” *Biomed. Opt. Express*, vol. 8, no. 1, p. 68, 2017.
- [141] G. Wissmeyer, M. A. Pleitez, A. Rosenthal, and V. Ntziachristos, “Looking at sound: optoacoustics with all-optical ultrasound detection,” *Light Sci. Appl.*, vol. 7, no. 1, 2018.
- [142] V. G. Andreev, A. A. Karabutov, A. E. Ponomaryov, and A. A. Oraevsky, “Detection of optoacoustic transients with a rectangular transducer of finite dimensions,” 2017.
- [143] K. Wang, S. A. Ermilov, R. Su, H.-P. Brecht, A. A. Oraevsky, and M. A. Anastasio, “Imaging Model Incorporating Ultrasonic Transducer Properties for Three-Dimensional Optoacoustic Tomography,” *IEEE Trans. Med. Imaging*, vol. 30, no. 2, pp. 203–214, 2011.
- [144] K. B. Chowdhury, J. Prakash, A. Karlas, D. Justel, and V. Ntziachristos, “A Synthetic Total Impulse Response Characterization Method for Correction of Hand-Held Optoacoustic Images,” *IEEE Trans. Med. Imaging*, vol. 39, no. 10, pp. 3218–3230, 2020.

- [145] N. A. Rejesh, H. Pullagurra, and M. Pramanik, “Deconvolution-based deblurring of reconstructed images in photoacoustic/thermoacoustic tomography,” *J. Opt. Soc. Am. A*, vol. 30, no. 10, p. 1994, 2013.
- [146] K. Mitsuhashi, K. Wang, and M. A. Anastasio, “Investigation of the far-field approximation for modeling a transducer’s spatial impulse response in photoacoustic computed tomography,” *Photoacoustics*, vol. 2, no. 1, pp. 21–32, 2014.
- [147] M.-L. Li, Y.-C. Tseng, and C.-C. Cheng, “Model-based correction of finite aperture effect in photoacoustic tomography,” *Opt. Express*, vol. 18, no. 25, pp. 26285–26292, 2010.
- [148] V. Neuschmelting *et al.*, “Performance of a Multispectral Optoacoustic Tomography (MSOT) System equipped with 2D vs. 3D Handheld Probes for Potential Clinical Translation,” *Photoacoustics*, vol. 4, no. 1, pp. 1–10, 2016.
- [149] A. Buehler, G. Diot, T. Volz, J. Kohlmeyer, and V. Ntziachristos, “Imaging of fatty tumors: appearance of subcutaneous lipomas in optoacoustic images,” *J. Biophotonics*, vol. 10, no. 8, pp. 983–989, 2017.
- [150] G. E. Forsythe, M. A. Malcolm, and C. B. Moler, “Computer methods for mathematical computations,” *Englewood Cliffs by Prentice-Hall*, 1976.
- [151] R. P. Brent, *Algorithms for Minimization without Derivatives*. 1973.
- [152] B. V. R. Rao, “Dispersion of Sound Velocity in Liquids,” *Nature*, no. May, p. 885, 1937.
- [153] Y. Levy, Y. Agnon, and H. Azhari, “Measurement of speed of sound dispersion in soft tissues using a double frequency continuous wave method,” *Ultrasound Med. Biol.*, vol. 32, no. 7, pp. 1065–1071, 2006.
- [154] M. D. Verweij, B. E. Treeby, K. W. A. van Dongen, and L. Demi, *Simulation of Ultrasound Fields*, vol. 2. 2014.
- [155] W. D. Wilson, “Speed of Sound in Heavy Water as a Function of Temperature and Pressure,” *J. Acoust. Soc. Am.*, vol. 31, no. 8, pp. 1067–1072, 1959.
- [156] R. C. Chivers and R. J. Parry, “Ultrasonic velocity and attenuation in mammalian tissues,” *J. Acoust. Soc. Am.*, vol. 63, no. 3, pp. 940–953, 1978.
- [157] J. Prakash and P. K. Yalavarthy, “A LSQR-type method provides a computationally efficient automated optimal choice of regularization parameter in diffuse optical tomography,” *Med. Phys.*, vol. 40, no. 3, 2013.
- [158] Z. Wang, A. C. Bovik, H. R. Sheikh, and S. Eero, “Image Quality Assessment: From Error Visibility to Structural Similarity,” *IEEE Trans. IMAGE Process.*, vol. 13, no. 4, pp. 600–612, 2004.
- [159] S. L. Jacques, “Optical properties of biological tissues: A review,” *Phys. Med. Biol.*, vol. 58, no. 14, pp. 5007–5008, 2013.
- [160] J. S. Pober and W. C. Sessa, “Inflammation and the blood microvascular system,” *Cold Spring Harb. Perspect. Biol.*, vol. 7, no. 1, pp. 1–12, 2015.
- [161] M. J. Fowler, “Microvascular and macrovascular complications of diabetes... 6th in a 12-part series,” *Diabetic*, vol. 26, no. 2, pp. 77–82, 2008.

- [162] D. Queirós, X. L. Déan-Ben, A. Buehler, D. Razansky, A. Rosenthal, and V. Ntziachristos, “Modeling the shape of cylindrically focused transducers in three-dimensional optoacoustic tomography,” *Photons Plus Ultrasound Imaging Sens. 2014*, vol. 8943, p. 89432F, 2014.
- [163] J. A. Jensen, “Safety assessment of advanced imaging sequences II: Simulations,” *IEEE Trans. Ultrason. Ferroelectr. Freq. Control*, vol. 63, no. 1, pp. 120–127, 2016.
- [164] A. Aldroub and M. Unser, “Sampling procedures in function spaces and asymptotic equivalence with shannon’s sampling theory,” *Numer. Funct. Anal. Optim.*, vol. 15, no. 1–2, pp. 1–21, 1994.
- [165] A. Aldroubi and K. Gröchenig, “Nonuniform sampling and reconstruction in shift-invariant spaces,” *SIAM Rev.*, vol. 43, no. 4, pp. 585–620, 2001.
- [166] L. Ding, X. Luís Déan-Ben, C. Lutzweiler, D. Razansky, and V. Ntziachristos, “Efficient non-negative constrained model-based inversion in optoacoustic tomography,” *Phys. Med. Biol.*, vol. 60, no. 17, pp. 6733–6750, 2015.
- [167] C. P. Hansen, “Regularization Tools A Matlab Package for Analysis and Solution of Discrete Ill-Posed Problems Version 4.1 for Matlab 7.3,” vol. 6, no. March, pp. 1–35, 2008.
- [168] Å. Björck, “A bidiagonalization algorithm for solving large and sparse ill-posed systems of linear equations,” *Bit*, vol. 28, no. 3, pp. 659–670, 1988.
- [169] J. A. Simmons, “A bidiagonalization-regularization procedure for large scale discretizations of ill-posed problems,” *SIAM J. SCI. STAT. Comput.*, vol. 2, no. 4, pp. 474–489, 1981.
- [170] M. E. Kilmer, “CHOOSING REGULARIZATION PARAMETERS IN ITERATIVE METHODS FOR ILL-POSED PROBLEMS,” *SIAM J. MATRIX ANAL. APPL.*, vol. 22, no. 4, pp. 1204–1221, 2001.
- [171] C. C. Paige and M. A. Saunders, “LSQR: An Algorithm for Sparse Linear Equations and Sparse Least Squares,” *ACM Trans. Math. Softw.*, vol. 8, no. 1, pp. 43–71, 1982.
- [172] C. B. Shaw, J. Prakash, M. Pramanik, and P. K. Yalavarthy, “Least squares QR-based decomposition provides an efficient way of computing optimal regularization parameter in photoacoustic tomography,” *J. Biomed. Opt.*, vol. 18, no. 8, p. 080501, 2013.

List of Publications

Kaushik Basak Chowdhury, Jaya Prakash, Angelos Karlas, Dominik Jüstel and Vasilis Ntziachristos

A Synthetic Total Impulse Response Characterization Method for Correction of Hand-held Optoacoustic Images

IEEE Transactions on Medical Imaging

Volume: 39, Issue: 10 , Oct. 2020

DOI: 10.1109/TMI.2020.2989236

Kaushik Basak Chowdhury, Christoph Denher, Maximilian Bader, Dominik Jüstel and Vasilis Ntziachristos

An Individual Transducer Impulse Response Characterization Method to Improve Image Quality of Array-based Handheld Optoacoustic Tomography

Optics Letters

Volume: 46, Issue: 1, Jan. 2021

DOI: 10.1364/OL.412661

Christoph Denher, Ivan Olefir, **Kaushik Basak Chowdhury**, Dominik Jüstel and Vasilis Ntziachristos

Deep learning based electrical noise removal enables high spectral optoacoustic contrast in deep tissue

arXiv:2102.12960